The Pennsylvania State University
The Graduate School
College of Engineering

STUDY OF STRUCTURE AND DYNAMICS OF PLANT CELL WALL POLYSACCHARIDES VIA NEUTRON SCATTERINGS

A Dissertation in
Chemical Engineering
by
Shih-Chun Huang

© 2015 Shih-Chun Huang

Submitted in Partial Fulfillment
of the Requirements
for the Degree of

Doctor of Philosophy

May 2015

The dissertation of Shih-Chun Huang was reviewed and approved* by the following:

Janna K. Maranas
Graduate Program Director
Professor of Chemical Engineering and Material Science and Engineering
Dissertation Advisor, Chair of Committee

Seong H. Kim
Professor of Chemical Engineering and Material Science and Engineering

Enrique D. Gomez
Assistant Professor of Chemical Engineering

Daniel J. Cosgrove
Professor of Biology

*Signatures are on file in the Graduate School

Abstract

Plant cell wall plays important biological functions of plant bodies and constitutes many renewable sources that can be used to make paper, textile, polymer derivatives and alternative energy resources. At the nanoscale, plant cell wall is an extraordinarily complex composite composed of three polysaccharides, namely, cellulose, hemicellulose and pectins. Despite numerous works have been done to understand the wall polysaccharides over the past three centuries, many aspects of cell wall are still not clear.

To enhance the understanding of plant cell wall, it is necessary to investigate cell wall at molecular level. Cell walls of both wild-type and xyloglucan-deficient mutant *Arabidopsis thaliana* are investigated. HPAEC experiment is performed to determine the fraction of cellulose, hemicellulose, and pectins. Cell wall structure at nanometer scale is characterized by small-angle neutron scattering (SANS). In this work, two methodologies are used to obtain information that was not available before. One is applying selective deuterium labeling on the non-cellulose polysaccharides in cell wall. Since the scattering of neutron from hydrogen is very different than that of deuterium, doing selective deuterium labeling create contrast between cellulose and the non-cellulose polysaccharides. Another method applied here is using contrast

matching to detect structure of cellulose and the non-cellulose polysaccharides in turn. Models are utilized to fit the SANS profiles and to obtain the structural information of the cell wall samples. As expected, cellulose is high-aspect cylinders with diameters of about 3 nm and lengths of more than 100 nm. Partial surface of cellulose is covered by non-cellulose polysaccharides in *wild-type Arabidopsis*, which feature is negligible in xyloglucan-deficient mutant. This difference illustrates a unique role of xyloglucan in cell wall. However, not all xyloglucan is in close contact with cellulose, about half of xyloglucan has structure similar to the other non-cellulose polysaccharides, being solvated in water and only form extended coils, potentially function as spacers to separate cellulose microfibrils.

The experiment method, used to determined cell wall structure of *Arabidopsis*, is extended to several plant species to obtain a more general picture of cell wall. One prominent difference among plants is cell wall composition. For example, non-graminaceous land plants contain a large fraction of xyloglucan whereas graminaceous monocot cell walls contain little xyloglucan but much mixed-linkage glucans and arabinoxylans. HPAEC and SANS are used to determine the composition and the cell wall structure of cucumber, onion, wheat and maize. The composition and the cell wall structure of cucumber and onion are similar to that is found in wild-type *Arabidopsis*: cellulose microfibrils are about 3 nm thick and partially coated by xyloglucan. Most of the non-cellulose polysaccharides form extended coils. Maize and wheat have little xyloglucan and decent amount of mixed-linkage glucan. A decent coating around cellulose microfibril is observed in in maize cell wall,

presumably the mixed-linkage glucan play a similar role as xyloglucan in maize. This might be because the similar backbone to xyloglucan and cellulose microfibrils.

To fully understand plant cell wall, we study not only cellulose-xyloglucan interaction between cellulose and the other polysaccharides, but also the interaction between cellulose and water. It should be noted that water makes up about 80% mass of cell wall. To remain active, cell wall requires an aqueous environment to permeate proteins and ions. Quasi-elastic neutron scattering is used to study the water dynamics. We investigate the state of water when it is in close contact with cellulose. On the surface of cellulose, two hydration layers are identified. Water in the inner hydration layer is directly constrained by the surface of cellulose. Thus the water molecules are confined and show relaxation times 100 times slower than bulk water. Water in the outer hydration layer is less confined but still has dynamics 5 times slower than bulk water. Despite the difference in the translational motion, both inner and outer hydration water shares similar rotational and vibrational diffusivity.

To sum up, we bring an integrated result that includes the molecular interaction not only between cellulose and the non-cellulose polysaccharides but also between cellulose and water. Our results indicate cellulose in primary cell wall is about 3 nm thick, and sometimes the surface is covered by matrix polysaccharides if xyloglucan or mixed-linked glucan is decent. Most matrix polysaccharides are not capable to directly deposit on the cellulose surface. Instead, they form extended coils, presumably function as interfibril spacers. It should be noted that in the current picture of cell wall, water is often regarded as background. However, their very slow

dynamics when it is in close contact with cellulose illustrates their ability to form direct bonding with cellulose. This should be taken into consideration in many experiment interpretations and building the cell wall model.

TABLE OF CONTENTS

List of Figures ix
List of Tables xii
Acknowledgements xiii
Chapter 1 Introduction 1
1.1 General Background of Cell Wall 1
1.2 The Structural Polysaccharides of the Cell Wall and Their Functions 2
1.2.1 Cellulose 3
1.2.2 Hemicellulose Functions and Cell Wall Models 5
1.2.3 Structure and Function of Pectin in Cell Walls 7
1.3 Objectives of the present work 10
1.3.1 Cell wall organization in the model dicot *Arabidopsis thaliana* 10
1.3.2 Cell Wall Architecture in Monocot and Dicot Primary Cell Wall 11
1.3.3 Water Dynamics in Close Contact with Cellulose Microfibril 11
1.4 Thesis Organization 12
1.5 References 12
Chapter 2 Experimental Techniques 19
2.1 Neutron Scattering Fundamentals 19
2.2 Small Angle Neutron Scattering (SANS) 22
2.2 Dynamics: Quasi-Elastic Neutron Scattering [QENS] 24
2.2.1 Disk Chopper Time-of-Flight Spectrometer [DCS] 25
2.2.2 Backscattering Spectrometer (BASIS) 27
2.3 Morphology: Field-Emission Scanning Electron Microscopy [FESEM] 28
Chapter 3 Conformation of Polysaccharides in Arabidopsis Primary Plant Cell Walls 30
3.1 Introduction 31
3.2 Materials and Methods 34
3.3 Results and Discussion 39
3.4 Conclusion 48
3.5 Reference 49
Chapter 4 Structure of Monocot and Dicot Primary Cell Wall Polysaccharides from Small-Angle Neutron Scattering 55

4.1 Introduction 56
4.3 Results and Discussion 62
4.4 Conclusion 73
4.5 Reference 74
Chapter 5 The Confined Dynamics of Surface Water of Cellulose Microfibril 80
5.1 Introduction 81
5.2 Materials and Methods 84
5.3 Result and Discussion 87
5.4 Conclusion 101
5.5 Reference 101
Chapter 6 Concluding Remarks and Suggestions for Future Directions 107
6.1 Xyloglucan and pectins in *Arabidopsis* primary cell walls 107
6.2 Impact of different hemicellulose on primary cell wall structure 108
6.3 Confined dynamics of water when confined by cellulose microfibril 109
6.4 Suggestion for future direction of this work and preliminary results 110
6.4.1 Gel formation of pectin in cell wall 110
6.4.2 Assembly of secondary cell wall 112
6.4.3 Cellulose in secondary cell wall produced by inactivation of cellulose synthease proteins 113
6.4.4 Bacterial cellulose as a model system to study the interaction of matrix polysaccharides 114
Appendix A: SANS Fitting Procedures 117
Appendix B: Alternative Fit Models 121

List of Figures

Figure 1.1: Single cellulose chain repeat unit 4

Figure 1.2: Schematic of the unit cells and the crystal cell dimension for cellulose I_α and I_β (courtesy to Pérez and Samain, 2010) [50]. 4

Figure 1.3: Monosaccharides and classic repeat units of hemicellulose 6

Figure 1.4: Chemical structure of HG, RG-I and RG-II 8

Figure 1.5: Schematic representation of calcium binding of pectin gel formation [57] 9

Figure 2.1: Dependence of penetration depth on atomic number for electrons, x-rays and neutrons. Penetration depth is defined where the beam intensity is reduced by a factor of 1/e (37%) to its original intensity. [1] 21

Figure 2.2: Neutron scattering variables and the corresponding neutron scattering techniques 22

Figure 2.3: Schematic of a SANS measurement. The incident beam scatters from the sample at an able of 2θ. The scattered beam is detected on an area detector 22

Figure 2.4: Contrast variation as a function of D_2O concentration.....24

Figure 2.5: Examples of elastic, inelastic and quasi-elastic scattering. The x-axis represents the gain or loss in energy experienced by the neutron and the y-axis represents the number of scattered neutrons. 25

Figure 2.6: (A) The DCS instrument at the NCNR (B) Schematic of DCS time-of-flight measurement: a pulse of neutrons arrives at the sample and some neutrons are scattered at angle *2θ* (pulser and monochromator is not included for simplicity.) 25

Figure 2.7: The kinetic allowed region for DCS at λ = 4.8Å, medium resolution 27

Figure 2.8: BASIS instrument at SNS, ORNL 28

Figure 2.9: Schematic of FESEM setup. The electron beam reflects from the sample with backscattered electrons, secondary electrons that will be collected for imaging and meanwhile this process produce photons, x-rays and some of the wave is adsorbed or transmitted to sample. 29

Figure 3.1: SANS cellulose-highlighted profiles for wild type and *xxt1/xxt2 Arabidopsis* cell wall before and after depectination in absolute scale. Measurements were performed in 48% D_2O to highlight the structure of cellulose microfibril. Fitting lines (black lines) are overlaid for each data set and parameters are shown in Table 3.2.....58

Figure 3.2: SANS cellulose-matched profiles (points) for wild type and *xxt1/xxt2 Arabidopsis* cell wall before and after depectination. Measurements were performed in 35% D_2O to highlight the structure of non-cellulose wall polysaccharides. Fitting lines (black lines) are overlaid for each data set and data are shifted for clarity

Figure 3.3: WT (left) and xxt1/xxt2 (right) Arabidopsis primary wall schematics based on SANS results 63

Figure 4.1: Cellulose-highlight measurements for cucumber, onion, maize and wheat. Intensity profiles are shifted for clarity and the scale factors are shown in the figure. Measurements were performed in 48% D_2O to highlight the cellulose structure. Fitting lines are overlaid for each data and parameters are summarized in Table III. 66

Figure 4.2: (upper) Probability distribution of cellulose diameter for primary cell walls of cucumber, onion, maize, wheat and Arabidopsis, obtained from the fitting parameter of average diameter and Schultz distribution (lower) Cellulose diameter reported in literatures 68

Figure 4.3: Matrix-polysaccharide-highlight measurements for cucumber, onion, maize and wheat. Intensity profiles are shifted for clarity and the scale factors are shown in the figure. Measurements were performed in 35% (v/v) D_2O solution to highlight the structure of matrix polysaccharides. Fitting lines are overlaid for each data and parameters are summarized in Table 4.4 and Table 4.5. 69

Figure 4.4: Correlation of cellulose coated fraction with xyloglucan-to-cellulose ratio ...72

Figure 5.1: SFG comparison of d-cellulose and h-cellulose 89

Figure 5.2: XRD of h-cellulose and d-cellulose 90

Figure 5.3: Comparison of FESEM direct images of h-cellulose and d-cellulose.....91

Figure 5.4: (A) $S(Q,\omega)$ of 25% hydrated d-cellulose sample at 298K measured at DCS at Q=1.2 $Å^{-1}$ (B) $S(Q,\omega)$ of 20% hydrated d-cellulose sample at 298K measured at BSS at Q=1.2 $Å^{-1}$ (C) Fourier-transformed self-intermediate scattering function $S(Q,t)$ of DCS and BSS spectra and the corresponding fit lines for 25% hydrated d-cellulose sample at 298K at Q=1.2 $Å^{-1}$. 92

Figure 5.5: Temperature dependence of the rotational relaxation time of 11W(solid circle), 25W(circle) and bulk water (dashed line) 95

Figure 5.6: The Q dependence of the translational relaxation time in 11W and 25W samples. It is readily seen that the Q^2 dependence of translational relaxation time obeys jump diffusion model at 278–338K. T=278K(blue); T=298K(green); T=318K(orange); T=338K(red). 97

Figure 5.7: The temperature dependence of the characteristic times for the two translational motions of surface water on cellulose surface compared with bulk water. The translational residence times obey an Arrhenius-type temperature dependence. Slow translation in 11W (solid circle); Slow translation in 25W (empty circle); Fast translation in 11W (solid triangle); Fast translation in 25W (empty triangle); Bulk water after Teixeira et al (solid square). 99

Figure 5.8: Schematic of water molecule dynamics in close contact with cellulose microfibril 100

Figure 6.1: SANS measurement on 1wt% xyloglucan D_2O solution at pH 2–7. Structure does not change responsive to pH of environment. 112

Figure 6.2 SEM images of bacterial cellulose model system. (A) control (B) cultured with xyloglucan (C) cultured with xylan (D) cultured with homogalacturan. (In courtesy of Jin Gu and Jeffery M. Catchmark, *Carbonhydrate Polymer* 2012).....115

Figure 6.3 SANS spectrum of bacterial cellulose composite with xyloglucan, xylan, pectin measured under the contrast match point of deuterated cellulose (81% D_2O) 116

List of Tables

Table 1.1 Occurrence of hemicellulose in primary and secondary walls of plants 6

Table 3.1: Component analysis of WT and *xxt1/xxt2* at untreated and depectinated states. Units: mole % based on total sugars (± SEM, n=3).....55

Table 3.2: Characteristics of cellulose microfibrils in the WT and *xxt1/xxt2 Arabidopsis* walls under untreated and depectinated conditions

Table 3.3: Characteristics of the core-shell features in WT and *xxt1/xxt2 Arabidopsis* cell walls under depectinated condition.....57

Table 3.4: Characteristics of the correlational length features of non-cellulose polysaccharides in WT and *xxt1/xxt2 Arabidopsis* walls under untreated and depectinated condition 61

Table 4.1: Monosaccharide Composition Analysis of primary cell walls from maize, cucumber, wheat and onion 64

Table 4.2: Polysaccharide fraction in the primary cell walls of maize, cucumber, wheat and onion. Units: mole % based on total sugars.....65

Table 4.3: Characteristics of cellulose microfibril in the primary cell walls of cucumber, onion, maize and wheat.....67

Table 4.4. Coating features around cellulose microfibrils in primary cell walls of cucumber, onion, maize and wheat.....70

Table 4.5: Correlation length parameters of matrix polysaccharides in primary cell walls of cucumber, onion, maize and wheat.....73

Table 5.1: Comparison of h-cellulose and d- cellulose crystal structure.....90

Table 5.2: The temperature and water content dependence of translational relaxation time, jump length and diffusion coefficient. The jump length is calculated by $L=(6D\tau_{res})^{1/2}$ 99

Acknowledgements

2010–2015 has been the most challenging and exciting years of my life to date, and I have numerous people I would like to thank for the help and warm I receive through this time.

First and foremost, I would like to thank my advisor, Dr. Janna K. Maranas, for giving me the admission coming to Penn State and the opportunity to join your research group. When I first started the project, I was much like many students just finished their undergraduate learning. There had been so much works ahead for me to excel in research. Thank you for introducing me into the world of plant cell wall, neutron scattering, and a lot of things written in this thesis. Thank you for being so patient and always allow me enough time to learn. Your intellectual guidance on the project has helped me the most. I also want to thank your for encouraging me to attend conferences and meetings, from which I had extensive practice on writing and presentation skills. Thank you so much for making my graduate experience so valuable and memorable.

I extend my deepest gratitude to those professional scientists from a variety of scientific field. I would like to thank Dr. Seong Kim, Dr. Enrique Gomez and Dr. Daniel Cosgrove. Thank you for all the knowledgeable insight toward my project and the time of being my committee members. I appreciate you taking time to read my thesis and to give me great advices. I would like to thank Dr. Yong Bum Park for the valuable research input and for preparing cell wall samples. I would like to thank Dr. Lin Fang for doing bacterial cellulose synthesis and several kinds of cellulose

modifications. I would like to thank scientist from NIST including Yun Liu, Steve Kline, Paul Butler, Boualem Hammouda, Daniel Pajerowski, John Copley and scientist from ORNL including Shuo Qian, Changwoo Do, Sai Venkatesh Pingali, Souleymane Omer Diallo, and Eugene Mamontov for insightful discussions on the scattering data and its scientific meanings behind. Thank you for being so patient with my questions and experiment requests.

I would like to thank to all former and current members in Janna Maranas research group. It is my pleasure to work with you. I will miss the time a lot that we had brainstorming in group meetings and face-to-face discussions. I sincerely appreciate to Lalitha Ganapatibohtla, Pengfei Zhan, Dan Ye, Sarah Kiemle, David Caldwell, Xinren Yu, who helped me with my neutron scattering experiments. Without your help, I will never finish those intense marathon-type neutron scattering experiments. It is hard to picture how much effort it takes without being actually there.

A special thank to the last group of people who is by far the most important ones to me. I would like to thank my families for the encouragement and dedication throughout this process. I am grateful to have the chance to be your son, brother, and husband. Studying abroad and doing research have a variety of different challenges. There are peaks and valleys associated with it, and my family is always there whenever I need. I cannot say enough to thank you for all the things you have done to support me through these meaningful and great years.

Thank you all so much! I can honest say this work could not have been completed without support from all of you.

The work is supported as part of The Center for Lignocellulose Structure and Formation, an Energy Frontier Research Center funded by the U.S. Department of Energy, Office of Science, Office of Basic Energy Sciences under Award Number DE-SC0001090.

Chapter 1 Introduction

1.1 General Background of Cell Wall

About three centuries ago, Robert Hooke first observed the plant cell wall through a primitive microscope. Gradually we have come to recognize that the plant cell wall is a dynamic, precisely regulated living structure. In plants, cell walls are necessary for the mechanical strength, tissue cohesion, ion exchange, protection, growth and division of plant cells. Without cell walls, plants would not have an opportunity to grow or maintain their biological functions. The size, shape, and position of plant cells are regulated by cell walls [1,2]. Some plants reach heights of more than 100 m, and cell walls hold up the plants, which would otherwise collapse under the force of gravity [1–3]. Despite being strong and rigid, cell walls are dynamic systems. They allow the exchange of material between cells, and can deform to accommodate the expansion of cells (which can be up to 30,000-fold in the largest plant cells). Polysaccharides from plant cell walls are used in the paper and textile industry. They are also gaining attentions as sources of environmentally friendly biomass [3–6] and functional additive in advanced materials. Thus, a comprehensive study of the structure, intermolecular interaction, and dynamics of polysaccharides in cell walls has fundamental and practical significance.

Plants produce two types of cell walls: primary and secondary. Primary cell walls are very thin, flexible layers formed during plant expansion [1]. The thinness (100–300 nm) and the fibrous structure (at a few nm) of primary cell walls can be observed using light and electron microscope [7–10]. Although primary cell walls are very thin, they are capable of withstanding the tensile forces arising from turgor pressure [11,12]. Primary cell walls serve important functions in plant growth, whereas secondary walls are usually

formed when cells have completed their growth. An important reason for plants to build secondary cell wall is to provide mechanical reinforcement and rigidity [13]. The presence of secondary walls allows tall plants to support their weight and to form xylem to transport water. Both primary and secondary walls are microfibril-based nanocomposites, but they differ in many aspects. Many secondary cell walls contain lignin and are more diverse in their structure. As lignin is highly hydrophobic, the deposition of lignin in secondary cell wall serves to drive the water out of the tissue [1], which makes secondary walls have very little water content while primary cell walls are about 80% water by mass.

1.2 The Structural Polysaccharides of the Cell Wall and Their Functions

In this thesis, we focus on characterizing primary cell walls, which contain mostly polysaccharides and a minor fraction of structural proteins. The composition of polysaccharides varies between plant species and tissues. Classically, primary cell walls Contain 15–40% cellulose, 20–30% hemicellulose (mostly xyloglucan), and 30–50% pectic polysaccharides [1,2,14]. Notable exceptions to the general composition pattern include the primary walls of grasses and celery. In grasses, the dominant hemicelluloses are arabinoxylan and mixed linkage glucan rather than xyloglucan [11,15,16]. Celery's primary cell wall on the other hand, has very little hemicellulose [13,17,18]. Many biochemical, chemical and physical methods have been employed to study the structure and the molecular interactions of the wall polysaccharides [14,19,22,23]. It is clear that the intermolecular interactions and the molecular level structure determine the mechanical performance and the expansion mechanism of cell wall [7,19–21]. Chemicals

and enzymes were used to sequentially solubilize polysaccharides from the cell walls to determine the mass fraction of each polysaccharide. Because cellulose is the final component after the series of treatments, the difficulty of removing the non-cellulosic polysaccharides thus indicates their affinity to cellulose microfibril [23]. The extracted polysaccharides have been characterized using mass spectrometry and dynamic light scattering to determine the size and the conformation of their chain length and conformation in solutions. However, the structure of components might change during extraction and therefore not reflect their genuine structure as in cell walls. TO obtain in situ information about cell wall structure, many researchers use physical methods such as nuclear magnetic resonance [16,17,24–33], optical spectroscopies [34–40], x-ray [17,41–44] and neutron scattering [4,45,46]. Here we would like to summarize the current knowledge about each polysaccharide class and its role in cell wall structure.

1.2.1 Cellulose

As the most abundant biological material on earth, cellulose is the most well-understood cell wall component. Cellulose was first isolated 130 years ago by French scientist Anselme Payen after he treated wood with nitric acid. The name “cellulose” originally came from the acid resistant substance of wood. The modern definition of cellulose refers to the polysaccharide of linear (1,4) β-D-glucan as shown in Figure 1.1.

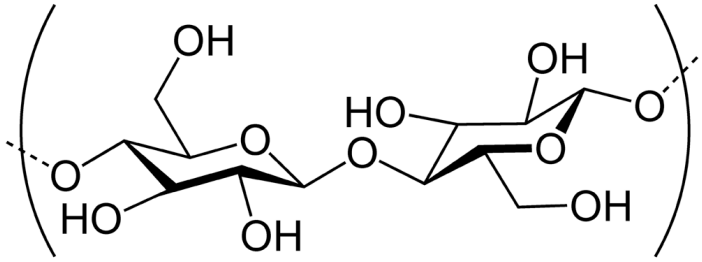

Figure 1.1: Single cellulose chain repeat unit

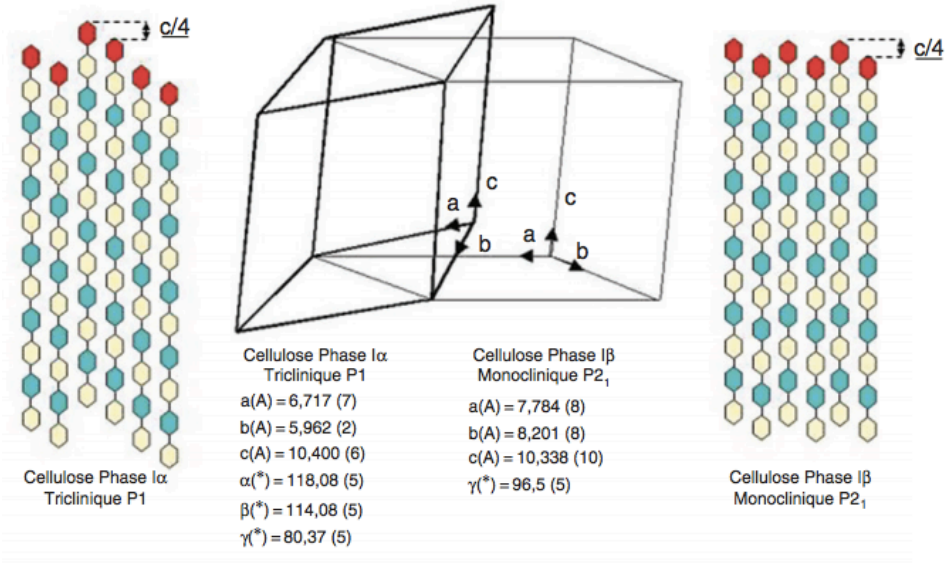

Figure 1.2: Schematic of the unit cells and the crystal cell dimensions for cellulose I_α and I_β (from Pérez and Samain, 2010) [50].

In nature, many cellulose chains assemble in parallel to form a highly crystalline microfibril [41,47,48]. The microfibril is mechanically strong and highly resistant to chemical and enzyme treatments. These properties make cellulose an ideal cell wall scaffold. In nature, cellulose has two crystal structures known as I_α and I_β [41,47,49], as shown in Figure 1.2.

Cellulose I_α is considered a metastable state because I_α can be converted to I_β upon heating or upon interaction with some cell wall polysaccharides [43,51,52]. The cellulose I_α and I_β can also be chemically converted to other crystal forms such as cellulose II, III and IV, which are not found in nature and thus beyond the interest of this thesis. Natural cellulose microfibrils always contain a mixture of I_α and I_β cellulose [39]. The I_α/I_β fraction varies with the origin of cellulose. Cellulose produced by algae, bacteria or tunicate is primarily in the form of I_α whereas cellulose in higher plants is primarily in the form of I_β [53]. Microfibril dimensions also depend on the cellulose source: most plant microfibrils are about 3 nm thick, while algae and tunicate microfibrils are more than 20 nm thick [53]. There is not a direct evidence to relate cellulose thickness to its crystal structure. The differences can be traced back to the mechanism of cellulose synthesis and the shape of cellulose-producing enzyme [1].

1.2.2 Hemicellulose Functions and Cell Wall Models

Hemicellulose was traditionally defined as the wall polysaccharides extracted by strong alkaline treatment. But in last two decades it became clear that some pectic polysaccharides are also solved by the alkaline solution. Thus the old definition is no longer useful. The modern definition for hemicellulose is the cell wall polysaccharides with equatorial β-(1,4)-linked backbones [54]. Figure 1.3 shows the common types of hemicellulose and Table 1.1 summarizes the typical fraction of each hemicellulose in dicot and grass cell walls, as measured by sequential extraction analysis.

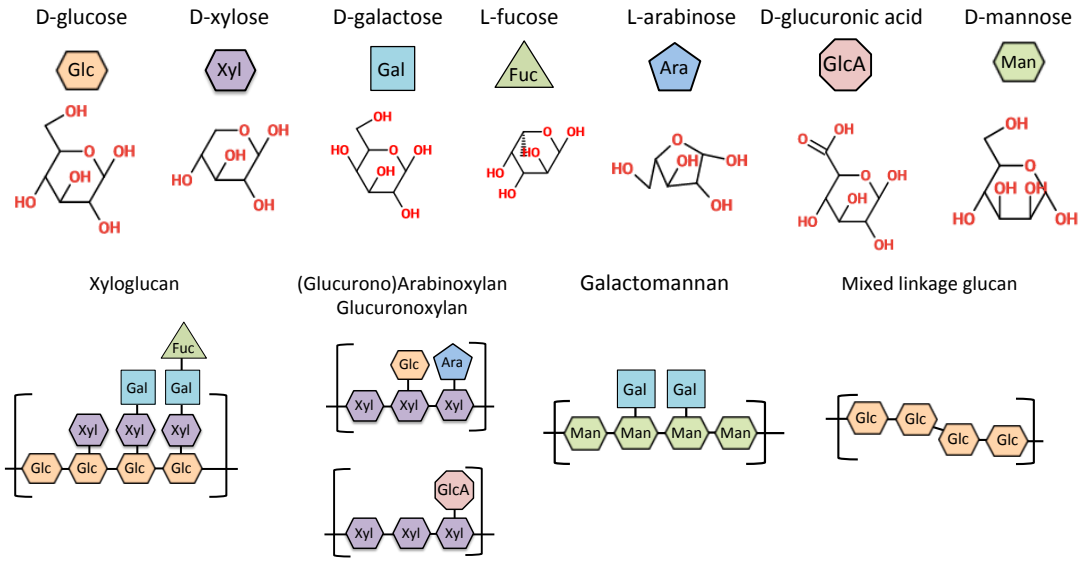

Figure 1.3: Monosaccharides and classic repeat units of hemicellulose

Table 1.1 Occurrence of hemicellulose in primary and secondary walls of plants [54]

Amount of polysaccharide in wall (% w/w)				
Polysaccharides	Dicot walls		Grass walls	
	Primary	Secondary	Primary	Secondary
Xyloglucan	20–25	-	2–5	-
(Glucorono)arabinoxylan	5	-	20–40	40–50
Glucuronoxylan	-	20–30	-	-
Galactomannan	3–5	2–5	2	0–5
Mixed linkage glucan	-	-	2–15	-

-, absent or minor

Hemicellulose plays an important role in integrating the cell wall entity. Although cellulose is responsible for the cell wall's microfibril-based structure, enzyme activity on the hemicellulose allows cell wall expansion [7,19]. This finding has suggested an important role of hemicellulose in expansion and cell wall structure [2,7,26]. The hemicellulose's position has been debated for decades. The very first cell wall model

viewed the wall as a giant molecule, in which all non-cellulose polysaccharides are convalently linked together [55]. This model however is not supported by later chemical extraction experiments, which show a sequential extractability of the wall polysaccharides. Also, this model predicts extensive hemicellulose–pectin linkage, which is not yet confirmed [22,57]. An alternative theory called the "tethering network" model was proposed and has become one of the most influential models. In this model, xyloglucan tethers cellulose microfibrils to form a load-bearing network while pectic polysaccharides form an independent network interlaced with the cellulose-xyloglucan network [10,23,58–60]. This model suggests that xyloglucan forms three different structures [23]: one is flexible chains that tether, loop and free stand between microfibrils; another is a tightly bound coating of chains on microfibril's surface; and the last group of xyloglucan is embedded in cellulose microfibril. The "tethering network" model is supported by numerous experiments [52,61–63], but evidence to the contrary also exists [19,24]. For example, the tethering model predicts that xyloglucan removal should lead to wall creep, which is not consistent with recent experiments on cucumber cell walls [19]. The model also suggests extensive interaction between xyloglucan and the surface cellulose, which is not found in the nuclear magnetic resonance spectrum on *Arabidopsis thaliana* and *mung* bean [25,33]. Other configurations and roles for xyloglucan have been proposed, including spacer between microfibrils to maintain interfibril distance [20,56] or the xyloglucan-cellulose amalgam to strengthen the cell wall [19,63].

1.2.3 Structure and Function of Pectin in Cell Walls

Pectins are a complicated mixture of polysaccharides that make up about half of dry substance in the primary cell walls, where they function as a hydrating agent and a

spacer to separate cellulose microfibrils. Pectins are found in relatively large amounts in soft plant tissues under conditions of rapid growth and higher moisture content. Pectins are heterogeneous with respect to chemical structure and molecular weight. Their composition varies with plant species, growth stage, location, extraction method and other environmental factors. Elucidation of pectin's structure is important for understanding its role in plant growth and development. Figure 1.4 shows the chemical structure of three pectin subclasses, namely, homogalaturon (HG), rhamnogalacturonan I (RG-I) and rhamnogalacturonan II (RG-II).

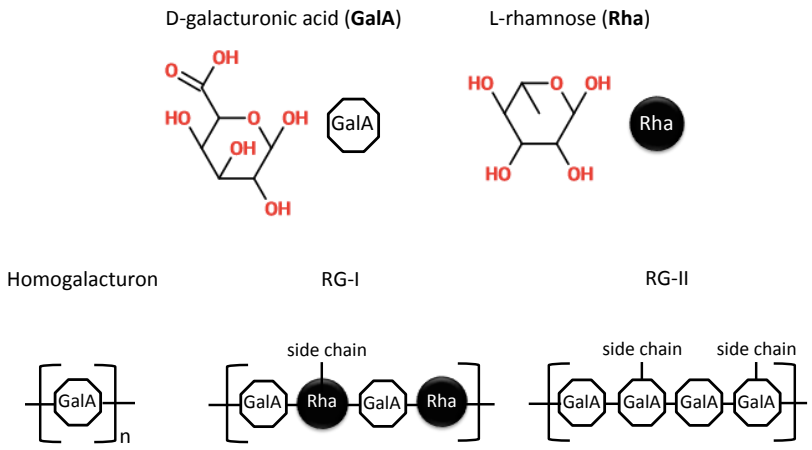

Figure 1.4: Chemical structure of HG, RG-I and RG-II

Pectins could form hydrogels in the presence of chelating agents such as Ca^{2+} ions, boron, sugar and acid. Pectin's gel forming ability makes it both a necessary cell wall component and an important ingredient in many food products. As shown in Figure 1.5, the structure of pectin hydrogel includes three parts:

1. Junctions where pectins are joined by chelating agents (Ca^{2+} ions, boron etc)
2. Interjunction mobile segments

3. Water trapped in the pectin network

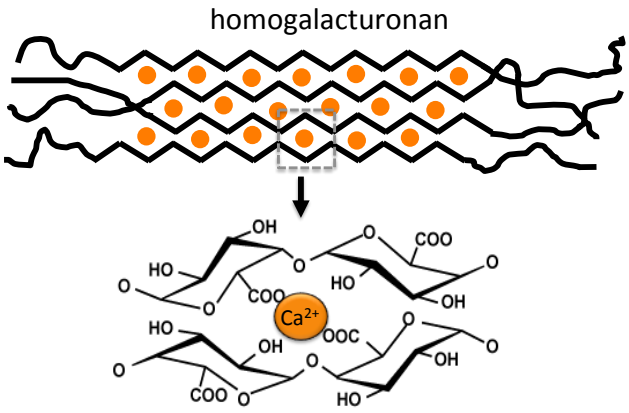

Figure 1.5: Schematic representation of calcium binding and pectin gel structure [57]

In the example in Figure 1.5, pectin crosslinks with Ca^{2+} ions through their carboxyl groups. The carboxyl groups in pectin are often methyl esterified. Plant cells control the pectin gelation by manipulating the degree of esterification. Gelation in rapidly expanding cells is less desirable. To minimize the gelation under these conditions, carboxyl groups are esterified (COO^- to COOMe). When the cells cease growth, the methyl ester group would then be converted back to unmasked carboxyl groups by pectin methylesterases, which will induce the gel formation and stiffen the cell wall.

Despite that pectins can stiffen after gelation, most of pectins are easy to extract from cell walls because they lack covalent linkage to either cellulose or hemicellulose. Although pectins fill almost the entire cell wall, nuclear magnetic resonance spectrum has elucidated that there is little strong interaction between pectins and cellulose (even though many pectins are in close contact with cellulose) [16,25]. A small number of covalent bonds between hemicellulose and pectin has been reported [22,64], but it is still not enough for pectin to be considered as one of the load-bearing component.

1.3 Objectives of the present work

The primary goals of the present work are to understand the structure and dynamics of the plant primary cell wall and fill the knowledge gaps in literature reports. These goals are divided into three objectives described below

1.3.1 Cell wall organization in the model dicot *Arabidopsis thaliana*

It is important to elucidate how cellulose, pectins and hemicelluloses interact with each other and compose an integrated wall. The current understanding for cell wall architecture is largely derived from extraction-based chemical analysis, which does not necessarily provide correct information for the physical interaction between wall components. Some popular structural probes such as electron microscopes and x-ray scatterings are not suitable to detect the wall structures because these measurements do not differentiate the wall polysaccharides. We use SANS to address the molecular structure of cellulose and matrix polysaccharides. One challenge of using SANS to detect cell wall structure is that the contrast in native cell wall is very low. To resolve this limitation, we combine selective deuterium labeling and contrast matching. The measurement under contrast matching conditions highlights the structure of cellulose and matrix polysaccharides in turns. To determine the structure of xyloglucan and pectin in cell wall architecture, we compare wild-type and xyloglucan-deficient *Arabidopsis thaliana*, and compare the cell wall structure prior and after partial pectin removal. Based on the analysis of structure, location, dimension and fraction of each wall component in

each type of the cell walls, we bring an integrated structure of primary cell wall that is consistent with all SANS data.

1.3.2 Cell Wall Architecture in Monocot and Dicot Primary Cell Wall

The polysaccharide structure in the primary cell walls of cucumber, onion, maize and wheat are investigated. Monocot and dicot plant species are selected to make a comprehensive study on purpose. While all these cell walls contain cellulose as the main structural scaffold, monocots contain mixed linkage glucan and arabinoxylan as the main hemicellulose, and dicots contain xyloglucan as the main hemicellulose. The structure of cellulose microfibril and the non-cellulosic polysaccharides are determined in turns using contrast matching. Since xyloglucan is also abundant in the primary cell walls of cucumber and onion, it is of great interest whether the cell wall structure is similar to *Arabidopsis* cell walls. On the other hand, for monocot primary cell walls such as maize and wheat that have little xyloglucan, whether arbinoxylan, mixed linkage glucan or pectins play the function of xyloglucan is also worth investigating.

1.3.3 Water Dynamics in Close Contact with Cellulose Microfibril

Primary cell walls include an aqueous environment to allow biologic function of proteins and to transport ions. As mentioned in earlier section, cellulose, the most important component in cell walls, is in hydrated state. Since water often plays an active role to change the structure and the dynamics of macromolecules, extensive studies have been done to study how cellulose-water interaction affects cellulose structure. However, only scarce reports have been tried to study the state of water when interacting with

cellulose. In this case, water is often assumed to maintain the same properties as bulk water. Radloff et al [32] studied the water in extracted cellulose and identified three distinct water populations in hydrated cellulose matrix: namely highly mobile water, non-freezable rigid water, and very strongly bound water. The authors provided a valuable viewpoint at large time and length scale. However, some details would not be clear without knowing the dynamics process at smaller time and length scale. To fill the knowledge gap, we extend the dynamics investigation to time scale down to ps and length scale down to nm by using quasi-elastic neutron scattering on deuterated cellulose sample.

1.4 Thesis Organization

The remainder of this document is organized into 6 chapters. Chapter 2 contains a detailed description of the working principles of the experimental techniques employed in this work. In Chapter 3, a report of the cell wall organization in *Arabidopsis* and how the structure might influence cell wall properties are discussed. The structure feature is further compared to other plant species and discussed in Chapter 4. Chapter 5 discusses the cellulose-water interaction and the method of producing deuterated microfibril. Finally, we conclude important findings in Chapter 6 and provide suggestions for future direction of this work.

1.5 References

1. Albersheim, P., Darvill, A., Roberts, K., Sederoff, R. & Staehelin, A. Plant cell walls: from chemistry to biology. (Garland Science, Taylor and Francis Group, LLC, 2010).

2. Cosgrove, D. J. Growth of the plant cell wall. Nat. Rev. Mol. Cell Biol. 6, 850–61 (2005).

3. Silveira, R. L., Stoyanov, S. R., Gusarov, S., Skaf, M. S. & Kovalenko, A. Plant biomass recalcitrance: effect of hemicellulose composition on nanoscale forces that control cell wall strength. J. Am. Chem. Soc. 135, 19048–51 (2013).

4. Pingali, S. V. et al. Breakdown of cell wall nanostructure in dilute acid pretreated biomass. Biomacromolecules 11, 2329–35 (2010).

5. Cheng, G. et al. Transition of cellulose crystalline structure and surface morphology of biomass as a function of ionic liquid pretreatment and its relation to enzymatic hydrolysis. Biomacromolecules 12, 933–41 (2011).

6. Pingali, S. V. et al. Morphological changes in the cellulose and lignin components of biomass occur at different stages during steam pretreatment. Cellulose 21, 873–878 (2014).

7. Marga, F., Grandbois, M., Cosgrove, D. J. & Baskin, T. I. Cell wall extension results in the coordinate separation of parallel microfibrils: evidence from scanning electron microscopy and atomic force microscopy. Plant J. 43, 181–90 (2005).

8. McCann, M. C. & Roberts, K. Changes in cell wall architecture during cell elongation. J. Exp. Bot. 45, 1683–1691 (1994).

9. McCann, M. C., Wells, B. & Roberts, K. Complexity in the spatial localization and length distribution of plant cell-wall matrix polysaccharides. J. Microsc. 166, 123–136 (1992).

10. McCann, M. C., Wells, B. & Roberts, K. Direct visualization of cross-links in the primary plant cell wall. J. Cell Sci. 96, 323–334 (1990).

11. Carpita, N. C. & Gibeaut, D. M. Structural models of primary cell walls in flowering plants: consistency of molecular structure with the physical properties of the walls during growth. Plant J. 3, 1–30 (1993).

12. Cosgrove, D. J. Wall extensibility: its nature, measurement and relationship to plant cell growth. New Phytol. 124, 1–23 (1993).

13. Cosgrove, D. J. & Jarvis, M. C. Comparative structure and biomechanics of plant primary and secondary cell walls. Front. Plant Sci. 3, 204 (2012).

14. Zablackis, E., Huang, J., Müllerz, B., Darvill, A. G. & Albersheim, P. Characterization of the cell-wall polysaccharides of Arabidopsis thaliana leaves. Plant Physiol. 107, 1129–1138 (1995).

15. Carpita, N. C. Structure and biogenesis of the cell walls of grasses. Annu. Rev. Plant Physiol. Plant Mol. Biol. 47, 445–476 (1996).

16. Wang, T., Salazar, A., Zabotina, O. A. & Hong, M. Structure and dynamics of brachypodium primary cell wall polysaccharides from two-dimensional (13)c solid-state nuclear magnetic resonance spectroscopy. Biochemistry 53, 2840–54 (2014).

17. Kennedy, C. J. et al. Microfibril diameter in celery collenchyma cellulose: X-ray scattering and NMR evidence. Cellulose 14, 235–246 (2007).

18. Thomas, L. H. et al. Structure of cellulose microfibrils in primary cell walls from collenchyma. Plant Physiol. 161, 465–76 (2013).

19. Park, Y. B. & Cosgrove, D. J. A revised architecture of primary cell walls based on biomechanical changes induced by substrate-specific endoglucanases. Plant Physiol. 158, 1933–43 (2012).

20. Thompson, D. S. How do cell walls regulate plant growth? J. Exp. Bot. 56, 2275–85 (2005).

21. Park, Y. B. & Cosgrove, D. J. Changes in cell wall biomechanical properties in the xyloglucan-deficient xxt1/xxt2 mutant of Arabidopsis. Plant Physiol. 158, 465–75 (2012).

22. Thompson, J. E. & Fry, S. C. Evidence for covalent linkage between xyloglucan and acidic pectins in suspension-cultured rose cells. Planta 211, 275–86 (2000).

23. Pauly, M., Albersheim, P., Darvill, A. & York, W. S. Molecular domains of the cellulose/xyloglucan network in the cell walls of higher plants. Plant J. 20, 629–639 (1999).

24. Dick-Perez, M., Wang, T., Salazar, A., Zabotina, O. A. & Hong, M. Multidimensional solid-state NMR studies of the structure and dynamics of pectic polysaccharides in uniformly 13C-labeled Arabidopsis primary cell walls. Magn. Reson. Chem. 50, 539–50 (2012).

25. Dick-Pérez, M. et al. Structure and interactions of plant cell-wall polysaccharides by two- and three-dimensional magic-angle-spinning solid-state NMR. Biochemistry 50, 989–1000 (2011).

26. Wang, T. et al. Sensitivity-enhanced solid-state NMR detection of expansin's target in plant cell walls. Proc. Natl. Acad. Sci. U. S. A. 110, 16444–16449 (2013).

27. Einfeldt, J., Meißner, D. & Kwasniewski, A. Molecular interpretation of the main relaxations found in dielectric spectra of cellulose – experimental arguments. Cellulose 11, 137–150 (2004).

28. White, P. B., Wang, T., Park, Y. B., Cosgrove, D. J. & Hong, M. Water-polysaccharide interactions in the primary cell wall of Arabidopsis thaliana from polarization transfer solid-state NMR. J. Am. Chem. Soc. (2014).

29. Mansfield, S. D., Kim, H., Lu, F. & Ralph, J. Whole plant cell wall characterization using solution-state 2D NMR. Nat. Protoc. 7, 1579–89 (2012).

30. Foston, M. B., McGaughey, J., O'Neill, H., Evans, B. R. & Ragauskas, A. Deuterium incorporation in biomass cell wall components by NMR analysis. Analyst 137, 1090–3 (2012).

31. Froix, M. F. & Goedde, A. O. The effect of temperature on the cellulose/water Interaction from NMR Relaxation Times. Macromolecules 428–430 (1975).

32. Radloff, D., Boeffel, C. & Spiess, H. W. Cellulose and cellulose/poly(vinyl alcohol) blends. 2. water organization revealed by solid-state NMR spectroscopy. Macromolecules 29, 1528–1534 (1996).

33. Bootten, T. J., Harris, P. J., Melton, L. D. & Newman, R. H. Solid-state 13C-NMR spectroscopy shows that the xyloglucans in the primary cell walls of mung bean (Vigna radiata L.) occur in different domains: a new model for xyloglucan-cellulose interactions in the cell wall. J. Exp. Bot. 55, 571–83 (2004).

34. Lee, C. M. et al. Cellulose polymorphism study with sum-frequency-generation (SFG) vibration spectroscopy: identification of exocyclic CH2OH conformation and chain orientation. Cellulose 20, 991–1000 (2013).

35. Kafle, K. et al. Cellulose microfibril orientation in onion (Allium cepa L.) epidermis studied by atomic force microscopy (AFM) and vibrational sum frequency generation (SFG) spectroscopy. Cellulose 21, 1075–1086 (2013).

36. Barnette, A. L. et al. Selective detection of crystalline cellulose in plant cell walls with sum-frequency-generation (SFG) vibration spectroscopy. Biomacromolecules 12, 2434–9 (2011).

37. Lee, C. M., Mohamed, N. M. A., Watts, H. D., Kubicki, J. D. & Kim, S. H. Sum-frequency-generation vibration spectroscopy and density functional theory calculations with dispersion corrections (DFT-D2) for cellulose Iα and Iβ. J. Phys. Chem. B 117, 6681–92 (2013).

38. Park, Y. B. et al. Monitoring meso-scale ordering of cellulose in intact plant cell walls using sum frequency generation spectroscopy. Plant Physiol. 163, 907–13 (2013).

39. Horikawa, Y. & Sugiyama, J. Accessibility and size of Valonia cellulose microfibril studied by combined deuteration/rehydrogenation and FTIR technique. Cellulose 15, 419–424 (2007).

40. Hishikawa, Y., Togawa, E., Kataoka, Y. & Kondo, T. Characterization of amorphous domains in cellulosic materials using a FTIR deuteration monitoring analysis. Polymer. 40, 7117–7124 (1999).

41. Nishiyama, Y., Langan, P. & Chanzy, H. Crystal structure and hydrogen-bonding system in cellulose I(beta) from synchrotron X-ray and neutron fiber diffraction. J. Am. Chem. Soc. 124, 9074–82 (2002).

42. Bale, H. D. & Schmidt, P. W. Small-angle x-ray scattering investigation of submicroscopic porosity with fractal properties. Phys. Rev. Lett. 53, 596–599 (1984).

43. Park, Y. B. et al. Effects of plant cell wall matrix polysaccharides on bacterial cellulose structure studied with vibrational sum frequency generation spectroscopy and x ray Diffraction. Biomacromolecules 15, 2718–2724 (2014).

44. Park, S., Baker, J. O., Himmel, M. E., Parilla, P. a & Johnson, D. K. Cellulose crystallinity index: measurement techniques and their impact on interpreting cellulase performance. Biotechnol. Biofuels 3, 10 (2010).

45. Pingali, S. V. et al. SANS study of cellulose extracted from switchgrass. Acta Crystallogr. D. Biol. Crystallogr. 66, 1189–93 (2010).

46. Penttilä, P. A. et al. Small-angle scattering study of structural changes in the microfibril network of nanocellulose during enzymatic hydrolysis. Cellulose 20, 1031–1040 (2013).

47. Nishiyama, Y., Sugiyama, J., Chanzy, H. & Langan, P. Crystal structure and hydrogen bonding system in cellulose I(alpha) from synchrotron X-ray and neutron fiber diffraction. J. Am. Chem. Soc. 125, 14300–6 (2003).

48. Matthews, J. F. et al. Computer simulation studies of microcrystalline cellulose Ibeta. Carbohydr. Res. 341, 138–52 (2006).

49. Jarvis, M. Cellulose stacks up. Nature 426, 611–612 (2003).

50. Pérez, S. & Samain, D. Structure and engineering of celluloses. Adv. Carbohydr. Chem. Biochem. 64, 25–116 (2010).

51. Gu, J. & Catchmark, J. M. Impact of hemicelluloses and pectin on sphere-like bacterial cellulose assembly. Carbohydr. Polym. 88, 547–557 (2012).

52. Gu, J. & Catchmark, J. M. The impact of cellulose structure on binding interactions with hemicellulose and pectin. Cellulose 20, 1613–1627 (2013).

53. Nishiyama, Y. Structure and properties of the cellulose microfibril. J. Wood Sci. 55, 241–249 (2009).

54. Scheller, H. V. & Ulvskov, P. Hemicelluloses. Annu. Rev. Plant Biol. 61, 263–89 (2010).

55. Keegstra, K., Talmadge, K. W., Bauer, W. D. & Albersheim, P. The structure of plant cell walls. Plant Physiol. 51, 188–196 (1973).

56. Talbott, L. D. & Ray, P. M. Molecular size and separability features of pea cell wall polysaccharides : implications for models of primary wall structure. Plant Physiol. 98, 357–68 (1992).

57. Thakur, B. R., Singh, R. K. & Handa, a K. Chemistry and uses of pectin--a review. Crit. Rev. Food Sci. Nutr. 37, 47–73 (1997).

58. Hayashi, T. Xyloglucan in the primary cell wall. Annu. Rev. Plant Physio. Plant Mol. Biol. 40, 139–168 (1989).

59. Hayashi, T., Wong, Y.-S. & Maclachlan, G. Pea Xyloglucan and Cellulose. Plant Physiol. 75, 605–610 (1984).

60. Fry, S. C. The Structure and Functions of Xyloglucan. J. Exp. Bot. 40, 1–11 (1989).

61. Hanus, J. & Mazeau, K. The Xyloglucan to Cellulose Assembly at the Atomic Scale. Biopolymers 82, 59–73 (2006).

62. Zhang, Q., Brumer, H., Ågren, H. & Tu, Y. The adsorption of xyloglucan on cellulose: effects of explicit water and side chain variation. Carbohydr. Res. 346, 2595–602 (2011).

63. Zhao, Z., Crespi, V. H., Kubicki, J. D., Cosgrove, D. J. & Zhong, L. Molecular dynamics simulation study of xyloglucan adsorption on cellulose surfaces: effects of surface hydrophobicity and side-chain variation. Cellulose 21, 1025–1039 (2014).

64. Popper, Z. A. & Fry, S. C. Xyloglucan-pectin linkages are formed intra-protoplasmically, contribute to wall-assembly, and remain stable in the cell wall. Planta 227, 781–94 (2008).

Chapter 2 Experimental Techniques

The purpose of this chapter is to review the experimental techniques used in this study and to outline the expected results for our specific system. These techniques include small-angle neutron scattering, quasi-elastic neutron scattering, and Field-Emission Scanning Electron Microscopy.

2.1 Neutron Scattering Fundamentals

Neutron scattering is a useful and versatile technique for studying the molecular structure and dynamics of water, polymers, proteins, living cells and even for condensed matters. Molecular structure can be detected because the neutron wavelengths are comparable to atomic sizes and inter-distance spacing. Dynamics can be detected because the neutron energies are comparable to normal motion mode energies in materials. Generally, neutrons have the greatest penetration depth when compared to other waves used to study materials. Electron waves are deflected by the electron cloud around an atom, and therefore penetrate least. X-ray waves penetrate more than electron waves, but are still influenced by electromagnetic field. Neutrons only interact with atoms through short-range nuclear interactions, and therefore penetrate the most. Unlike electrons and x-rays, the interaction strength between neutrons and an atom varies randomly with atomic number, as shown in Figure 2.1. In fact, some atoms that scatter x-rays and electrons weakly, such as hydrogen, can scatter neutrons strongly. This allows the use of neutron to study plant cell walls that primarily contain light atoms such as hydrogen, oxygen and carbon. The strength of neutron interaction with an atom is quantified by the atom's

scattering cross-section. This can be viewed as the area of the atoms visible to the passing neutrons: the larger the scattering cross-section, the stronger the interaction. The scattering length of an atom, b, is used to calculated the cross-section, σ

$$\sigma = 4\pi b^2 \tag{2.1}$$

The cross-section is further differentiated into incoherent and coherent contributions. It should be noted that cross-sections not only vary from element to element but also between isotopes of the same element. For example, deuterium, an isotope of hydrogen, has a 40 times smaller incoherent cross-section and a 3 times larger coherent cross-section than hydrogen. In this study, deuterium is often used to reduce the large incoherent contribution and increase the coherent contribution. This method is known as "deuterium labeling."

When neutrons interact with an atom, the scattering intensity includes both coherent and incoherent contribution. As shown in Figure 2.2, the coherent contribution provides information on the position of an atom relative to the position of other nearby atoms, and incoherent contribution provides information only to the position of an atom relative to itself. The design of the instrument determines whether the structure or mobility is measured. Structure can be measured with an instrument that detects the angle of the scattered neutrons, but does not necessarily differentiate neutron energy changes. In this case, the scattering is elastic and the coherent contribution provides information on the structure of the sample. Conversely, mobility can be measured if neutron energy changes are measured, and this type of scattering is inelastic. Figure 2.2 summarizes four types of scattering, and the controlling variables. The instruments used in this study are included below the type of scattering and discussed in the following subsections.

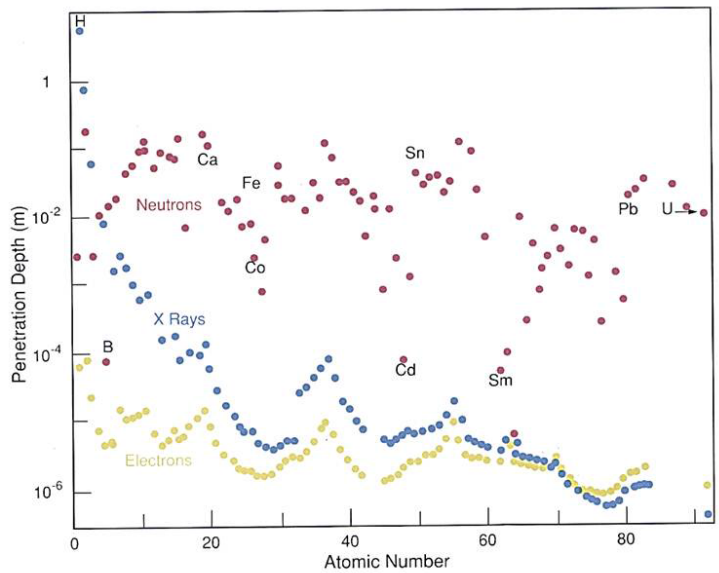

Figure 2.1: Dependence of penetration depth on atomic number for electrons, x-rays and neutrons. Penetration depth is defined where the beam intensity is reduced by a factor of 1/e (37%) to its original intensity. [1]

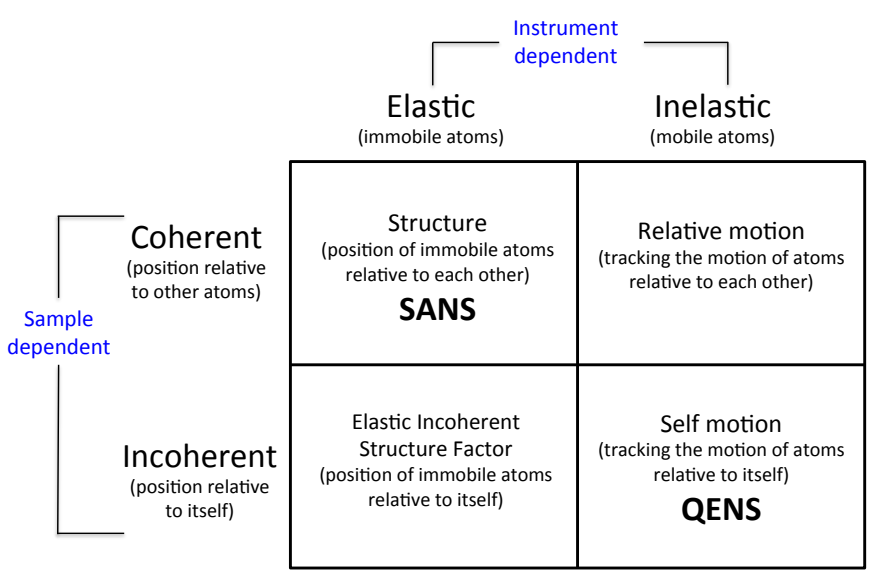

Figure 2.2: Neutron scattering variables and the corresponding neutron scattering techniques

2.2 Small Angle Neutron Scattering (SANS)

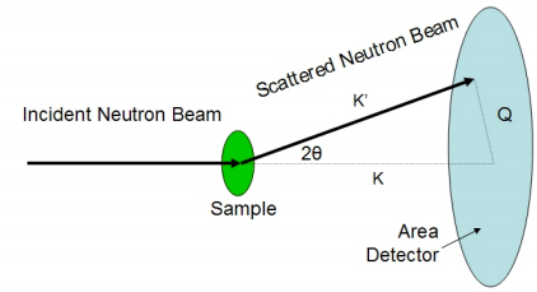

Figure 2.3: Schematic of a SANS measurement. The incident beam scatters from the sample at an able of 2θ. The scattered beam is detected on an area detector

Figure 2.3 illustrates the general idea of a SANS measurement. The incident neutron beam interacts with the sample, and neutrons are scattered at angle, 2θ. The scattered neutrons are then detected on a grid of detectors. K is the wave vector of incident neutrons and is inversely proportional to the wavelength (λ) of the neutrons, given by K = 2π/λ. Since SANS is an elastic measurement with no exchange of energy or momentum, K = K´. Using simple vector trigonometry, Q, the scattering vector, is given by the equation

$$Q = 2Ksin\theta = \frac{4\pi sin\theta}{\lambda}$$

The value of Q is inversely proportional to the distance being measured and the neutron wavelength. The SANS instrument at the NCNR can detect scattering angles from 0.08 to 16 degrees by adjusting the sample-to-detector distance. Using an incident neutron wavelength of 6Å, this correspond to Q range of 0.003Å^{-1} to 0.6Å^{-1}, equivalent to

spatial range of 10Å to 6000Å. To extend Q probe range, neutron wavelength is adjusted in the Extended Q-Range SANS at ORNL, which allows experiments reach a wider Q range of 0.002 $Å^{-1}$ to 1.4$Å^{-1}$.

What is needed in SANS measurements to provide contrast factors is the difference of scattering length density (not the scattering length). The scattering length density is defined as the ratio of the scattering length per molecule and per volume. Assuming a polymer has a repeat unit of A_mB_n, the scattering length density is calculated as:

$$\rho_{A_mB_n} = (b/v)_{A_mB_n} = (f_A b_A + f_B b_B)(m+n)/v = (mb_A + nb_B)/v \qquad (2.2)$$

Here mb_A+nb_B is the scattering length per molecule and v is the volume per molecule. For polymer composites, since the difference of volume per molecule between polymers is usually small, significant contrast always requires the replacement of hydrogen to deuterium. In the case of plant cell walls, scattering length densities of all polysaccharides change with the concentration of D_2O/ H_2O (see Figure 2.4). In a primary cell wall hydrated with H_2O, i.e. 0% D_2O solution, contrast between cellulose and xyloglucan (as well as other cell wall polysaccharide) is very small. Contrast gains as the D_2O concentration increases. It should be noted that the majority of scattering comes from the contrast between components to solvent at high water content systems such as primary cell wall. To observe a single specific component, it is necessary to minimize the coherent contribution of other objects in the same system. For example, to observe xyloglucan, the contrast between cellulose and water should be small, which suggests the use of 35% D_2O water solution. This technique is referred to "contrast match method," which is used to characterize the cell wall structure in Chapter 3 and Chapter 4.

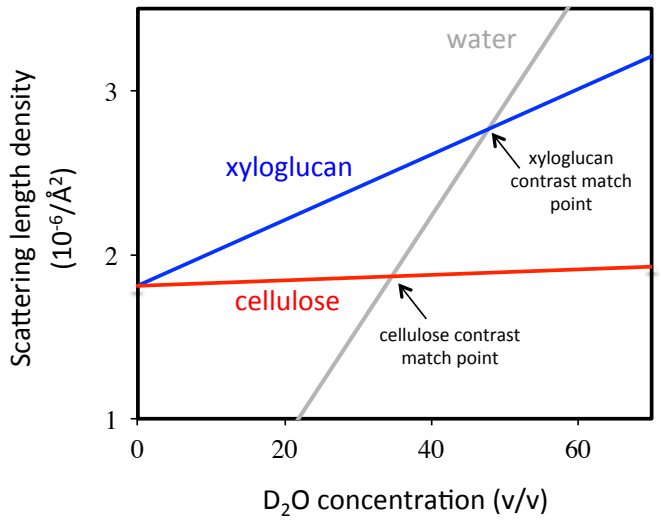

Figure 2.4: Contrast variation as a function of D_2O concentration

2.2 Dynamics: Quasi-Elastic Neutron Scattering [QENS]

In contrast to structure, mobility is determined by detecting the energy change of neutron during the scattering process. The type of neutron scattering is subdivided into elastic, inelastic and quasi-elastic scattering (see Figure 2.5). Neutron can scatter elastically (no energy change) or inelastically (some loss/gain of energy) depending o whether the neutron encounters immobile or mobile atoms in the sample. Quasi-elastic neutron scattering (QENS) is a special type of inelastic scattering where the neutrons have very small energy changes. The amplitude of energy change is affected by the mobility of atoms in the sample. Characterizing the width of QENS peak thus quantifies the molecular motion. To obtain the time probe range of 1–1000 ps, it requires three QENS instruments. In the subsection below we review the working principle of the QENS instruments in this thesis, namely Disk Chopper Time-of-Flight Spectrometer (DCS) and High Flux Backscattering Spectrometer (HFBS) at the National Institute of

Standard and Technology (NIST) and Backscattering Spectrometer (BSS) at Oak Ridge National Lab (ORNL).

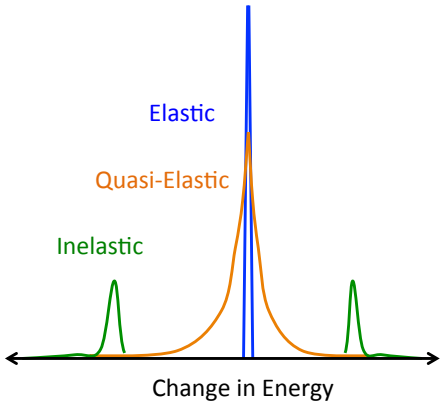

Figure 2.5: Examples of elastic, inelastic and quasi-elastic scattering. The x-axis represents the gain or loss in energy experienced by the neutron and the y-axis represents the number of scattered neutrons.

2.2.1 Disk Chopper Time-of-Flight Spectrometer [DCS]

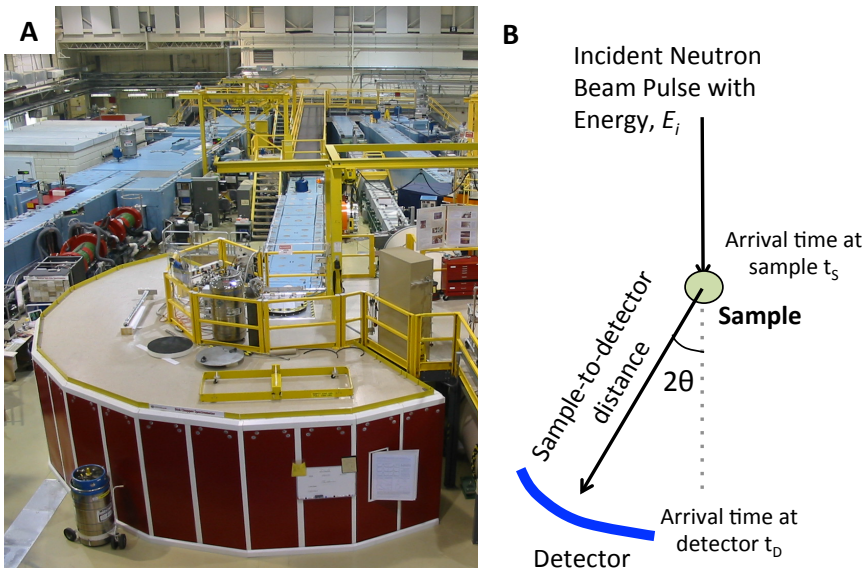

Figure 2.6: (A) The DCS instrument at the NCNR (B) Schematic of DCS time-of-flight measurement: a pulse of neutrons arrives at the sample and some neutrons are scattered at angle 2θ.

The DCS instrument (see Figure 2.6 A) can be used for both inelastic and quasi-elastic neutron scattering experiments. The incident neutrons can be controlled to have wavelength of 2–9 Å with initial energy (E_i) of 15–1500 μeV. The final energy (E_f) is calculated by the final velocity, which is obtained by the ratio of sample-to-detector distance to the time neutron travels the distance. The energy transfer is subtracted from the initial energy to final energy. Based on the scattering angle, we can calculate the energy exchange as a function of momentum transfer, Q. A schematic of time-of-flight geometry is illustrated in Figure 2.6 B.

The DCS probe range in time and space is illustrated by kinetic allowed region plot (see Figure 2.7). In the current case, neutron wavelength of 4.8Å and medium resolution mode are used, corresponding to energy resolution of 57 μeV. The upper time limit is calculated by the product of Planck's constant and inverse energy resolution, which yields 70 ps. On the other hand, the lower time limit is obtained by the left boundary of kinetic allowed region, slightly varying with Q values and is about 1 ps. The red line at represents the maximum energy loss that can be captured by the instrument at this configuration. The accessible Q range is established by the limits of the region (blue lines) when the elastic peak is observed (energy loss is zero).

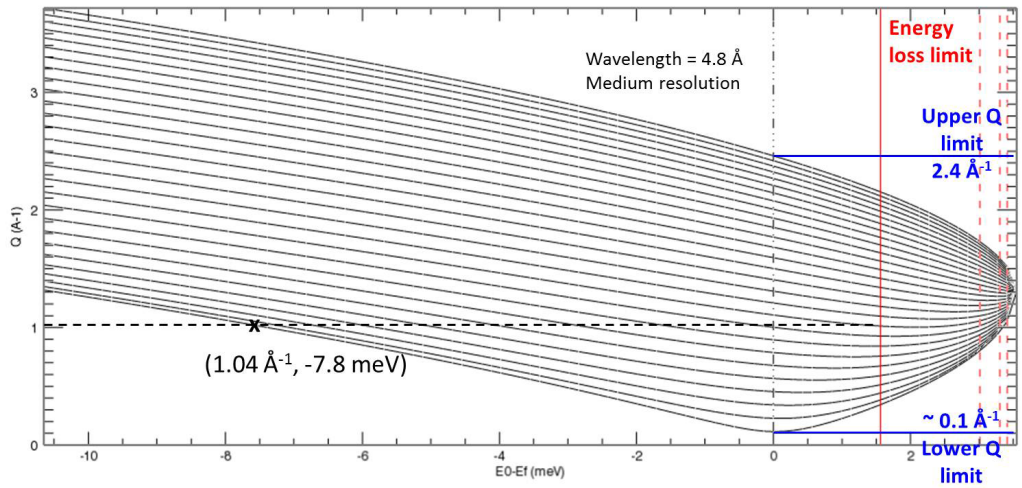

Figure 2.7: The kinetic allowed region for DCS at λ = 4.8Å, medium resolution

2.2.2 Backscattering Spectrometer (BASIS)

Both the BASIS (see Figure 2.8) and the DCS are time-of-flight spectrometers. The working principles are similar except the BASIS utilizes an inverted scattering geometry where the final energy of neutrons is selected using analyzer crystals. The inverted geometry minimizes the energy resolution down to 3.0–3.5 μeV at the elastic peak. The very fine resolution enables measurement to probe time scale at 40 to 800 ps, with a spatial scale of 0.2 to 2.0 Å^{-1}.

Figure 2.8: BASIS instrument at SNS, ORNL

2.3 Morphology: Field-Emission Scanning Electron Microscopy [FESEM]

Very fine resolutions are required to imagine the morphology of plant cell walls in nanometer scale. The resolution of a microscope is limited by both the quality of detector and the wavelength of the wave. Physically, diffraction bands cannot form from two objects that are closer than half of the wavelength of the wave, i.e., two distinct objects would appear as one. In order to obtain greater resolution we need shorter wavelengths. Electron microscopes serve as a better tool than optical microscopes on this purpose. In this work, field-emission scanning electron microscopy [FESEM] is used.

FESEM uses a field emission cathode in the electron gun to generate electrons. Very fine wavelengths are achieved by high-voltage electron incident gun. These electrons experience many electromagnetic lenses and apertures before they are incident on the sample. As electrons penetrate the surface and interact with the sample, emission of electrons, x-rays, and photons occurs as shown in Figure 2.9. Of all the emitted waves, the secondary electrons and backscattered electrons are collected to image the samples in

this work. Secondary electrons are ejected from k-shell of atoms by inelastic scattering interactions with incident electron beam that originate from the sample surface. Thus they contain more information about surface topography. Backscattered electrons originate by elastic scattering from the sample bulk. The electrons penetrate into the sample bulk, and the backscattered electrons are sensitive to atomic mass of the nuclei they scatter from and thus provide more elemental contrast and information about sample composition. The biggest advantage of FESEM technique is the ease of sample preparation. Because the FESEM samples are generally thicker than a few hundred nanometers, electrons are either scattered or absorbed before they transmit through the sample.

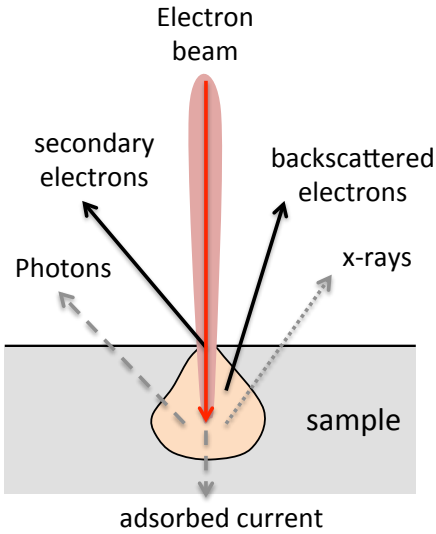

Figure 2.9: Schematic of FESEM setup. The electron beam reflects from the sample with backscattered electrons, secondary electrons that will be collected for imaging and meanwhile this process produce photons, x-rays and some of the wave is adsorbed or transmitted to sample.

Chapter 3 Conformation of Polysaccharides in Arabidopsis Primary Plant Cell Walls

This chapter is adapted from the author's manuscript: Shih-Chun Huang, Yong Bum Park, Daniel J. Cosgrove and Janna K. Maranas. In preparation.

We determine the primary cell walls molecular architecture of wild-type and xyloglucan-deficient *Arabidopsis thaliana*. By using small-angle neutron scattering with contrast match method, distinct measurements on cellulose microfibrils and non-cellulosic matrix polysaccharides are achieved. The contrast between wall components arises from the differences of the water permeability and the degree of labile proton exchange in D_2O. Our results show that the diameter of cellulose microfibrils is 2.7 nm, with portions coated with non-cellulosic matrix polysaccharides. In contrast to the current knowledge on the wall architecture, we conclude that the non-cellulosic matrix polysaccharides coat only 5–25% microfibril surface instead of fully coverage. Most of the non-cellulosic polysaccharides form extended coils in a good solvent, potentially acting as spacers between cellulose microfibrils. A cell wall model that incorporates these features is presented.

3.1 Introduction

Polysaccharide-rich primary cell walls play important roles in plant growth, development, morphogenesis and intercellular transport. To control cell growth and provide mechanical strength, primary cell walls must be dynamic enough to allow the cells to expand and simultaneously strong enough to withstand the cell turgor pressure. Despite much research, debate about primary wall architecture and how it influences wall extensibility still remains [1,2]. Primary wall is a complex polymer composite including three classes of polysaccharides: cellulose, hemicelluloses and pectins [2]. It may be regarded as a viscoelastic composite similar to fiberglass, with stiff microfibrils of crystalline cellulose embedded in a matrix of hydrated noncrystalline polysaccharides. Alternatively, the current cell wall model, based on biochemical extraction [3–7] and electron microscopy [8–10], envisions a more structured network, in which cellulose microfibrils are tethered together by the hemicellulose chains to form a load-bearing scaffold embedded in a pliant hydrogel made of pectins [11]. Detail information on the molecular structure of wall polymers, particularly non-cellulosic polysaccharides, is needed but not available.

The most well-understood wall component is cellulose, which exists as long microfibrils assembled from linear glucan chains [12]. Intrachain and interchain hydrogen bonds arrange the chains into highly crystalline microfibrils with a diameter of 2–5 nm [13,14]. Microfibrils can be directly visualized using atomic force microscope [15–18] and electron microscope [8,19], in which bundling of microfibrils can be observed. In contrast to cellulose, scarce information on the conformation of non-cellulosic matrix polysaccharides in cell wall has been reported. Cell wall models have depicted that

xyloglucan, the primary hemicellulose in higher plants, plays an essential role in cell wall architecture [3,8,20]. Those models suggest that xyloglucan forms a load-bearing network with cellulose, and it is present in three hypothetical domains [3]: tethers, loops and free stands between microfibrils; tight coating on microfibril surface; intertwined domain formed with microfibril. This notion is further strengthened by adsorption tests, which indicate xyloglucan binds to cellulose stronger than any other wall polysaccharides [21,22]. For the past two decades, the model has dominated the modern plant biology field. It however conflicts with multiple recent findings. The model predicts xyloglucan hydrolysis should lead to wall creep, which is not consistent with latest result [6]. The model also suggests extensive interaction between xyloglucan and surface cellulose, which is against NMR studies [23,24]. Other configurations and roles for xyloglucan have been proposed, including the spacer between microfibrils to maintain interfibril distance [25,26] or the xyloglucan-cellulose amalgam to strengthen wall mechanical property [6,27]. Despite the debates of its function and structure, xyloglucan is still regarded as an indispensible component for wall integrity, so it was surprising when the xyloglucan-deficient mutant Arabidopsis (xylosyltransferase1 and xylosyltransferase2, *xxt1/xxt2*) was developed and showed only minor growth defects [28]. It is speculated that other matrix polysaccharides (pectin or other hemicelluloses) play xyloglucan's mechanical role in *xxt1/xxt2*, but compositional analysis [28,29] and NMR analysis [30] do not yield strong conclusion on this point. Thus, it is also important to elucidate the structure and the function of pectins in the primary wall, and more specifically, address how cellulose, pectins and hemicelluloses (xyloglucan and non-xyloglucan) influence each other and compose an integrated wall.

Although there is an increasing interest in determining cell wall architecture, it is difficult to determine wall structure that simultaneously comprises cellulose microfibrils, hemicelluloses and pectins. Many wall models are derived on the basis of sequential chemical extraction analysis, which may yield the correct fraction of polysaccharides, but not necessarily provide exact polysaccharide arrangement and location. Common probes in determining polymer structure such as electron microscopes and x-ray scatterings are not capable to produce the complete wall architecture because these measurements either preferentially detect microfibril or fail to make distinct measurements on different wall components. To resolve this limitation, we use small-angle neutron scattering (SANS), which could probe conformational structure of polymer and has been used to investigate the diameter, interfibril distance and disorder periodicity of cellulose microfibril [31,32]. Because of the low contrast between wall polysaccharides, SANS has not been used to elucidate the molecular structure of other polysaccharides in cell wall. We increase the contrast among wall polysaccharides by applying selective deuterium labeling. Despite the molecular similarity between wall polysaccharides, there is a significant difference in their water permeability. Hemicelluloses and pectins are more permeable to water than cellulose as they do not form highly crystalline structure. We induce a discrepancy in cellulose and other wall components by submerging cell walls in D_2O, which allows more H/D exchange in matrix polysaccharides than in the microfibrils [13]. Since hydrogen and deuterium differ in neutron scattering length, difference in hydrogen/deuterium exchange provides contrast in SANS. We combined this advantage with the application of contrast match method [33]. In SANS measurements, scattering intensity increases with the scattering length density difference between component and

solvent. When component and solvent share the same scattering length density, there is no contribution from the component to the SANS spectrum. The SANS measurement under a contrast-matched condition is therefore highlighting the other component structure. In this case, we vary the percentage of D_2O in water to prepare cellulose-matched samples to observe matrix polysaccharides against a background of cellulose/solvent, and matrix-polysaccharide-matched samples to observe cellulose against a background of matrix polysaccharides/solvent.

In this article, we study the structure of xyloglucan and pectin in cell wall architecture by comparing primary specimens from wild-type (WT) and xyloglucan-deficient (*xxt1/xxt2*) *Arabidopsis*, and comparing cell walls prior and after partial pectin removal. Based on the analysis of structure, location, dimension and fraction of each wall component in each type of the cell walls, we bring an integrated structure of primary cell wall that most accurately describes the wall samples and challenges the conventional model.

3.2 Materials and Methods

Cell Wall Samples.

Cell walls were extracted from aerial tissues of 4-week-old WT and xxt1/xxt2 Arabidopsis. To remove chlorophylls, fresh samples were boiled in 95% ethanol for 5 min and washed 3 times with 95% ethanol. The samples were washed 3 times with ice-cold de-ionized distilled water (ddH2O), followed by homogenization with a minimum volume of ddH2O. Each homogenate was centrifuged at 6,000g at 4°C for 15 min and sequentially treated with 1.5% and 0.5% SDS to remove wall proteins. The recovered cell walls were consecutively washed with acetone, methanol:chloroform (1:1 v/v), 100%

ethanol, and water 3 times in each solution. Starch in the wall samples was removed with 500 units of α-amylase from porcine pancreas (Sigma-Aldrich) in 50 mM Hepes (pH 6.8) for 5 h at 37°C. First, pectin in the walls was extracted 3 times with 50 mM CDTA (pH 6.8) for at least 3 h at room temperature and further extracted 3 times with 50 mM Na2CO3 containing 20 mM NaBH4 for at least 3 h at room temperature. The remaining pectin and xylan in cell walls were sequentially removed by each 20 unit of pectate lyase (Megazyme) in 20 mM Tris-HCL (pH 9.5) containing 1 mL CaCl2 and xylanase M4 (Megazyme) in 50 mM sodium acetate (pH 5.0) for 5 h at 27°C. The recovered cell walls were washed with water 5 times and dried with freeze-dryer.

Cell Wall Composition Analysis.

WT and *xxt1/xxt2 Arabidopsis* cell walls (~ 3 mg) used for SANS experiment was incubated with 1 mL of 2 M trifluoroacetic acid (TFA) at 121°C for 1 h. The supernatant was collected and dried under air-flow. The dried 2 M TFA soluble wall component was resuspended in ddH_2O for high performance anion exchange chromatography (HPAEC) analysis. The 2 M TFA insoluble residue was incubated with 1 mL of 72% H2SO4 at room temperature for 1 h. The slurry of 72% H_2SO_4 was diluted with ddH_2O at 2 M concentration, further hydrolyzed at 100°C for 2 h with frequent vortexing (~ every 15 min), and neutralized with ammonium hydroxide (NH_4OH). For HPAEC analysis, TFA and H_2SO_4 solubilized samples were filtered with a 0.1 μm centrifuge filter (Amicon). Monosaccharaides were analyzed with a Dionex Carbo PA-20 column at a flow rate of 0.5 mL min-1 under 0.1 M NaOH isocratic condition for first 15 min and then under linear gradient condition for 20 min from 0.1 M NaOH to a 0.1 M NaOH and 0.1 M sodium acetate (1:1. v/v) mixture, and detected with a pulsed amperometric detection.

SANS Experiments.

SANS experiments were performed using the NG-7 SANS [34] at National Institute of Standards and Technology (NIST), Gaithersburg, MD and the CG-3 Bio-SANS [35] at Oak Ridge National Laboratory (ORNL), Oak Ridge, TN. SANS profiles were obtained by azimuthally averaging the processed 2D images, which were normalized to incident beam monitor counts and corrected with detector dark current, pixel sensitivity, and empty beam scattering. Samples were contained in quartz cells with 1 mm path length. Data were corrected for detector efficiency, background radiation, empty cell scattering, and incoherent scattering to absolute scale. The processing of data was performed using Igor Pro (WaveMetrics) with the NIST analysis macro plugin [36]. To control the relative amount of H2O and D2O, samples under contrast-matched conditions were freeze-dried and rehydrated in contrast-matching condition. Before conducting the SANS measurements, samples were soaked for 12 hours for hydroxyl exchange to reach equilibrium [37].

Contrast Variation Experiments.

Pure components of cellulose (prepared by Gluconacetobacter xylinus), xyloglucan (from tamarind seeds, Megazyme) and a non-xyloglucan hemicellulose (xylan, from birchwood, Sigma) were prepared in D_2O/H_2O solvents that have D_2O fraction from 0–100%. SANS experiments on above samples were conducted, and the intensities were individually integrated from Q of 0.02 to 0.4 $Å^{-1}$ after subtracting incoherent background scattering. Match points, giving minimum coherent scattering intensity, are 35.0% D_2O for cellulose, 48.1% D_2O for xyloglucan, 49.0% D_2O for xylan and 48.8% D_2O for pectin.

SANS Fitting Model

Our scattering model for cellulose considers three contributions to the total scattering intensity, namely polydisperse cylinder for cellulose microfibril and power-law scattering for fractal dimension, and incoherent scattering background. The three contributions combine to give the following scattering model,

$$I(Q) = P_{cyl}(Q) + BQ^{-n} + D$$

The scattering intensity of polydisperse cylinder model is described as

$$P_{cyl}(Q) = \frac{scale}{V_{poly}} \int_0^x f(r) \int_0^{\pi/2} F^2(Q,\alpha) \sin(\alpha) d\alpha$$

$$V_{poly} = \pi r^2 L \left(\frac{z+2}{z+1}\right)$$

where $P_{cyl}(Q)$ is the single cylinder chain form factor, $f(r)$ is the normalized Schulz distribution of the radius, α is the angle between the cylinder axis and the scattering vector Q, L is the cylinder length, and z is the Schulz polydispersity. The limits of the integration are adjusted to cover the full range of radius. The calculation is normalized to the polydisperse volume using the second moment. The scattering amplitude F is addressed as

$$F(Q,\alpha) = 2V_{cyl}(\rho_{cyl} - \rho_{sol}) \frac{sin(QHcos\ \alpha)}{QHcos\ \alpha} \frac{j_1(Qr\ sin\ \alpha)}{Qr \sin \alpha}$$

where $j_1(x)$ is the first order Bessel function, and H is half the cylinder length. The scattering of the cellulose microfibril network at low Q can be described as a fractal

object. A fractal object has a power-law scattering that is added as a second term. Lastly, incoherent scattering mainly from hydrogen provides no structural information (q-independent), and this term is incorporated as a constant *D*.

Our scattering model for hemicellulose considers three contributions to the total scattering intensity, namely correlation length model for polymer chain, and polydisperse core-shell cylinder model for coating around cellulose microfibril, and incoherent scattering background. The scattering intensity of correlation length model is described as

$$I_{polymer}(Q) = AQ^{-n} + \frac{B}{1 + (Q\xi)^m}$$

The first term describes power-law scattering from fractal object (exponent=*n*) and the second term is a Lorentzian function describing polymer chain (exponent=*m*). ξ is the correlation length of the polymer chains. This second term characterizes the polymer/solvent interaction and therefore presents the thermal dynamics.

The form factor for polydisperse core-shell cylinder (similar to polydisperse cylinder) is

$$P_{cscyl}(Q) = \frac{scale}{V_{shell}} \int_0^{\pi/2} F_{cs}^2(Q, \alpha)\, \alpha \sin \alpha \, d\alpha$$

$F_{cs}(Q,\alpha)$ describes scattering from both cylinder core and cylinder shell to solvent. Since the cylinder core (cellulose microfibril) is contrast matched in the experiment. $F_{cs}(Q,\alpha)$ can be simplified as

$$F_{cs}(Q,\alpha) = 2(\rho_{shell} - \rho_{solv})V_{shell}j_0(QHcos\ \alpha)\frac{J_1(Q(r+t)\sin\alpha)}{Q(r+t)\sin\alpha}$$

where t is the thickness of the shell. Eventually, the combined model for hemicelluloses and pectins becomes

$$I(Q) = I_{polymer}(Q) + P_{cscyl}(Q) + D$$

3.3 Results and Discussion

Samples were obtained from aerial tissues of 4-week-old WT and *xxt1/xxt2 Arabidopsis*, in which secondary thickening is negligible [41]. Thus, the samples used for the SANS experiment contains mostly primary walls. Table 3.1 shows the component analysis by methanolic hydrochloric acid extraction. As expected, *xxt1/xxt2* contains no xyloglucan at both untreated and depectinated states. The depectinated procedure is chosen to avoid extraction of hemicellulose and preserve cellulose-hemicellulose interaction [42,43]. Component analysis confirms that pectin/cellulose ratios are largely reduced whereas hemicellulose/cellulose ratios are only mildly affected. Partial pectins still remain in the composites result from their association with hemicelluloses and cellulose through covalent bond and hydrogen bonds. Further removal of pectins from cell wall is possible, but it requires harsh treatments such as applying concentrated acid or enzymatic breakdown that will cause unwanted change on cellulose-hemicellulose interactions.

Table 3.1. Component analysis of WT and *xxt1/xxt2* at untreated and depectinated states. Units: mole % based on total sugars. (±: standard deviation, n=3)

Sample name	Cellulose %	Hemicellulose %		Pectin %
		Xyloglucan	Others	
Untreated WT	13.5 (±1.3)	15.1 (±0.3)	7.1 (±0.2)	64.3 (±0.8)
Untreated *xxt1/xxt2*	17.3 (±0.4)	0	11.4 (±0.5)	71.4 (±0.2)
Depectinated WT	39.2 (±07)	22.9 (±1.9)	14.8 (±0.9)	23.1 (±0.4)
Depectinated *xxt1/xxt2*	54.5 (±0.3)	0	16.6 (±0.3)	29.9 (±0.2)

Samples are measured under contrast-match conditions, in which the scattering length density of the solvent and the component to be matched is equivalent. To determine the match point of each component, we prepared samples containing only one component among cellulose, xyloglucan, non-xyloglucan hemicellulose, and pectin. Measurements on single component samples are performed at various H_2O/D_2O ratios ranging from 0–100% D_2O. The contrast match point is determined at the D_2O ratio giving the lowest scattering intensity. Following the procedure, we determine that the match point of the cellulose microfibril is 35% D_2O, consistent with literature value [31,44]; and the match points of the xyloglucan, the non-xyloglucan hemicellulose, and the pectin are all about 48% D_2O.

Cellulose-highlighted measurements

We examine the structural role of cellulose in the primary wall by comparing the cellulose-highlighted (matrix-polysaccharide-matched) SANS spectra as shown in Figure 3.1. Since samples have similar dry mass, suppressing SANS intensities in untreated cell walls confirms their low cellulose content and validates contrast matching of other matrix

polysaccharides. Based on the known feature of cellulose microfibrils, high aspect ratio object is required to fit the cellulose-highlighted spectra. We use the form factor of cylinder with polydisperse radius to describe individual microfibril at high Q (smaller length scale) and a power law model to describe the network formed by multiple microfibrils at low Q (large length scale). Fitting parameters are summarized in Table 3.2. The average diameters are similar among these four cell walls at around 2.7 nm, which is ~10% less than NMR estimation on *Arabidopsis* [24] and consistent with the diameter found in other plant tissues [8,18]. It is worth noted that the polydispersity does not change after depectination and is smaller in *xxt1/xxt2*. Since the *xxt1/xxt2* mutation does not alter the mechanism of cellulose synthesis [28], it suggests that xyloglucan affects cellulose chain assembly. The interaction between xyloglucan and cellulose may change the microfibril structure by altering the cellulose interfibril H-bonding [45]. Alternatively, xyloglucan can become trapped inside the microfibril during the early stage of cellulose formation. The average length of cellulose microfibrils reaches to hundreds nm, which is difficult to be accurately determined as low-Q SANS feature (large length scale) is dominated by power-law scattering. The power law scattering arises from objects larger than the upper length limit of this SANS experiment (200 nm). The value of power can be regarded as a self-similar structure (mass fractals) and its structure factor [46]. Higher value of mass fractal indicates more packed space filling. Both WT and *xxt1/xxt2* have similar mass fractal in their untreated state, suggesting the spatial arrangement of microfibrils in WT and *xxt1/xxt2* are similar packed, agrees with NMR conclusion on *Arabidopsis* [30]. The special arrangements in the depectinated walls differ significantly from that of untreated walls. The higher fractals in the depectinated walls indicate that

pectin removal results in more densely microfibril packing. The change is less significant in WT, suggesting that xyloglucan can work as spacer between cellulose microfibrils.

The power law and cylinder models are fit independently. The gap between the two models describes the size scale that is more than a single microfibril but less than microfibril network. This gap is then equivalent to the range of interfibril distance (list in Table 3.2). For untreated walls, results are consistent with available data on primary walls in various plant species and tissues [8,10,18]. The minimum and maximum interfibril distances are reduced upon depectination, indicating microfibrils collapsed after depectination, especially in the *xxt1/xxt2*. The change of interfibril distance and fractals of microfibril upon depectination agree with each other and both highlight the spacer role of pectins in cell walls. The sum of the cylinder and the power law model provides a good description of the spectra throughout the spatial range of the SANS experiment, including the gap between the two models. This suggests that there are no structures on intermediate length scales have noticeable contribution to the scattering.

Table 3.2. Characteristics of cellulose microfibrils in the WT and *xxt1/xxt2 Arabidopsis* walls under untreated and depectinated conditions. Standard errors are shown in parenthesis.

Cellulose features	Untreated		Depectinated	
	WT	*xxt1/xxt2*	WT	*xxt1/xxt2*
Diameter (nm)	2.74 (0.24)	2.76 (0.20)	2.73 (0.18)	2.72 (0.04)
Schultz polydispersity	0.17 (0.15)	0.08 (0.10)	0.15 (0.12)	0.07 (0.06)
Fractal	2.74 (0.07)	2.71 (0.05)	2.89 (0.03)	3.01 (0.01)
Interfibril distance (nm)	25–50	25–50	21–50	18–35

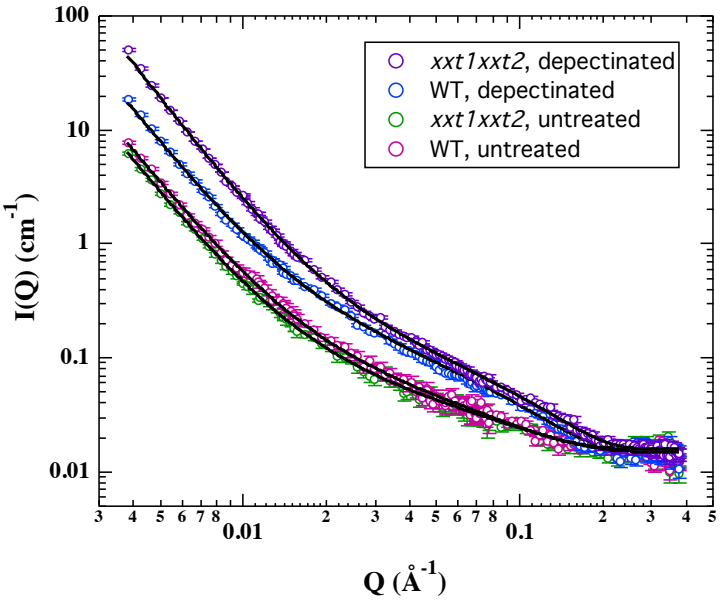

Figure 3.1. SANS cellulose-highlighted profiles for WT and *xxt1/xxt2 Arabidopsis* cell wall before and after depectination in absolute scale. Measurements were performed in 48% D_2O to highlight the structure of cellulose microfibril. Fitting lines (black lines) are overlaid for each data set and parameters are shown in Table 3.2.

Coating on Microfibril

Matrix-polysaccharide-highlighted (cellulose-matched) measurements on cell walls examine the structure of matrix polysaccharides. The matrix-polysaccharides-highlighted spectra are plotted and fitted using the cylindrical shell model and the correlation length model as shown in Figure 3.2. The cylindrical shell model is used to determine whether matrix polysaccharides form coating shell on microfibrils. This model identifies the thickness and the length of coating shell, and the volume fraction of coating shell. The model however does not describe matrix polysaccharides that do not form a complete shell on the microfibril surface, i.e. the polysaccharides that interact with microfibril with only a few monomers are not included in this model. The coating feature

in untreated WT and *xxt1*/*xxt2* walls is not obvious. Since both walls are abundant in pectins, suggesting that pectins do not form strong interactions with cellulose microfibrils. This is consistent with previous studies that pectins can be easily removed by mild treatments such as dilute alkali or hot water. To determine an accurate coating fraction in untreated cell walls is challenging because the matrix-polysaccharides-highlighted scattering is dominated by another correlational length model feature. Alternatively, as depectination is known to have minor influence on cellulose-hemicellulose interaction, one can more accurately determine the coating fractions by measuring the depectinated walls. Table 3.3 shows fitting parameters used for depectinated cell walls. At depectinated state, WT has notably larger fraction of coated cellulose microfibrils compared to *xxt1*/*xxt2*. Since the main difference between the two cell walls is that *xxt1*/*xxt2* lacks xyloglucan, we conclude that the extra coating found in WT is caused by xyloglucan-cellulose interaction. Both the coating fraction and the dimension of coating regions are reduced in *xxt1*/*xxt2*. The coating in *xxt1*/*xxt2* is 33% thinner and 65% shorter than that in WT. Based on the volume fraction of shell structure, we calculate the fraction of polysaccharides participating in coating: in *xxt1*/*xxt2*, 7% of the matrix polysaccharides form coating; and in WT, the coating region consist of 51% of xyloglucan. The difference shows that xyloglucan coats cellulose microfibrils. These results are comparable to *in vitro* adsorption isotherm test: the amount of xyloglucan adsorbed to cellulose surface is more than 5 folds greater than that of pectins [47]. The coating feature in depectinated cell wall has a uniform thickness of 0.9 nm. The thickness is at the same size of one xyloglucan chain, suggesting xyloglucan forms only a single layer of coating. This means that the interaction between free xyloglucan and coating

xyloglucan is not strong enough to seed additional layers. The average inner diameter of the coating in WT is 3.2 nm, 0.5 nm wider than the average diameter found in cellulose-highlighted experiment, suggesting that xyloglucan preferentially coats wider region of cellulose microfibril, perhaps at the sites where xyloglucan is entrapped [3,30] or the sites where cellulose is disordered [31,48]. We also determine that the polydispersity of cellulose diameter is smaller in *xxt1/xxt2*. Thus the large diameter microfibrils are much fewer to anchor coatings. Cellulose coating domain is believed to contribute to the wall mechanical strength, particularly when two coated cellulose microfibrils are in close contact and function as biomechanical "hot-spots" [6]. Recent studies show that the *xxt1/xxt2* wall is 20–50% weaker compared to the WT wall [28,29], which can be explained by our conclusion of low coating fraction in *xxt1/xxt2* and the "hot-spots" theory.

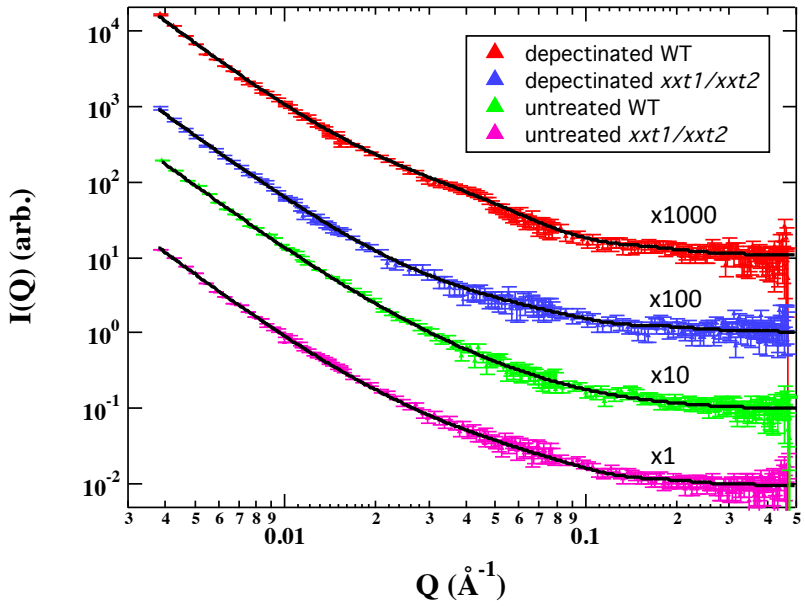

Figure 3.2. SANS cellulose-matched profiles (points) for WT and *xxt1/xxt2 Arabidopsis* cell wall before and after depectination. Measurements were performed in 35% D_2O to

highlight the structure of non-cellulose wall polysaccharides. Fitting lines (black lines) are overlaid for each data set and data are shifted for clarity.

Table 3.3. Characteristics of the core-shell features in WT and *xxt1/xxt2 Arabidopsis* cell walls under depectinated condition. Standard errors are shown in parenthesis.

Coating features	Depectinated	
	WT	*xxt1/xxt2*
Cellulose coated ratio (%)	25.0 (5.7)	4.7 (3.1)
Coated length (nm)	12.6 (2.5)	4.5 (4.0)
Core diameter (nm)	3.2 (0.3)	3.0 (0.3)
Shell thickness (nm)	0.9 (0.2)	0.7 (0.3)

Correlation Length

The structure of other matrix polysaccharides that are not in the coating form is described by correlation length model, which has been used for polymer solution and hydrogel [38,49,50]. Correlation length model is important to describe the scattering feature of matrix-polysaccharide-highlighted samples in the low Q range. The correlational length charateristics are listed in Table 3.4. Although polysaccharides in the wall are confined and influenced by cellulose microfibrils, much of it resemble the chain conformation as in dilute water solution [51], behaving like chains with excluded statistics (good solvent). The function of the coil domain is not clear. Coils might simply presense as space fillers. For example, our recent work demonstrated that removing xyloglucan in this domain does not lead to wall creep [6]. The correlation length characterizes the average distance between chain entanglements and is proportional to the individual coil sizes in the dilute region [50,52]. There is a negative effect of concentration on correlation length [50]. Before the depectination treatment, walls have

higher matrix polysaccharide concentration, as a result, chains interact more extensively and the average size is smaller. In the untreated walls, pectins dominate in the matrix-polysaccharides-highlighted spectra, the presence of xyloglucan is less important in determining the correlation length. The difference in correlation length between untreated WT and *xxt1/xxt2* is small. Once the pectin amount is reduced, correlation length for both walls increases. Depectinated WT has larger correlation length that is because WT has long xyloglucan chains and increases the average mesh size. The SANS spectra for non-cellulose polysaccharides also show a power-law scattering at low Q regions. Possibilty for the origin of power-law scattering is similar to those for microfibrils and includes additional options as individual non-cellulose polysaccharides are solvated in water. For example, for poly(ethylene oxide)(PEO) solvated in water, power-law scattering at low Q is observed when chains are aggregated. The power law scattering describes a large aggregated cluster, allowing an excluded volume parameter to be extracted from the exponent. In the present measurements and PEO/water solutions [38,39], the excluded volume parameter indicates a cluster with self-attraction. Physically, this means that although the monomers in the same chain follow a self-avoiding walk, monomers on different chains can follow a self-attracting walk. Such behavior could arise through interactions between polysaccharide segments that are more hydrophobic [53] or crosslinks between acidic pectin and Ca^{2+} [11,30]. In Figure 3.3, we provide a schematic that summarizes our results on the distinct measurements on cellulose and non-cellulose polysaccharides. The schematic is made to scale and incorporates the microfibril diameter, coating length, coating thickness, and interfibril tethers.

Table 3.4. Characteristics of the correlational length features of non-cellulose polysaccharides in WT and *xxt1/xxt2 Arabidopsis* walls under untreated and depectinated condition. Standard errors are shown in parenthesis.

	Depectinated		Untreated	
	WT	*xxt1/xxt2*	WT	*xxt1/xxt2*
Correlational length (nm)	11.9 (2.7)	8.8 (2.4)	7.5 (1.8)	6.9 (1.6)
Low-Q Fractal	3.02 (0.00)	2.88 (0.04)	2.87 (0.02)	2.91 (0.01)

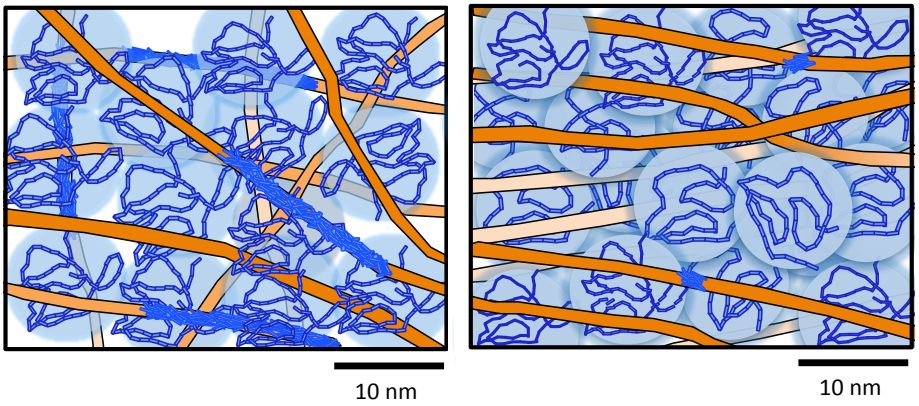

Figure 3. WT (left) and *xxt1/xxt2* (right) *Arabidopsis* primary wall schematics based on SANS results. The thick orange rods represent cellulose microfibrils, and the thin blue lines are matrix polysaccharides. The matrix polysaccharides may form coil structures functioning as interfibril fillers and coating domains around cellulose microfibrils.

3.4 Conclusion

In this article, we provide new insight on the structure of the plant primary cell wall that partially conflicts with current views. Cellulose-highlighted measurements share features observed by atomic force microscope and electron microscope [8,18,54]. Matrix-polysaccharide-highlighted measurements are novel and provide support for limited microfibril coating and hydrogel structure between cellulose microfibrils. It appears that the majority of matrix polysaccharides form hydrogel network that may space and

cushion microfibril contacts, rather than functioning as taut chains that directly bear mechanical load [6]. Cellulose coating features are identified in different walls. The SANS result is in contract with the traditional notion, which believes most of the cellulose surface is coated, and this study is comparable with recent NMR studies estimating only a minority of the cellulose is interacting with xyloglucan [23,30]. Recently, some of us proposed that a small fraction of xyloglucan, which mediates contacts between microfibrils, functions as biomechanical "hot-spots" in primary walls. This theory is supported by our low fraction (25%) of the coated cellulose microfibril, and the fraction of coating in direct contact, analogous to hotspots, will be considerably less. *xxt1/xxt2* lacks xyloglucan biosynthesis, resulting in lower hemicellulose content and a more important role for non-xyloglucan hemicelluloses and for pectins. Although the absence of xyloglucan does not alter the average microfibril diameter, it does impact the interfibril distance, microfibril space filling and the microfibril coating content. The most important difference is the reduction of coating feature, which we believe a key factor leading to the weaker mechanic properties of *xxt1/xxt2* wall. Our results challenge current wall models and call for new interpretation of the role of xyloglucan in the plant primary cell walls.

3.5 Reference

1. Albersheim, P., Darvill, A., Roberts, K., Sederoff, R. & Staehelin, A. Plant cell walls: from chemistry to biology. (Garland Science, Taylor and Francis Group, LLC, 2010).

2. Cosgrove, D. J. Growth of the plant cell wall. Nat. Rev. Mol. Cell Biol. 6, 850–61 (2005).

3. Nishiyama, Y. Structure and properties of the cellulose microfibril. J. Wood Sci. 55, 241–249 (2009).

4. Kafle, K. et al. Cellulose microfibril orientation in onion (Allium cepa L.) epidermis studied by atomic force microscopy (AFM) and vibrational sum frequency generation (SFG) spectroscopy. Cellulose 21, 1075–1086 (2013).

5. Niimura, H., Yokoyama, T., Kimura, S., Matsumoto, Y. & Kuga, S. AFM observation of ultrathin microfibrils in fruit tissues. Cellulose 17, 13–18 (2009).

6. Ding, S.-Y. & Himmel, M. E. The maize primary cell wall microfibril: a new model derived from direct visualization. J. Agric. Food Chem. 54, 597–606 (2006).

7. Zhang, T., Mahgsoudy-Louyeh, S., Tittmann, B. & Cosgrove, D. J. Visualization of the nanoscale pattern of recently-deposited cellulose microfibrils and matrix materials in never-dried primary walls of the onion epidermis. Cellulose 21, 853–862 (2013).

8. McCann, M. C., Wells, B. & Roberts, K. Direct visualization of cross-links in the primary plant cell wall. J. Cell Sci. 96, 323–334 (1990).

9. McCann, M. C., Wells, B. & Roberts, K. Complexity in the spatial localization and length distribution of plant cell-wall matrix polysaccharides. J. Microsc. 166, 123–136 (1992).

10. Scheller, H. V. & Ulvskov, P. Hemicelluloses. Annu. Rev. Plant Biol. 61, 263–89 (2010).

11. Hayashi, T. Xyloglucan in the primary cell wall. Annu. Rev. Plant Physio. Plant Mol. Biol. 40, 139–168 (1989).

12. Park, Y. B. & Cosgrove, D. J. Changes in cell wall biomechanical properties in the xyloglucan-deficient xxt1/xxt2 mutant of Arabidopsis. Plant Physiol. 158, 465–75 (2012).

13. Cavalier, D. M. et al. Disrupting two Arabidopsis thaliana xylosyltransferase genes results in plants deficient in xyloglucan, a major primary cell wall component. Plant Cell 20, 1519–37 (2008).

14. Pauly, M., Albersheim, P., Darvill, A. & York, W. S. Molecular domains of the cellulose/xyloglucan network in the cell walls of higher plants. Plant J. 20, 629–639 (1999).

15. Lerouxel, O., Choo, T. S., Se, M., Lerouge, P. & Pauly, M. Rapid Structural Phenotyping of Plant Cell Wall Mutants by Enzymatic Oligosaccharide Fingerprinting 1. Plant Physiol. 130, 1754–1763 (2002).

16. Carpita, N. C. Hemicellulosic polymers of cell walls of zea coleoptiles. Plant Physiol. 72, 515–21 (1983).

17. Park, Y. B. & Cosgrove, D. J. A revised architecture of primary cell walls based on biomechanical changes induced by substrate-specific endoglucanases. Plant Physiol. 158, 1933–43 (2012).

18. Thompson, J. E. & Fry, S. C. Restructuring of wall-bound xyloglucan by transglycosylation in living plant cells. Plant J. 26, 23–34 (2001).

19. Carpita, N. C. & Gibeaut, D. M. Structural models of primary cell walls in flowering plants: consistency of molecular structure with the physical properties of the walls during growth. Plant J. 3, 1–30 (1993).

20. McCann, M. C. & Roberts, K. Changes in cell wall architecture during cell elongation. J. Exp. Bot. 45, 1683–1691 (1994).

21. Gu, J. & Catchmark, J. M. The impact of cellulose structure on binding interactions with hemicellulose and pectin. Cellulose 20, 1613–1627 (2013).

22. Dick-Pérez, M. et al. Structure and interactions of plant cell-wall polysaccharides by two- and three-dimensional magic-angle-spinning solid-state NMR. Biochemistry 50, 989–1000 (2011).

23. Bootten, T. J., Harris, P. J., Melton, L. D. & Newman, R. H. Solid-state 13C-NMR spectroscopy shows that the xyloglucans in the primary cell walls of mung bean (Vigna radiata L.) occur in different domains: a new model for xyloglucan-cellulose interactions in the cell wall. J. Exp. Bot. 55, 571–83 (2004).

24. Thompson, D. S. How do cell walls regulate plant growth? J. Exp. Bot. 56, 2275–85 (2005).

25. Talbott, L. D. & Ray, P. M. Molecular size and separability features of pea cell wall polysaccharides : implications for models of primary wall structure. Plant Physiol. 98, 357–68 (1992).

26. Zhao, Z., Crespi, V. H., Kubicki, J. D., Cosgrove, D. J. & Zhong, L. Molecular dynamics simulation study of xyloglucan adsorption on cellulose surfaces: effects of surface hydrophobicity and side-chain variation. Cellulose 21, 1025–1039 (2014).

27. Nishiyama, Y. et al. Periodic disorder along ramie cellulose microfibrils. Biomacromolecules 4, 1013–7 (2003).

28. Matthews, J. F. et al. Computer simulation studies of microcrystalline cellulose Ibeta. Carbohydr. Res. 341, 138–52 (2006).

29. Pai, S. S. et al. The conformation of the poly(ethylene glycol) chain in mono-PEGylated lysozyme and mono-PEGylated human growth hormone. Bioconjug. Chem. 22, 2317–23 (2011).

30. Heller, W. T. Small-angle neutron scattering and contrast variation: a powerful combination for studying biological structures. Acta Crystallogr. D. Biol. Crystallogr. 66, 1213–7 (2010).

31. Endo, H. et al. Membrane decoration by amphiphilic block copolymers in bicontinuous microemulsions. Phys. Rev. Lett. 85, 102–5 (2000).

32. Glinka, C. J., Barker, J. G., Hammouda, B. & Krueger, S. The 30m small-angle neutron scattering instruments at the National Institute of Standards and Technology. J. Appl. Crystallogr. 31, 430–445 (1998).

33. Lynn, G. W. et al. Bio-SANS—A dedicated facility for neutron structural biology at Oak Ridge National Laboratory. Phys. B Condens. Matter 385-386, 880–882 (2006).

34. Kline, S. R. Reduction and analysis of SANS and USANS data using IGOR Pro. J. Appl. Crystallogr. 39, 895–900 (2006).

35. Hishikawa, Y., Togawa, E., Kataoka, Y. & Kondo, T. Characterization of amorphous domains in cellulosic materials using a FTIR deuteration monitoring analysis. Polymer. 40, 7117–7124 (1999).

36. Hammouda, B., Ho, D. L. & Kline, S. Insight into clustering in poly(ethylene oxide) solutions. Macromolecules 37, 6932–6937 (2004).

37. Hammouda, B., Ho, D. & Kline, S. SANS from Poly(ethylene oxide)/Water Systems. Macromolecules 35, 8578–8585 (2002).

38. Hammouda, B. SANS from polymers—review of the recent literature. Polym. Rev. 50, 14–39 (2010).

39. Gendreau, E. et al. Cellular basis of hypocotyl growth in Arabidopsis thaliana. Plant Physiol. 114, 295–305 (1997).

40. Thompson, J. E. & Fry, S. C. Evidence for covalent linkage between xyloglucan and acidic pectins in suspension-cultured rose cells. Planta 211, 275–86 (2000).

41. Popper, Z. A. & Fry, S. C. Xyloglucan-pectin linkages are formed intra-protoplasmically, contribute to wall-assembly, and remain stable in the cell wall. Planta 227, 781–94 (2008).

42. Kennedy, C. J. et al. Microfibril diameter in celery collenchyma cellulose: X-ray scattering and NMR evidence. Cellulose 14, 235–246 (2007).

43. Park, Y. B. et al. Effects of plant cell wall matrix polysaccharides on bacterial cellulose structure studied with vibrational sum frequency generation spectroscopy and x ray Diffraction. Biomacromolecules 15, 2718–2724 (2014).

44. Teixeira, J. Small-angle scattering by fractal systems. J. Appl. Crystallogr. 21, 781–785 (1988).

45. Dick-Perez, M., Wang, T., Salazar, A., Zabotina, O. A. & Hong, M. Multidimensional solid-state NMR studies of the structure and dynamics of pectic polysaccharides in uniformly 13C-labeled Arabidopsis primary cell walls. Magn. Reson. Chem. 50, 539–50 (2012).

46. Zykwinska, A. W., Ralet, M. J. & Garnier, C. D. Evidence for in vitro binding of pectin side chains to cellulose. Plant Physiol. 139, 397–407 (2005).

47. Zhao, Z. et al. Cellulose microfibril twist, mechanics, and implication for cellulose biosynthesis. J. Phys. Chem. A 117, 2580–2589 (2013).

48. Hyland, L. L., Taraban, M. B., Hammouda, B. & Yu, Y. B. Mutually reinforced multicomponent polysaccharide networks. Biopolymers 95, 840–51 (2011).

49. Hammouda, B. & Ho, D. L. Insight into chain dimensions in PEO/water solutions. J. Polym. Sci. 45, 2196–2200 (2007).

50. Manet, S. & Jean, B. SANS measurements of semiflexible xyloglucan polysaccharide chains in water reveal their self-avoiding statistics Biomacromolecules 12, 3330–3336 (2011).

51. Hule, R. A., Nagarkar, R. P., Hammouda, B., Schneider, J. P. & Pochan, D. J. Dependence of self-assembled peptide hydrogel network structure on local fibril nanostructure. Macromolecules 42, 7137–7145 (2009).

52. Linder, Å., Bergman, R., Bodin, A. & Gatenholm, P. Mechanism of assembly of xylan onto cellulose surfaces. Langmuir 5072–5077 (2003).

53. Ding, S.-Y., Zhao, S. & Zeng, Y. Size, shape, and arrangement of native cellulose fibrils in maize

Chapter 4 Structure of Monocot and Dicot Primary Cell Wall Polysaccharides from Small-Angle Neutron Scattering

This chapter is adapted from the author's manuscript: Shih-Chun Huang, Yong Bum Park, Daniel J. Cosgrove and Janna K. Maranas.

Abstract

The polysaccharide structure in primary cell walls of cucumber, onion, maize, and wheat are investigated using Small-Angle Neutron Scattering (SANS). The plant species are selected across monocot and dicot plant species. Although these cell walls are microfibril-based, the dominant forms of hemicellulose for maize and wheat are mixed-linkage glucan and arabinoxylan while cucumber and onion is xyloglucan. The structural features of cellulose and the matrix polysaccharides are determined using contrast matching. The diameter of cellulose microfibrils in these walls range between2–6 nm and have an average diameter of ~3 nm, which agrees well with literatures. The cellulose surface is partially coated with hemicellulose, and the coated fraction is largely correlated to xyloglucan content. We also find that mixed-linkage glucan plays a role in coating the microfibril, suggesting that mixed-linkage glucan may adopt some xyloglucan function in monocots.

4.1 Introduction

Cell walls play important biological functions in plants. Each plant cell is encased in its own cell wall. Primary cell walls regulate the expansion and the size of growing plant cells [1–3]. When the cell has ceased growing, some plants develop an additional thickened cell wall between the cell membrane and the primary cell wall. This thicker wall is known as the secondary cell wall, and enhances the mechanical strength of the plant. Primary cell walls of all higher plants contain three polysaccharide categories, which are cellulose, hemicellulose, and pectins. Secondary cell walls have a more diverse composition that incorporates lignin, and does not contain pectin. The composition and structure of cell walls vary with species and tissues. For example, primary walls of dicot and non-graminaceous monocot contain a large fraction of xyloglucan [4], which is thought to interact with cellulose to form a three-dimensional load-bearing network [5]. In contrast, the dominant forms of hemicellulose in grass cell walls are arabinoxylan and mixed-linkage glucan [4], which may have different functions and structures than xyloglucan. To obtain a general model of the plant cell wall, a comprehensive study on the structure of dicot, graminaceous monocot, and non-graminaceous monocot is required.

Many chemical and enzymatic extraction studies have been done on the chemical composition and structure of primary plant cell walls [5–9]. Cell wall extraction process employs chemicals to sequentially solubilize pectin, hemicellulose, and cellulose. Pectins are first extracted from primary cell walls by chelating agents [10]. Because of the ease of extraction, pectins are often referred to as an independent network that interpenetrates into the hemicellulose-cellulose network [1,2,11]. After the removal of pectin,

hemicellulose is extracted with a mild alkali solution. The most recalcitrant component in the cell wall is cellulose, which can only be hydrolyzed by a strong acid solution at high temperature. During the extraction process, cellulose associates more with hemicellulose than with pectin [4]. Therefore, cell wall studies have focused on hemicellulose-cellulose interactions. Several possible structures of hemicellulose have been proposed: tethered chains that connect cellulose microfibrils, adsorbed chains that coat regions of the cellulose surface, or intertwined chains embedded in cellulose.

Structural techniques, such as microscopic imaging and x-ray scattering, have tried to characterize wall structure at the molecular level. However, these techniques are not able to differentiate the wall polysaccharides. We recently investigated the molecular structure of the *Arabidopsis* primary cell wall using Small-Angle Neutron Scattering (SANS). The SANS contrast between the wall polysaccharides in native cell walls is minor. To increase the contrast, a fraction of the hydrogen in the matrix polysaccharides was replaced with deuterium. Structural analysis on cellulose and matrix polysaccharides was achieved by contrast matching. The results show that cellulose in *Arabidopsis* has a width of ~3 nm and a length exceeding 100 nm, both are consistent with available literature [13,14]. Some xyloglucan forms uniform layers that coat the surface of cellulose microfibrils. The remaining xyloglucan, as well as other matrix polysaccharides, form coil structures that function as spacers between cellulose microfibrils. Because xyloglucan is not only abundant in *Arabidopsis* but also in the primary cell walls of dicot and non-graminaceous monocot, it is of great interest whether the structure of the *Arabidopsis* cell wall is similar to other cell walls containing xyloglucan. Moreover, it is

also worth investigating whether any polysaccharides replace the structure and function of xyloglucan for cell walls without xyloglucan.

In this study, we determine the primary cell wall architecture of wheat, maize, cucumber, and onion. The cellulose and the matrix polysaccharides are characterized separately. By comparing the structural differences among these cell walls, we discuss the interactions of different cell wall polysaccharides and propose an integrated picture of the primary cell wall.

4.2. Experiment

4.2.1 Plant Material

Primary cell walls of 5-day-old etiolated shoots of wheat and maize, 5-day-old etiolated cucumber hypocotyls, and the whole 5th layer of onion were ground into liquid nitrogen and boiled in 100% ethanol for 5 min and incubated with 100% ethanol overnight. The wall samples were washed 3 times with de-ionized distilled water and sequentially treated with 1.5% and 0.5% sodium dodecyl sulfate to remove wall proteins for 3 hours. The recovered cell walls were consecutively washed with solutions of acetone, methanol:chloroform (1:1 v/v), 100% ethanol, and water. This consecutive washing was performed 3 times. Starch was removed with 500 units of α-amylase from porcine pancreas (Sigma-Aldrich) in 50 mM MES (pH 6.8) for 5 hours at 37°C. First, pectin in the walls was extracted with 50 mM cylcohexanediaminetetraacetic acid (pH 6.8) over 3 consecutive nights at room temperature and further extracted with 50 mM Na_2CO_3 containing 20 mM $NaBH_4$ over 3 consecutive nights at room temperature. The

residual pectin in the walls was further removed by applying 20 units of pectate lyase (Megazyme) in 20 mM Tris-HCL (pH 9.5) with 1 mL $CaCl_2$. The recovered cell walls were washed with water 3 times and dried with a freeze-dryer.

4.2.2. Composition Analysis

Cell walls (~ 3 mg) were incubated in 1 mL of 2 M trifluoroacetic acid (TFA) at 121°C for 1 h. The supernatant was collected and dried under air-flow. The dried 2 M TFA soluble wall polysaccharides were suspended in ddH_2O for High Performance Anion Exchange Chromatography (HPAEC) analysis. The 2 M TFA insoluble residue was incubated in 1 mL of 72% H_2SO_4 at room temperature for 1 h. The slurry of 72% H_2SO_4 was diluted with ddH_2O to 2 M, further hydrolyzed at 100°C for 2 h with frequent vortexing every 15 min, and then neutralized with ammonium hydroxide (NH_4OH). For HPAEC analysis, TFA and H_2SO_4 solubilized samples were filtered with a 0.1 μm centrifuge filter (Amicon). Monosaccharaides were analyzed with a Dionex Carbo PA-20 column with pulsed amperometric detection at a flow rate of 0.5 mL min^{-1} using 0.1 M NaOH under an isocratic condition for 15 min. This was followed by a linear gradient condition for 20 min from 0.1 M NaOH to a mixture of 0.1 M NaOH and 0.1 M sodium acetate (1:1. v/v)

4.2.3. SANS Experiments

In this study, NG3 SANS [15] at National Institute of Standards and Technology (NIST), Gaithersburg, MD and Extended Q-Range SANS [16] at Spallation Neutron Source, Oak Ridge National Laboratory (ORNL), Oak Ridge, TN were utilized to characterize the nanostructure of plant cell walls. Samples were contained in 1mm-thick

quartz cells for SANS measurements. Intensity profiles were obtained by azimuthally averaging the processed 2D intensity data, which were normalized to incident beam monitor counts and corrected with detector dark current, pixel sensitivity, and empty beam scattering. Data were corrected for detector efficiency, background radiation, empty cell scattering, and incoherent scattering to absolute scale. The processing of data was performed using Igor Pro (WaveMetrics) with the NIST analysis macro plugin [17]. To control D_2O concentration, samples were freeze-dried and rehydrated to a contrast-matching condition. Before conducting the SANS measurements, samples were soaked for 12 hours to allow hydroxyl exchange to reach equilibrium [18].

4.2.4 SANS Fitting Model

Our scattering model for cellulose considers three contributions to the total scattering intensity, namely polydisperse cylinders of cellulose microfibrils, power-law scattering for the cellulose network, and incoherent background. The three contributions combine to give the following scattering model,

$$I(Q) = P_{cyl}(Q) + BQ^{-n} + D$$

The scattering intensity of the polydisperse cylinder model is described as

$$P_{cyl}(Q) = \frac{scale}{V_{poly}} \int_0^x f(r) \int_0^{\pi/2} F^2(Q,\alpha) \sin(\alpha) d\alpha$$

$$V_{poly} = \pi r^2 L \left(\frac{z+2}{z+1}\right)$$

where $P_{cyl}(Q)$ is the single cylinder chain form factor, $f(r)$ is the normalized Schulz

distribution of the radius, α is the angle between the cylinder axis and the scattering vector Q, L is the cylinder length, and z is the Schulz polydispersity. The limits of integration are adjusted to cover the full range of the radius. The calculation is normalized to the polydisperse volume using the second moment. The scattering amplitude $F(Q, \alpha)$ is addressed as

$$F(Q,\alpha) = 2V_{cyl}(\rho_{cyl} - \rho_{sol})\frac{sin(QHcos\ \alpha)}{QHcos\ \alpha}\frac{j_1(Qr\ sin\ \alpha)}{Qr\sin\alpha}$$

where $j_1(x)$ is the first order Bessel function, and H is half the cylinder length. The scattering of the cellulose microfibril network at low Q can be described as a fractal object. A fractal object has power-law scattering and is represented as the second term in the first equation. The third contribution comes from incoherent scattering, mainly from hydrogen, and provides no structural information (Q-independent). Therefore, incoherent scattering is incorporated as the constant D.

Our scattering model for hemicellulose considers two contributions to the total scattering intensity, the correlation length for polymer chains and polydisperse core-shell cylinders that coat the cellulose microfibrils. The scattering intensity of the correlation length is described as [19-21]

$$I_{polymer}(Q) = AQ^{-n} + \frac{B}{1 + (Q\xi)^m}$$

The first term describes power-law scattering from a fractal object (exponent=n) and the second term is a Lorentzian function describing polymer chains (exponent=m). ξ is the

correlation length of the polymer chains. This second term characterizes the polymer/solvent interaction and therefore presents the thermodynamics.

The form factor for a polydisperse core-shell cylinder (similar to a polydisperse cylinder) is

$$P_{cscyl}(Q) = \frac{scale}{V_{shell}} \int_0^{\pi/2} F_{cs}^2(Q,\alpha)\, \alpha \sin\alpha \, d\alpha$$

$F_{cs}(Q,\alpha)$ describes scattering from both the cylinder's core and shell with respect to the solvent. Since the cylinder core (cellulose microfibril) is contrast matched in the experiment. $F_{cs}(Q,\alpha)$ can be simplified as

$$F_{cs}(Q,\alpha) = 2(\rho_{shell} - \rho_{solv}) V_{shell} j_0(QHcos\ \alpha) \frac{J_1(Q(r+t)\sin\alpha)}{Q(r+t)\sin\alpha}$$

where t is the thickness of the shell. Eventually, the combined models for hemicellulos and pectin become

$$I(Q) = I_{polymer}(Q) + P_{cscyl}(Q) + D$$

4.3 Results and Discussion

Cell wall composition analysis is accomplished by a sequential treatment of TFA and Saeman. TFA hydrolysis of the cell wall solubilizes monosaccharides from the matrix polysaccharides and a minor fraction of the amorphous cellulose. Saeman hydrolysis releases monosaccharides from crystalline cellulose and any remaining non-cellulose polysaccharides [22]. TFA hydrolysis (Table 4.1) shows that all cell wall

samples contain ~50% of glucose, xylose and mannose, the signature sugars of hemicellulose. Pectin-related sugars, such as galacturonic acid and glucuronic acid, compose about 15% of the cell walls. Compared to the 30–50% of pectin in the general wall composition, the reduced pectin amounts indicate the depectination process has removed most pectin. Since maize and wheat have abundant arabinoxylan and mixed-linkage glucan, the reduction of xyloglucan does not significantly decrease the fraction of glucose and xylose. The Saeman hydrolyzed sugars are composed of ~90% of the glucose and ~10% xylose and mannose, indicating that the TFA solution already hydrolyzed most of the non-cellulose polysaccharides. The trace amount of xylose and mannose may come from two possible sources: mannose could come from the epimerized form of glucose or the very strongly bound hemicellulose that is recalcitrant to TFA (discussed later).

Table 4.1: Monosaccharide Composition Analysis of primary cell walls from maize, cucumber, wheat and onion

Treatment	Monosaccharides (molar %)							
	Glucose	Xylose+ Mannose[a]	Galactose	Fucose	Arabinose	Rhamnose	Galacuronic Acid	Glucuronic Acid
TFA hydrolysis								
Cucumber	18.6 (±0.3)	27.2 (±0.6)	8.7 (±0.1)	4.8 (±0.1)	2.9 (±0.1)	1.0 (±0.3)	9.6 (±0.4)	1.0 (±0.7)
Onion	21.1 (±0.2)	28.0 (±0.3)	7.0 (±0.1)	5.2 (±0.0)	2.0 (±0.1)	1.6 (±0.2)	14.1 (±0.4)	0.7 (±0.4)
Maize	15.5 (±0.3)	27.4 (±0.3)	6.2 (±0.2)	2.9 (±1.2)	7.1 (±0.4)	2.5 (±0.7)	10.7 (±0.2)	4.9 (±1.5)
Wheat	9.7 (±0.1)	28.0 (±0.1)	7.5 (±0.4)	2.3 (±0.1)	15.8 (±1.0)	2.6 (±0.3)	5.7 (±0.3)	1.1 (±0.5)
Saeman hydrolysis								
Cucumber	22.2 (±0.4)	3.9 (±0.1)	ND	ND	ND	ND	ND	ND
Onion	18.8 (±0.4)	1.5 (±0.1)	ND	ND	ND	ND	ND	ND
Maize	20.9 (±0.7)	1.8 (±0.2)	ND	ND	ND	ND	ND	ND
Wheat	24.9 (±1.3)	2.4 (±0.2)	ND	ND	ND	ND	ND	ND

[a] Xylose and Mannose cannot be differentiated

ND- not detected

(± standard deviation, n=3)

Table 4.1 is used to calculate the fraction of each polysaccharide type. The cellulose fraction equals the glucose ratio from Saeman hydrolysis. The hemicellulose fraction is from the summation of glucose, xylose, mannose, and arabinose that are hydrolyzed by TFA. The pectin fraction is the remaining sugars released by TFA hydrolysis. Hemicellulose can further be divided into subclasses of xyloglucan and the non-xyloglucan hemicellulose. Xyloglucan in cell walls of cucumber and onion is calculated on the basis that all TFA-released glucose is from xyloglucan, and estimating the xyloglucan side chain with the ratio of glucose:xylose:galactose:fucose = 100:75:16:8. In the case of wheat and maize, the abundance of mixed-linkage glucan makes it difficult to estimate the amount of xyloglucan just from the monosaccharide table. Therefore, we assign an upper limit to xyloglucan content based on literature (2–5%). The final compositions are summarized in Table 4.2.

Table 4.2: Polysaccharide composition in the primary cell walls of maize, cucumber, wheat, and onion. Units: mole %

Sample name	cellulose	hemicellulose		pectin
		xyloglucan	others	
Cucumber	22.2	37.0[b]	18.3	25.1
Onion	18.8	42.0[b]	14.7	28.6
Maize	20.9	5[a]	45	27.2
Wheat	24.9	5[a]	48.5	19.2

[a] According to the upper limit of xyloglucan in literature.

[b] Calculated on the basis of TFA-released glucose and the fraction rule of xyloglucan sugars (glucose:xylose:galactose:fucose = 100:75:16:8)

Cell wall samples are measured at contrast-match conditions, in which the solvent shares the same scattering length density with at least one object. Contrast variation is used to find the contrast match point. SANS experiments are performed on the wall polysaccharides in solutions of varying D_2O concentration, 0 to 100%. The contrast match point is at the D_2O concentration that minimizes the integrated intensity. The match points have been determined in Chapter 2, where the match points are 35% D_2O for cellulose and 48% D_2O for the matrix polysaccharides. Therefore, the structure of the matrix polysaccharide and cellulose can be separately detected at 35% and 48% D_2O solutions respectively.

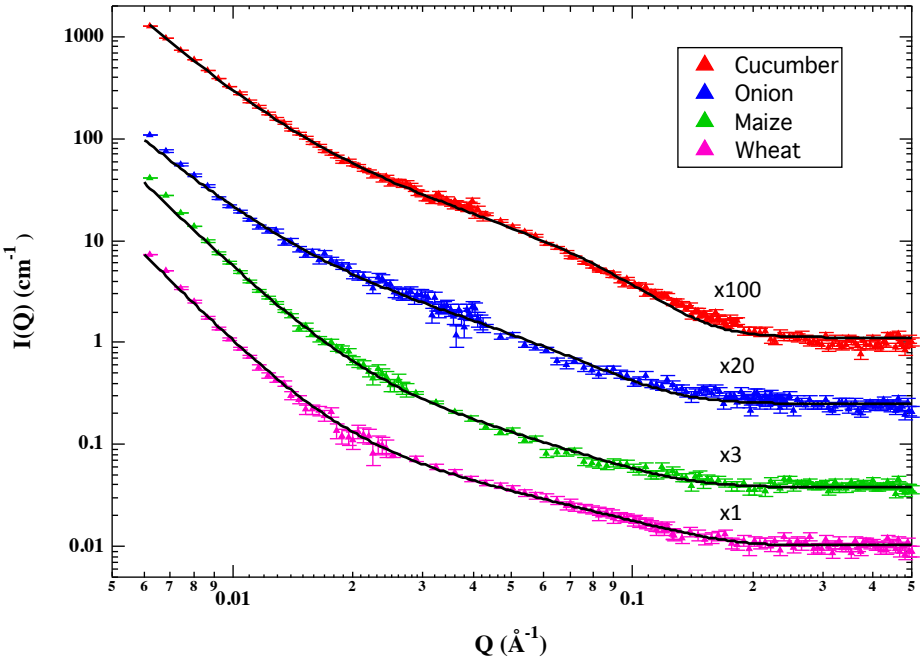

Figure 4.1: Cellulose-highlight measurements for cucumber, onion, maize, and wheat. Intensity profiles are shifted for clarity and the scale factors are shown in the figure. Measurements were performed in 48% D_2O to highlight the cellulose structure. Fitted models are overlaid for each series and parameters are summarized in Table 4.3.

The cell wall samples were soaked in 35% D_2O solutions and measured with

EQSANS (see Figure 4.1). The SANS spectrum contains two structural features. The shoulder at medium to high Q (0.03–0.5Å^{-1}) is modeled by the polydisperse radius cylinder function, describing the size and distribution of individual cellulose microfibrils. The upturn at low-Q (0.006–0.02Å^{-1}) is from power-law scattering, which describes the microfibril network and the heterogeneities, if there are any. All the SANS data are well described by using the same models, suggesting a similar fibrous structure among these primary cell wall samples. Table 4.3 summarizes the fitting parameters of the cellulose structure for cucumber, onion, maize, and wheat.

Table 4.3: Characteristics of cellulose microfibrils in the primary cell walls of cucumber, onion, maize, and wheat. Standard errors are shown in parenthesis.

Plant	Diameter (nm)	Schultz distribution	Fractal	Interfibril distance (nm)
Cucumber	3.2 (0.3)	0.28 (0.07)	2.94 (0.01)	20–33
Onion	3.2 (0.2)	0.37 (0.13)	3.12 (0.03)	20–38
Maize	2.7 (0.3)	0.35 (0.13)	3.74 (0.02)	15–28
Wheat	2.8 (0.4)	0.13 (0.08)	3.78 (0.04)	17–32

An average microfibril diameter of 2.7–3.2 nm is obtained from our SANS data, which is consistent with an elementary cellulose microfibril thickness of 2–3 nm reported in literatures [40]. Considering the close agreement to the size of the elementary cellulose microfibril, it is clear that the contrast matching of the matrix polysaccharides is effective and the intensity profile dominated by the structure of cellulose. It should be noted that none of the cellulose microfibrils probed here is monodisperse, otherwise the scattering profile should exhibit a clear periodic oscillation in Figure 4.1. For other SAXS and

SANS studies on samples of pure cellulose or complete cell walls [24–28], the intensity profiles show a smooth decay, which suggests a size distribution in the cellulose diameter. The size and distribution of cellulose microfibrils from different sources are shown in Figure 4.2, which is obtained from the average diameter and Schultz polydispersity. The size of a microfibril is directly related to the number of chains in a cellulose microfibril. Cellulose has been proposed to contain 18 chains [29], 24 chains [30] and 36 chains [31,32] in its elementary microfibril, and the corresponding diameters are 2.7, 3.1 and 3.8 nm. Our results show that the majority of cellulose microfibrils contain 18–24 chains, and some have 36 chains or more.

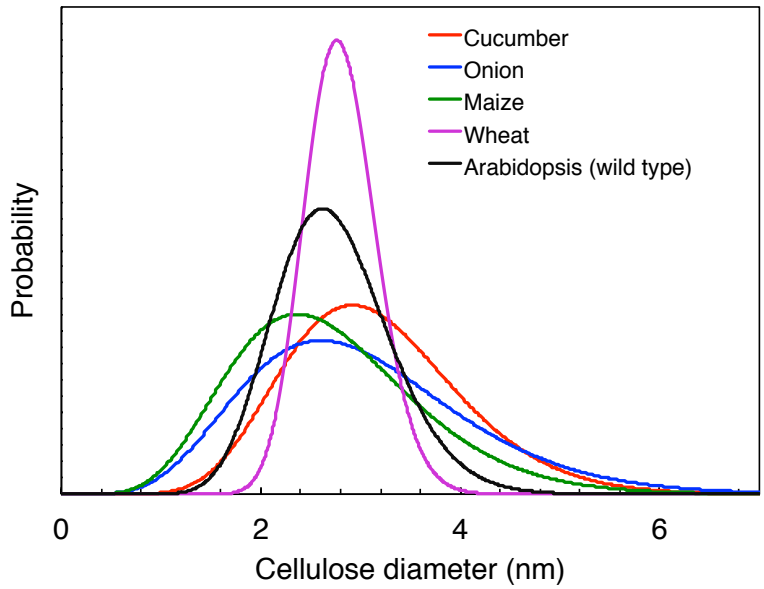

Figure 4.2: Probability distribution of cellulose diameter for primary cell walls of cucumber, onion, maize, wheat, and *Arabidopsis*, obtained from the fitted average diameter and Schultz distribution.

Power-law scattering describes objects larger than the upper length limit of this SANS experiment (~100 nm). The value of the power-law is regarded as a self-similar

structure (mass fractals) and its structure factor [37–39]. Although the cellulose contents are similar among the cell wall samples (see Table 4.2), it does not mean the spatial arrangements of cellulose are the same. If cellulose microfibrils are more aggregated, a larger fractal value and a smaller interfibril spacing would be measured. Interfibril spacing is determined from the gap between the fitting regions of the power-law scattering and the polydisperse radius cylinder scattering, which is essentially the length scale that is larger than a single microfibril but smaller than the microfibril network. As shown in Table 4.3, cellulose in the cell walls of cucumber and onion have smaller fractal dimensions and larger interfibril spacings.

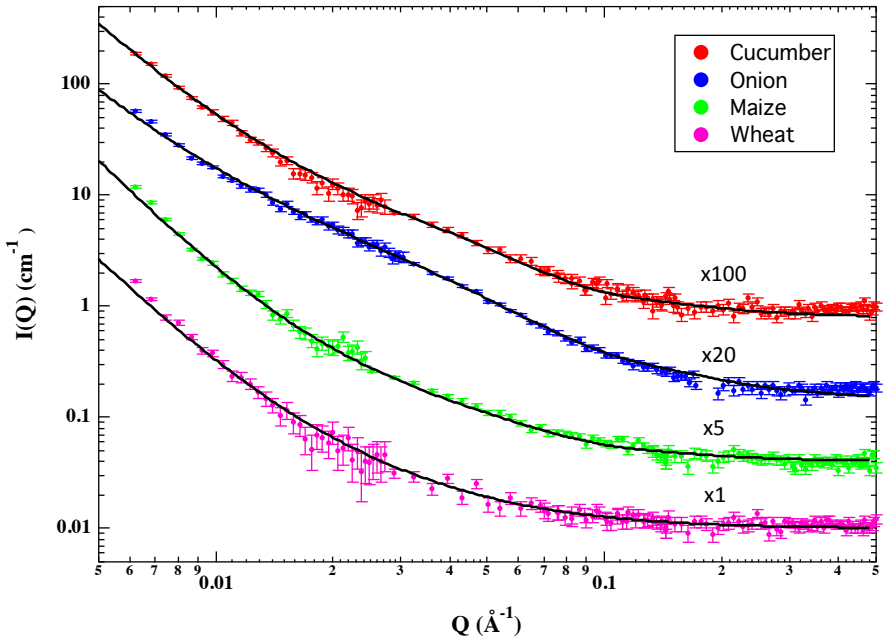

Figure 4.3: Matrix-polysaccharide-highlight measurements for cucumber, onion, maize, and wheat. Intensity profiles are shifted for clarity and the scale factors are shown in the figure. Measurements were performed in 35% (v/v) D_2O solutions to highlight the structure of matrix polysaccharides. Fitt models are overlaid for each series and parameters are summarized in Table 4.4 and Table 4.5.

Table 4.4. Coating features around cellulose microfibrils in primary cell walls of cucumber, onion, maize, and wheat. Standard errors are shown in parentheses.

Plant	Coated ratio (%)	Core diameter (nm)	Shell thickness (nm)	Coated length (nm)
Cucumber	31.4 (6.1)	3.1 (0.2)	1.1 (0.3)	9.1 (2.5)
Onion	53.8 (9.1)	3.2 (0.2)	1.0 (0.2)	17.9 (4.1)
Maize	20.5 (4.9)	3.1 (0.3)	1.1 (0.1)	5.9 (1.2)
Wheat*	4.1 (3.7)	2.9 (0.2)	0.7 (0.3)	3.3 (2.8)

*The scattering of core-shell features in wheat are very weak and almost undetectable

To highlight the structure of the matrix polysaccharides, the cell wall samples are suspended in mixture 35% D_2O solutions in SANS experiments (Figure 3). Note that the contrast variation in Chapter 2 has shown the various matrix polysaccharides all share the same scattering length density and degree of hydrogen/deuterium exchange. Thus, the structure of the matrix polysaccharides would be observed simultaneously at the cellulose-matched condition. The SANS data are fitted by the correlation length model and the core-shell cylinder model. The core-shell cylinder model determines whether matrix polysaccharides form a coated shell on the cellulose surface. This model identifies the thickness, length, and volume fraction of the coated shell. Previous SANS experiments on *Arabidopsis* have illustrated that pectin does not form coating features. Table 4.4 summarizes the coating dimensions found in the primary cell walls. One can see that the coated ratios vary largely between samples, but coating dimensions remain relatively consistent. Similar to what was found in *Arabidopsis*, the diameter of a coated cylinder is ~3 nm and the coating thickness is ~1 nm. The thickness of the coated layer is

similar to the size of a hemicellulose chain, suggesting that the coated layer is composed of a single layer of hemicellulose. Xyloglucan has been regarded as the principle component interacting with cellulose microfibrils. If this is true, intuitively the xyloglucan content should be positively correlated to the coated cellulose ratio. Figure 4.4 plots the coated cellulose percent as a function of xyloglucan to cellulose ratio and shows a positive effect of xyloglucan content on the percent of coated cellulose. It should be noted that although xyloglucan seems to be the principle component interacting with cellulose, it might not be the only component that could firmly bind to the cellulose surface. There is noticeable coating (20.5%) in maize, which is about 5 times more than in wheat. Maize and wheat have very similar composition in terms of the fraction of cellulose, xyloglucan, non-xyloglucan hemicellulose, and pectin (Table 4.1). The major difference is that maize has more mixed-linkage glucan than wheat (based on Sarah Kiemle's compositional analysis). Our results suggest that mixed-linkage glucan could strongly interact with cellulose. NMR studies have shown that glucuronoarabinoxylan in the grass cell wall is very mobile, suggesting a weak interaction with cellulose microfibrils [23]. Chemical extraction-based analysis also indicates mixed-linkage glucan binds to cellulose [41]. The general cellulose binding strength of hemicellulose from high to low should thus be xyloglucan, mixed-linkage glucan, and finally (glucurono)arabinoxylan. But it should be noted that in addition to the types of hemicellulose, the chain length [42], the number of side chains [41], and the side chain sugars [5,43] could all affect the coating content.

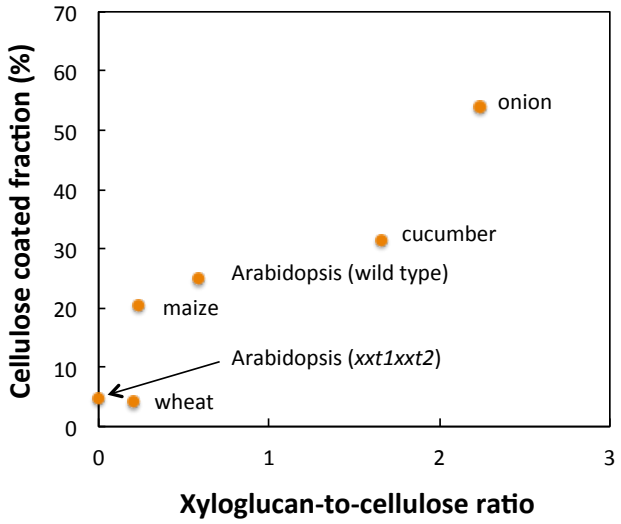

Figure 4.4: Correlation of cellulose coated percent to xyloglucan-to-cellulose ratio

Similar to many water-soluble polymers, a major fraction of the matrix polysaccharides is described by the correlation length model, which has been used for polymer solutions and hydrogels [19,39,44]. The correlational length characteristics are listed in Table 4.5. The matrix polysaccharides in this region follow self-avoiding statistics, similar to the conformation in dilute water solutions [45]. Park et al. have elucidated that this domain of matrix polysaccharides does not contribute to the mechanical strength of cell walls [46]. Instead, we believe the polysaccharide coils could function as a space filler. The correlation length characterizes the average distance between chain entanglements and is equal to the individual coil sizes [44,47]. The correlation length is affected by several factors of the polymer solution, including polymer chain length, polymer concentration, ionic strength, and the pH value of solution. In the primary cell walls, pectins are known to crosslink with each other by forming Ca^{2+} bridges [11], which change with pH and concentration of Ca^{2+}. It is proposed that cell

walls can regulate their stiffness by manipulating the degree of pectin crosslinks [11]. In other words, the correlation length of matrix polysaccharides varies during the growth stage. Given the complexity in the current cases, it is hard to find a single cause accounting for all the differences among these cell walls. The SANS spectra at low Q regions also follows a single power-law scattering, suggesting some large clusters are formed by the matrix polysaccharides [19,20]. The low-Q scattering power-law indicates clusters with self-attraction. Physically, this means that although the monomers in the same chain are self-avoiding, different chains can aggregate. The self-attraction behavior within matrix polysaccharides agrees well with several *in vivo* experiments on xyloglucan, xylan, and pectin [11,13,45,48].

Table 4.5: Correlation length parameters of matrix polysaccharides in primary cell walls of cucumber, onion, maize, and wheat. Standard errors are shown in parentheses.

Plant	Correlation length (nm)	Low-Q scattering power
Cucumber	12.0 (1.3)	3.26 (0.02)
Onion	5.2 (1.3)	3.09 (0.01)
Maize	6.3 (1.5)	3.37 (0.03)
Wheat	7.1 (2.1)	3.31 (0.02)

4.4 Conclusion

In this Chapter, the structure of primary cell walls from dicots and monocots is determined and improves the current understanding of the primary cell wall. Contrast

matching allows us to observe cellulose and matrix polysaccharides. The average diameter of cellulose microfibrils is ~3 nm, consistent with the microscopic images in literature. Cellulose microfibril's diameter is not monodesperse, with a diameter range of 2–6 nm, which means that different microfibrils could have varying numbers of chains. The primary walls are microfibril-based composites. Fractal dimensions are determined to characterize the cellulose network and the association of microfibrils. Fractal dimensions are smaller in cucumber and onion, suggesting that cellulose disperses more when xyloglucan is present. The matrix polysaccharides are able to form two different structures: one domain involves self-avoided coils that fill the interfibril space and another domain coats cellulose microfibrils. For dicots, the hemicellulose coating feature is more significant, confirming that xyloglucan is the principle component in primary cell walls. Similar coating features are observed in maize, which lacks xyloglucan but has more mixed-linkage glucan, suggesting that mixed-linkage glucan also interacts strongly with cellulose microfibrils.

4.5 Reference

1. Albersheim, P., Darvill, A., Roberts, K., Sederoff, R. & Staehelin, A. Plant cell walls: from chemistry to biology. (Garland Science, Taylor and Francis Group, LLC, 2010).
2. Cosgrove, D. J. Growth of the plant cell wall. Nat. Rev. Mol. Cell Biol. 6, 850–61 (2005).
3. Nishiyama, Y. Structure and properties of the cellulose microfibril. J. Wood Sci. 55, 241–249 (2009).
4. Kafle, K. et al. Cellulose microfibril orientation in onion (Allium cepa L.) epidermis studied by atomic force microscopy (AFM) and vibrational sum frequency

generation (SFG) spectroscopy. Cellulose 21, 1075–1086 (2013).

5. Niimura, H., Yokoyama, T., Kimura, S., Matsumoto, Y. & Kuga, S. AFM observation of ultrathin microfibrils in fruit tissues. Cellulose 17, 13–18 (2009).

6. Ding, S.-Y. & Himmel, M. E. The maize primary cell wall microfibril: a new model derived from direct visualization. J. Agric. Food Chem. 54, 597–606 (2006).

7. Zhang, T., Mahgsoudy-Louyeh, S., Tittmann, B. & Cosgrove, D. J. Visualization of the nanoscale pattern of recently-deposited cellulose microfibrils and matrix materials in never-dried primary walls of the onion epidermis. Cellulose 21, 853–862 (2013).

8. McCann, M. C., Wells, B. & Roberts, K. Direct visualization of cross-links in the primary plant cell wall. J. Cell Sci. 96, 323–334 (1990).

9. McCann, M. C., Wells, B. & Roberts, K. Complexity in the spatial localization and length distribution of plant cell-wall matrix polysaccharides. J. Microsc. 166, 123–136 (1992).

10. Scheller, H. V. & Ulvskov, P. Hemicelluloses. Annu. Rev. Plant Biol. 61, 263–89 (2010).

11. Hayashi, T. Xyloglucan in the primary cell wall. Annu. Rev. Plant Physio. Plant Mol. Biol. 40, 139–168 (1989).

12. Park, Y. B. & Cosgrove, D. J. Changes in cell wall biomechanical properties in the xyloglucan-deficient xxt1/xxt2 mutant of Arabidopsis. Plant Physiol. 158, 465–75 (2012).

13. Cavalier, D. M. et al. Disrupting two Arabidopsis thaliana xylosyltransferase genes results in plants deficient in xyloglucan, a major primary cell wall component. Plant Cell 20, 1519–37 (2008).

14. Pauly, M., Albersheim, P., Darvill, A. & York, W. S. Molecular domains of the cellulose/xyloglucan network in the cell walls of higher plants. Plant J. 20, 629–639 (1999).

15. Lerouxel, O., Choo, T. S., Se, M., Lerouge, P. & Pauly, M. Rapid structural phenotyping of plant cell wall mutants by enzymatic oligosaccharide fingerprinting. Plant Physiol. 130, 1754–1763 (2002).

16. Carpita, N. C. Hemicellulosic polymers of cell walls of zea coleoptiles. Plant

Physiol. 72, 515–21 (1983).

17. Park, Y. B. & Cosgrove, D. J. A revised architecture of primary cell walls based on biomechanical changes induced by substrate-specific endoglucanases. Plant Physiol. 158, 1933–43 (2012).

18. Thompson, J. E. & Fry, S. C. Restructuring of wall-bound xyloglucan by transglycosylation in living plant cells. Plant J. 26, 23–34 (2001).

19. Carpita, N. C. & Gibeaut, D. M. Structural models of primary cell walls in flowering plants: consistency of molecular structure with the physical properties of the walls during growth. Plant J. 3, 1–30 (1993).

20. McCann, M. C. & Roberts, K. Changes in cell wall architecture during cell elongation. J. Exp. Bot. 45, 1683–1691 (1994).

21. Gu, J. & Catchmark, J. M. The impact of cellulose structure on binding interactions with hemicellulose and pectin. Cellulose 20, 1613–1627 (2013).

22. Dick-Pérez, M. et al. Structure and interactions of plant cell-wall polysaccharides by two- and three-dimensional magic-angle-spinning solid-state NMR. Biochemistry 50, 989–1000 (2011).

23. Bootten, T. J., Harris, P. J., Melton, L. D. & Newman, R. H. Solid-state 13C-NMR spectroscopy shows that the xyloglucans in the primary cell walls of mung bean (Vigna radiata L.) occur in different domains: a new model for xyloglucan-cellulose interactions in the cell wall. J. Exp. Bot. 55, 571–83 (2004).

24. Thompson, D. S. How do cell walls regulate plant growth? J. Exp. Bot. 56, 2275–85 (2005).

25. Talbott, L. D. & Ray, P. M. Molecular size and separability features of pea cell wall polysaccharides : implications for models of primary wall structure. Plant Physiol. 98, 357–68 (1992).

26. Zhao, Z., Crespi, V. H., Kubicki, J. D., Cosgrove, D. J. & Zhong, L. Molecular dynamics simulation study of xyloglucan adsorption on cellulose surfaces: effects of surface hydrophobicity and side-chain variation. Cellulose 21, 1025–1039 (2014).

27. Nishiyama, Y. et al. Periodic disorder along ramie cellulose microfibrils. Biomacromolecules 4, 1013–7 (2003).

28. Matthews, J. F. et al. Computer simulation studies of microcrystalline cellulose Ibeta. Carbohydr. Res. 341, 138–52 (2006).

29. Pai, S. S. et al. The conformation of the poly(ethylene glycol) chain in mono-PEGylated lysozyme and mono-PEGylated human growth hormone. Bioconjug. Chem. 22, 2317–23 (2011).

30. Heller, W. T. Small-angle neutron scattering and contrast variation: a powerful combination for studying biological structures. Acta Crystallogr. D. Biol. Crystallogr. 66, 1213–7 (2010).

31. Endo, H. et al. Membrane decoration by amphiphilic block copolymers in bicontinuous microemulsions. Phys. Rev. Lett. 85, 102–5 (2000).

32. Glinka, C. J., Barker, J. G., Hammouda, B. & Krueger, S. The 30m small-angle neutron scattering instruments at the National Institute of Standards and Technology. J. Appl. Crystallogr. 31, 430–445 (1998).

33. Lynn, G. W. et al. Bio-SANS—A dedicated facility for neutron structural biology at Oak Ridge National Laboratory. Phys. B Condens. Matter 385-386, 880–882 (2006).

34. Kline, S. R. Reduction and analysis of SANS and USANS data using IGOR Pro. J. Appl. Crystallogr. 39, 895–900 (2006).

35. Hishikawa, Y., Togawa, E., Kataoka, Y. & Kondo, T. Characterization of amorphous domains in cellulosic materials using a FTIR deuteration monitoring analysis. Polymer. 40, 7117–7124 (1999).

36. Hammouda, B., Ho, D. L. & Kline, S. Insight into clustering in poly(ethylene oxide) solutions. Macromolecules 37, 6932–6937 (2004).

37. Hammouda, B., Ho, D. & Kline, S. SANS from Poly(ethylene oxide)/Water Systems. Macromolecules 35, 8578–8585 (2002).

38. Hammouda, B. SANS from polymers—review of the recent literature. Polym. Rev. 50, 14–39 (2010).

39. Gendreau, E. et al. Cellular basis of hypocotyl growth in Arabidopsis thaliana. Plant Physiol. 114, 295–305 (1997).

40. Thompson, J. E. & Fry, S. C. Evidence for covalent linkage between xyloglucan and acidic pectins in suspension-cultured rose cells. Planta 211, 275–86 (2000).

41. Popper, Z. A. & Fry, S. C. Xyloglucan-pectin linkages are formed intra-protoplasmically, contribute to wall-assembly, and remain stable in the cell wall. Planta 227, 781–94 (2008).

42. Kennedy, C. J. et al. Microfibril diameter in celery collenchyma cellulose: X-ray scattering and NMR evidence. Cellulose 14, 235–246 (2007).

43. Park, Y. B. et al. Effects of plant cell wall matrix polysaccharides on bacterial cellulose structure studied with vibrational sum frequency generation spectroscopy and x ray Diffraction. Biomacromolecules 15, 2718–2724 (2014).

44. Teixeira, J. Small-angle scattering by fractal systems. J. Appl. Crystallogr. 21, 781–785 (1988).

45. Dick-Perez, M., Wang, T., Salazar, A., Zabotina, O. A. & Hong, M. Multidimensional solid-state NMR studies of the structure and dynamics of pectic polysaccharides in uniformly 13C-labeled Arabidopsis primary cell walls. Magn. Reson. Chem. 50, 539–50 (2012).

46. Zykwinska, A. W., Ralet, M. J. & Garnier, C. D. Evidence for in vitro binding of pectin side chains to cellulose. Plant Physiol. 139, 397–407 (2005).

47. Zhao, Z. et al. Cellulose microfibril twist, mechanics, and implication for cellulose biosynthesis. J. Phys. Chem. A 117, 2580–2589 (2013).

48. Hyland, L. L., Taraban, M. B., Hammouda, B. & Yu, Y. B. Mutually reinforced multicomponent polysaccharide networks. Biopolymers 95, 840–51 (2011).

49. Hammouda, B. & Ho, D. L. Insight into chain dimensions in PEO/water solutions. J. Polym. Sci. 45, 2196–2200 (2007).

50. Manet, S. & Jean, B. SANS measurements of semiflexible xyloglucan polysaccharide chains in water reveal their self-avoiding statistics Biomacromolecules 12, 3330–3336 (2011).

51. Hule, R. A., Nagarkar, R. P., Hammouda, B., Schneider, J. P. & Pochan, D. J. Dependence of self-assembled peptide hydrogel network structure on local fibril nanostructure. Macromolecules 42, 7137–7145 (2009).

52. Linder, Å., Bergman, R., Bodin, A. & Gatenholm, P. Mechanism of assembly of xylan onto cellulose surfaces. Langmuir 5072–5077 (2003).

53. Ding, S.-Y., Zhao, S. & Zeng, Y. Size, shape, and arrangement of native cellulose fibrils in maize

Chapter 5 The Confined Dynamics of Surface Water of Cellulose Microfibril

This chapter is adapted from the author's manuscript: Shih-Chun Huang, Lin Fang, Kokonand Sinha, Tanuj Motawani, Christopher Lee, Seong H. Kim, Jeffery Catchmark, and Janna K. Maranas.

Water-cellulose interactions have been extensively studied, but none of these model systems may capture the behavior of water in the highly organized surface. Because of the experimental difficulty of selectively probing the dynamics of water on cellulose surface, radically different views about the properties of cellulose-bound water have proliferated. To resolve the long-standing controversy, we perform quasi-elastic neutron scattering experiments to study the dynamics of hydrogenated water adsorbed on deuterated cellulose. Two water hydration layers are identified. For water content of 11% and 25% At 278–338K, the inner hydration water displays a residence time around 100 ps, which is extremely slow compared with a few ps in bulk water). The outer hydration water shows a residence time around 10 ps. Despite the difference in the translational motion, both inner and outer hydration water shares similar rotational relaxation diffusivity.

5.1 Introduction

Water in plant cell walls is essential for proteins to maintain their function. Water can compose up to 90% of wall mass in a rapid growing plant tissue [1,2]. When water is removed, the growth and the expansion of a plant cell are ceased. Water also controls the diffusion rate of substrates, the conformation of wall polymers and the mechanical strengths of wall. Despite the importance of water for cell wall, there is a tendency to assume water inside cell wall shares the same properties as bulk water. This assumption is incorrect as it oversimplifies the complexity of cell wall. Plant cell walls consist of multiple biological polymers such as cellulose, hemicellulose, pectin and lignin. It is clear that these polymers could interact with water and form geometric confinement to limit the diffusion of water molecules [3–5].

In this article, we focus on the water interaction to cellulose, the most important constituent of cell wall. Cellulose is not only essential for all plants on earth, but also an important economic resource for paper, fabrics, food and biofuel. Chemically, Cellulose is a linear polymer assembled by unbranched β-1,4-linked glycopyranose units [6]. In plants, cellulose is synthesized membrane and crystallized into microfibrils by enzyme complexes in plasma [7,8]. Native cellulose contains a combination of two crystalline allomorphs, Iα and Iβ and a fraction of amorphous regions [9–11]. The dimension of microfibrils in land plant tissues can vary within 2–8 nm in diameter and a few hundreds nm in length, varying with plant source and growth stage. One of the key features of the cellulose is its water insolubility. When cellulose is hydrated, water interacts with cellulose and influences the cellulose crystal structure and the cellulose mechanical

strength. Moreover, water layers stack above cellulose surface as it is in contact with solid surface such as clay minerals and glasses [12]. Evidences in favor of more than a single phase of surface water of cellulose are reported. Based on dielectric spectroscopy measurements on a cellulose hydrogel, 90% of water molecules shows a reduced mobility indicating a close association with cellulose microfibrils, and only 10% of water moves freely as bulk water [13]. The observation is consistent with later differential scanning calorimetric studies, in which freezable and nonfreezable water contents are measured [3,14]. Three populations of water molecules are categorized when associated with cellulose: First, the adsorbed water molecules are directly bound to cellulose and form nonfreezable water. Then beyond ~25% water content threshold, the additional adsorbed water molecules become freezable with crystallization point below 0°C. And only at very high water content, bulk-like water appears and can be crystallized at 0°C. Similarly, three water categories have been observed by nuclear magnetic resonance on cellulose suspension and each category has different mobility and crystallization temperature that depend on how much they are associated with cellulose microfibrils [15,16].

Observations obtained by several independent methods led us to conclude multiple types of surface water of cellulose, and some of that might involve with a low rate of mobility. Thus we plan a more direct dynamics investigation on the water by conducting quasi-elastic neutron scattering (QENS) on deuterium-labeled cellulose samples. QENS is a powerful technique for studying the mobility of water and has been applied on various organic and inorganic water-containing materials, including proteins, polymers, metals and minerals. To characterize motions of water, QENS provides an

excellent probe scale in both time and space. More importantly, QENS is most sensitive to the motions of hydrogen. As hydrogen scatters ~40 times greater than all other elements, scattering from water can be highlighted if selective deuteration is achieved.

The ideal sample for this QENS study should consist of deuterated cellulose (d-cellulose) and hydrogenated water. It is challenging to prepare cellulose in deuterium form from plant tissues. The traditional method extracting cellulose from cell wall does not work well in this scenario. The kinetic isotope effects of deuterium cause lower chemical reactivity and slow the plant metabolism at higher D_2O concentration. When plants are grown in H_2O/D_2O mixture, abnormal morphology and delayed developments are found with increasing D_2O concentration. Alternatively, we prepare the d-cellulose by using the cellulose producing bacteria as known as Gluconacetobacter xylinus [17–21]. This method has been extensively used to construct cellulose network mimicking the fiber network in plant cell wall. Unlike traditional extraction method on plant tissues, this approach allows samples to contain little inherent biological wall polymers such as lignin and pectin. More importantly, Gluconacetobacter xylinus could overcome the kinetic isotope effect and survive in high concentration D_2O. Careful preparation using this method could yield high deuterium incorporation with minimal effects on the cellulose morphology [21].

In this article, the high deuterium incorporation of cellulose is confirmed by sum-frequency generation (SFG) optical spectroscopy. Furthermore, the crystal structure and the morphology of the d-cellulose are compared with protonated cellulose (h-cellulose) using x-ray diffraction (XRD) and field-emission scanning electron microscopy

(FESEM). Finally, we measure the dynamics of d-cellulose with 11% and 25% hydration level at temperature 278–338K using QENS. Different motions including the vibration, the rotation and the translation of water are characterized respectively and the result reveals significantly different dynamics of water molecules confined in cellulose microfibrils.

5.2 Materials and Methods

5.2.1 Materials.

Gluconacetobacter strain Gluconacetobacter xylinus ATCC 700178 was cultured in a standard Hestrin-Schramm medium to obtain cellulose microfibrils. Hestrin-Schramm medium contains 2% (w/v) glucose, 0.5% (w/v) peptone, 0.5% (w/v) yeast extract, 0.27% (w/v) disodium phosphate and 1.15 g/L citric acid [22]. Cells for the inoculum were cultured on a rotary shaker with addition of 1% cellulase enzyme for 3 days at 28 °C. Cells were harvested by centrifugation, then resuspended in the culture medium. The suspension is used as an inoculum. The main cultures were grown 1 week for h-cellulose and 4 weeks for d-cellulose. At the end of incubation, the pellicles were collected, and treated with 0.1M sodium hydroxide solution followed by rinsing until pH 7. The purified cellulose was lyophilized. To accurately control the water content, the samples were freeze-dried under vacuum and then rehydrated to 11% and 25% water content.

5.2.2 SFG Measurements.

The SFG setup used was described in previous studies [23]. The 532 nm laser pulse was generated by frequency doubling of the 1064 nm output from a Nd:YAG laser. An optical parameter generator/amplifier (OPG/OPA) using β-BaB2O4 and AgGaS2 crystals was

pumped with 532 and 1064 nm laser pulses and generated tunable IR pulses in the wavelength range of 2.3–10 μm with < 6 cm^{-1} bandwidth. The incidence angles of visible and IR pulses with respect to surface normal were 60° and 56°, respectively. The incident visible and IR beams were s-polarized and p-polarized, respectively, with respect to the laser incidence plane. The SFG signal was collected in the reflection geometry with no polarization selection. A beam collimator was used to enhance the collection efficiency of the SFG signals. SFG spectra were taken at 4 cm^{-1}/step for the 1000–1500 and 2700–3050 cm^{-1} regions, and 8 cm^{-1}/step in the 3096–3800 cm^{-1} region, with averaging 100 shots/step. Spectral data were fitted with the Lorentzian function to find the peak center position.

5.2.3 X-ray diffraction Measurements

XRD diagrams were recorded using PANalyticalX'Pert Pro multipurpose diffractometer with Cu Kα radiation generated at 45 kV and 40 mA. The data was collected in the 2θ range 5–40°. The degree of crystallinity index was calculated by PeakFit software following Park et al [24]. The broad peak at around 21.5° was assigned to the amorphous contribution. Crystallinity is calculated from the ratio of the area of all crystalline peaks to the total area. The dimension of the crystal perpendicular to the diffracting planes with Miller indices and B_{hkl} was evaluated by using Scherrer's expression

$$B_{hkl} = \frac{K\lambda}{\sqrt{\Delta 2\theta^2 - \Delta 2\theta_{inst}^2 cos\theta}}$$

B_{hkl} is the average crystalline width of a specific phase; K is a constant that varies with the

method of taking the breadth (K = 0.9); λ is the wavelength of incident X-rays (λ = 0.154nm); θ is the center angle of the peak; $\Delta 2\theta$ is the full width at half maximum of the reflection peak and $\Delta 2\theta_{inst}$ is the instrumental broadening, which was determined from reflections of the silicon standard NIST Si 640.

5.2.4 Field Emission Scanning Electron Microscopy

FESEM was employed to observe cellulose morphology and microstructure. Samples were lyophilized and sputter coated with gold. A LEO-1530 field emission scanning electron microscope (LEO Elektronenmikroskope, Oberkochen, Germany) was operated at 5kV.

5.2.5 QENS Measurements.

We employ both the time-of-flight disk chopper spectrometer (DCS) at National Institute of Standards and Technology for time scale 2–50 ps, and the backscattering spectrometer (BSS) at Oak Ridge National Lab for time scale 50–800 ps. For the DCS, we operate at an incident wavelength of 4.8 Å, corresponding to an energy resolution of 56μeV. This instrument setting at DCS accesses time scale 2–50 ps and spatial scale 3–11Å. For the BSS, we apply a dynamic range of 100μeV (energy resolution of 3.4μeV), corresponding to times scale 50–800 ps. The geometry allows us to access a spatial scale of 3–15Å.

Both instruments require an annular geometry for the sample. We prepare the sample as a uniformly thin film between aluminum foils. Water-containing cellulose sample is placed in a thin annular aluminum sample holder. The thickness is chosen to permit ~10% of the neutrons scatters from the sample; this gives good signal intensity with low probability of multiple scattering. Samples are measured at steady temperatures

at 278, and 298, 318 and 338K. To ensure samples are measured at steady state, data are collected after an hour of thermal equilibrium at every setting temperature.

All sample data are compared with the resolution function obtained by measuring vanadium standard. The intensity of scattered neutrons is a function of momentum transfer (Q) and frequency (ω). We reduce the raw scattering data using DAVE (Data Acquisition and Visualization Environment), in which raw data is corrected with resolution, background and detector efficiency to obtain reduced profile, $I(Q, \omega)$.

5.2.6 QENS Data Treatments.

The scattering intensity is proportional to the dynamic structure factor, $S(Q,\omega)$.

$$I = N\frac{\sigma_{inc}}{4\pi}\frac{k_s}{k_i}S(Q,\omega)$$

Where N is the number of nuclei, σ_{inc} is the incoherent scattering cross section of a nucleus, k_i and k_s are the incident and scattered neutron wave vectors, and $Q=|k_s-k_i|$ is the momentum transfer. Neutron intensities in the energy domain, including the resolution function are inverse-Fourier transformed to the self-intermediate scattering function, S(Q,t) [25,26]. S(Q,t) is an autocorrelation function in atom position. The decay of S(Q,t) is thus an indication of the mobility of water molecules.

5.3 Result and Discussion

5.3.1 Morphology, Crystallinity and Deuteration Level of Deuterated Cellulose

Previous reports have shown an apparent effect of D_2O concentration on plants growth. Higher plants fail to survive in D_2O solutions with concentration more than 80%. Even at 50% D_2O concentration, plants are always carried out with abnormal development,

delayed germination, slower growth, and sometimes completely inhibited growth. These influences might originate from the higher viscosity, the lower ionization constant and the lower substance solubility of D_2O. Gluconacetobacter xylinus could adapt to D_2O better than higher plants, but lower biological activity is still inevitable. In this case, when pure D_2O and deuterated glucose feed are used to prepare d-cellulose, the production rate is 4 times slower. The critical advantage in this method is the 100% D_2O tolerance of Gluconacetobacter xylinus. This allows us to prepare cellulose with maximal deuterium incorporation. As shown in Figure 1, the deuterium incorporation of d-cellulose is characterized by SFG. SFG is only sensitive to the cellulose functional groups in this system [23,27–30]. Other components such as adsorbed water, air moisture or protein residuals are excluded. The observed signal of h-cellulose in Figure 1 is typical to SFG data reported for bacterial cellulose [27]. The band at 3200–3400 cm^{-1} is attributed to the OH vibration, and the band at 2800–3000 cm^{-1} corresponds to the CH vibration. Both OH and CH peaks are prominent in h-cellulose but indiscernible in d-cellulose. Instead, peaks at 2400–2600 and 2050–2250 cm^{-1} emerge in d-cellulose represent the stretching vibration of OD and CD. OD and CD vibrate at lower frequencies due to the heavier reduced mass of deuterium bonds. We estimate deuterium incorporation based on the integrated peaks of CD and OD to CH and OH, which yields high deuterium incorporation in the d-cellulose. Further, we calculate the Iα and Iβ ratio in both d-cellulose and h-cellulose as described in Park et al [27]. The values of I_α and I_β in two bacterial cellulose samples are reasonably close. The similar proportions clearly indicate that even after high deuteration, no significant impact is observed on the crystalline phase

of bacterial cellulose.

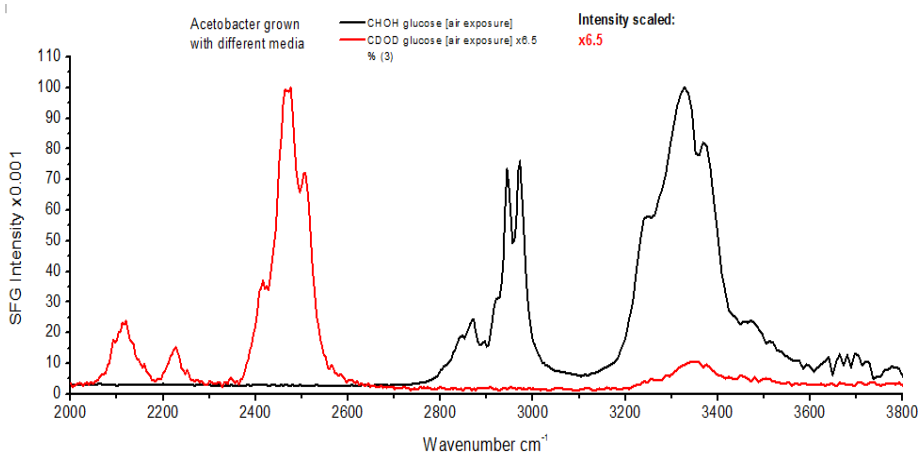

Figure 5.1: SFG comparison of d-cellulose and h-cellulose

To further illustrate this point, the microstructures in h-cellulose and d-cellulose samples are measured with XRD as shown in Figure 2. Three main peaks at 14.5°, 16.5° and 22.7° correspond to crystallographic planes (100), (010) and (110) respectively. The I_α and I_β of cellulose have been studied on various cellulose samples using x-ray and neutron diffraction [10,11,31]. Any changes in the d-spacing would indicate a difference in I_α and I_β fraction. In the case here, both samples show primary I_α characteristics allomorph, consistent with the SFG result and previous reports on bacterial cellulose [18,32]. The other purpose of investigating the diffraction is to compare their crystallinity. The integrated intensity of diffraction peak is calculated over the background to obtain crystallinity index [24], which yield 73.2 and 72.1 respectively for h-cellulose and d-cellulose. As summarized in Table I, the similar d-spacing and crystallinity indicate that deuteration does not disrupt the microstructure of cellulose microfibrils.

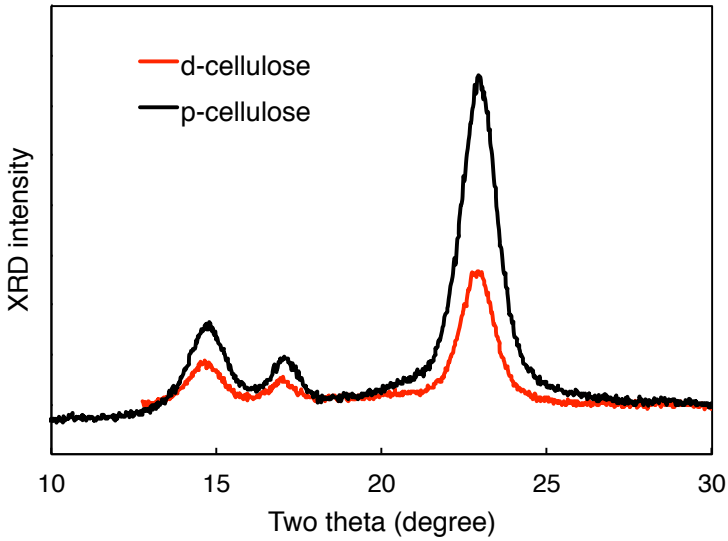

Figure 5.2: XRD of h-cellulose and d-cellulose

Table 5.1: Comparison of h-cellulose and d- cellulose crystal structure

	crystallinity	d-spacing (Å)			crystal size (nm)		
		(100)	(010)	(110)	(100)	(010)	(110)
h-cellulose	73.2%	6.0	5.2	3.9	5.3	7.4	6.4
d-cellulose	72.1%	6.0	5.2	3.9	7.3	8.9	6.9

The fibril morphology of d-cellulose is shown in Figure 3. It clears show that the bacterial cellulose successfully mimics the fiber network morphology in plant cell wall. Although the production rate is considerably slower, the d-cellulose sample shares the same morphology as other bacterial cellulose sample [33]. Cellulose made from bacteria source has been described as randomly oriented and overlaid microfibril ribbons. The FESEM image indicates that the d-cellulose microfibrils still remain smooth surface and uniform size with no significant difference in overall morphology.

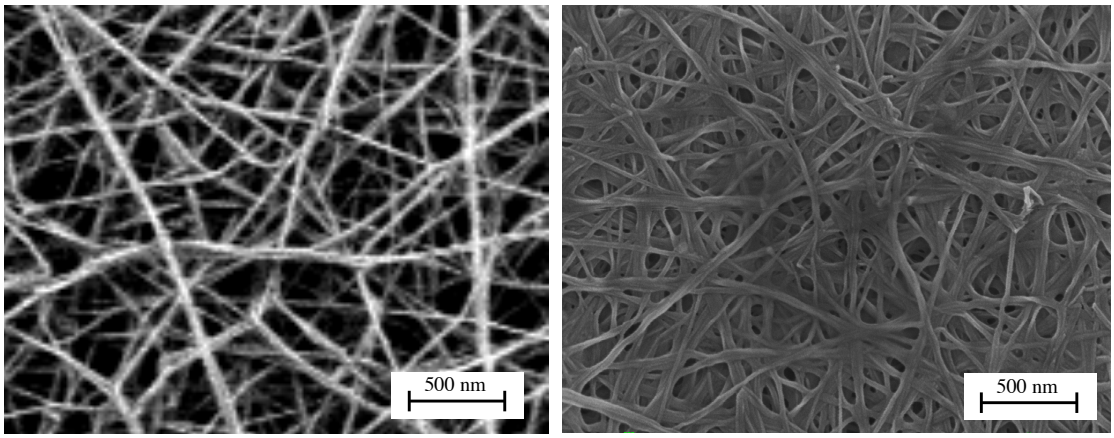

Figure 5.3: Comparison of FESEM direct images of h-cellulose and d-cellulose

5.3.2 Water Dynamics

The d-cellulose samples are freeze-dried and rehydrated before QENS measurements to accurately control the hydration level. Previous differential scanning calorimeter reports have illustrated that cellulose could strongly associate with the sorbed water and make it unfreezable up to 25% water content [3]. Samples at 11% (11W) and 25% (25W) water content are prepared to investigate the dynamics of the surface water of cellulose. QENS provides dynamics information in a specific space-time window by measuring the energy transfer (E) and the scatter vector (Q) of scattered neutrons. In a QENS measurement, the length scale of atomic motions is around Q^{-1}, and the time scale of motions is $t \leq \Delta E^{-1}$, where ΔE is the spectrometer resolution. There are several QENS facilities in US and each of them corresponds to a unique probe range in time and space. To cover an extended time range analysis, we include results from DCS and BSS to access a probe length scale around nanometer and time scale of picosecond to nanosecond.

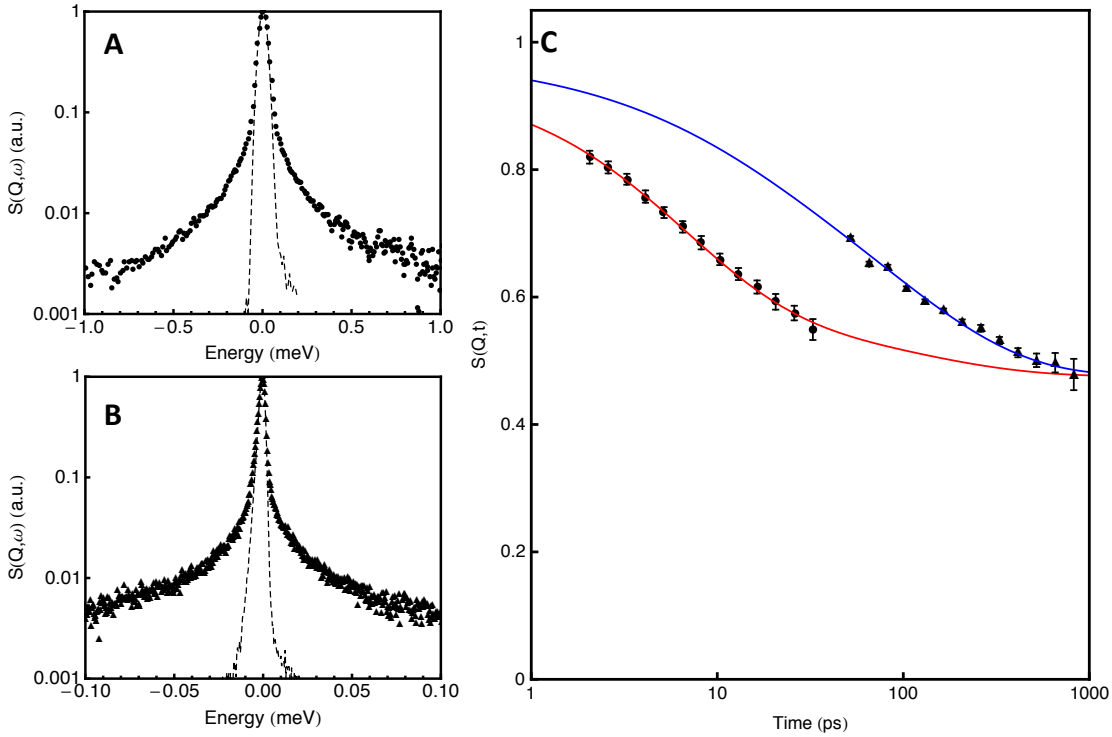

Figure 5.4: (A) *S(Q,ω)* of 25% hydrated d-cellulose sample at 298K measured at DCS at *Q*=1.2 Å^{-1} (B) *S(Q,ω)* of 20% hydrated d-cellulose sample at 298K measured at BSS at *Q*=1.2 Å^{-1} (C) Fourier-transformed self-intermediate scattering function *S(Q,t)* of DCS and BSS spectra and the corresponding fit lines for 25% hydrated d-cellulose sample at 298K at *Q*=1.2 Å^{-1}.

The DCS and BSS data collected at *Q*=1.2 Å^{-1} are shown in Figure 4A and 4B as an example. The broad quasielastic signal contains dynamics information of the system. The width of the signal grows with the temperature. Besides the quasielastic signal, the spectra include an elastic line due to the immobile components such as the surface hydroxyl groups and possibly some extremely slow water molecules not being captured in the time scale of this instrument. We employ Fourier transformation (see *QENS data treatment*) to convert energy domain data to time domain self-immediate scattering

function *S(Q,t)* as shown in Figure 4C. The decays of *S(Q,t)* from unity represents diffusion of scattering particles. To characterize the dynamics of cellulose surface water, we use the fitting equation

$$S(Q,t) = \varepsilon + (1-\varepsilon)S_V S_R S_T$$

Where ε is the elastic incoherent structure factor, describing the fraction of scattering intensity that is outside the time scale of the experiment, and S_V, S_R, S_T respectively describe the motions of vibration, rotation and translation. *S(Q,t)* data from DCS and BSS are fitted separately. Since the two instruments have different probe range in time, ε is allowed to vary between the two instruments. The first dynamics term S_V is used to describe the hydrogen in a water molecule vibrating perpendicular to its own OH bond. The vibration of water molecules is a very fast process. At time intervals greater than 1 ps, S_V is expressed as Debye-Waller factor, which equals to $\exp(-Q^2a^2/3)$, where a is the root-mean-square vibrational amplitude [34–36]. The a value is usually not affected much by the confinement. Previous QENS studies have found that a for water is from 0.4 to 0.6 Å either in bulk or in confinement. In our case, the a values are 0.48–0.51Å in DSC and 0.43–0.48Å in BSS, which agree well with the literature values [36,37].

Another fast process found in this system is the rotation of water. We use the Sears approximation to describe this motion, which is essentially a hindered hydrogen motion over a spherical surface. In the Q range of this experiment (0.4–2Å^{-1}), the first three orders dominates the Sears approximation, and the self-intermediate scattering function for rotation is therefore addressed as

$$S_R = j_0^2(Qr) + j_1^2(Qr)\exp\left(-\frac{t}{3\tau_R}\right) + j_2^2(Qr)\exp\left(-\frac{t}{\tau_R}\right)$$

Where j_i is the ith order spherical Bessel function, and r is the length of rotation radius known as 0.92 Å for water OH bond, and τ_R is the rotational relaxation time, which can be well characterized in the DCS time probe range. In our results, τ_R is independent of Q and its Q-averaged values at every temperature and water content are shown in Figure 5. It is obvious that the rotational relaxation time increases as the temperature decreases. The rotational diffusion takes place on a picosecond time scale, and slows down by a factor of 3 compared to bulk water at room temperature. This is comparable with water confined by macromolecule or protein, where τ_R is 2–5 times greater than that of bulk water [36]. The large τ_R values confirm that the water observed here is confined by cellulose. The influence of the confinement on the rotational dynamics of water is usually limited because rotational diffusion motions are localized and correlated with a typical hydrogen bond lifetime. From Figure 5 one can see τ_R appear to obey an Arrhenius-type temperature dependence. The activation energies are (2.10±0.06) and (2.22±0.14) kJ/mol for 11W and 25W samples. Similar to water confined in minerals and clays [35,38,39], the activation energy of the rotation is substantially lower than value of 7.74 kJ/mol for bulk water [37].

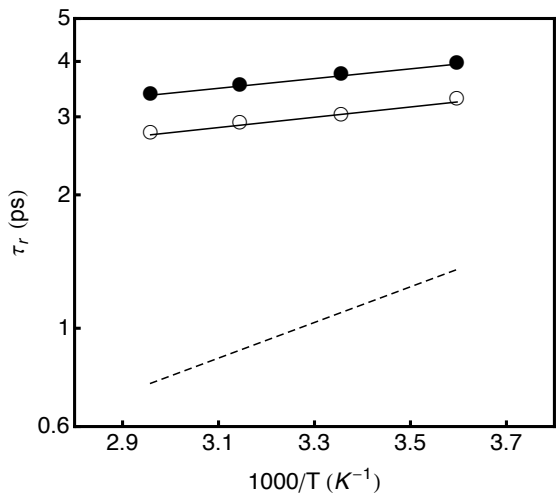

Figure 5.5: Temperature dependence of the rotational relaxation time of 11W(solid circle), 25W(circle) and bulk water (dashed line)

When the translational diffusion takes place in a single mode, it can be described by a single stretched exponential function. In the present work, given the broad probe time range provided by the two instruments, we observe two distinct translational motions that their characteristic relaxation times differ by an order of magnitude. Thus the fitting equation below includes two stretched exponential decay functions: the first exponential term describes the faster water molecules not in direct contact with cellulose, and the second term describes the slower water molecules in direct contact with cellulose.

$$S_T = (1 - X(Q))exp\left(-\left(\frac{t}{\tau_1}\right)^{\beta_1}\right) + X(Q)exp\left(-\left(\frac{t}{\tau_2}\right)^{\beta_2}\right)$$

where X(Q) is a spectrum weighing factor for the contribution of the very slow water detected by the QENS experiment, τ is the translational relaxation time, and β is the stretched factor used to describe the heterogeneity of the translational motion. X(Q) in a sense represent the fraction of the very slow water. At the lowest Q of this experiment,

X(Q) is 0.64 in 11W and 0.27 in 25W samples. One can then calculate that in both samples, the slowest water is ~7% cellulose mass. This fraction of water is presumably directly associated with cellulose microfibril. According to recent molecular dynamics simulation, the first hydration water could strength the cellulose rigidity by bridging neighboring cellulose monomers [40]. Similar conclusion is also obtained from XRD analysis, completely removing the first hydration water induces cellulose deformation and decrease in crystal size [32]. The cellulose-water interaction not only influences cellulose structure but also water properties. For water in either hydration layer, τ increases and β decreases significantly. β is between 0.5 and 0.85 for the two translational motions, indicating a distribution of the relaxation times. The average relaxation time, τav, can be calculated from τ and β as expressed by the equation below

$$\tau_{av} = \int_0^\infty dt\ exp\left(-\left(\frac{t}{\tau}\right)^\beta\right)$$

Figure 6 shows the Q dependence of the inverse relaxation time, τ_{av}^{-1}. This plot is important in determining the nature of jump diffusion process. For molecules restricted in a local area (ex: water in porous glass, or functional groups of rigid polymer), τ_{av}^{-1} reaches to a non-zero constant at small Q. In the present case, we see τ^{-1} approaches to zero at very low Q. This result confirms the majority of quasi-elastic scattering comes from surface water of cellulose rather than the cellulose functional groups or water entrapped in cellulose microfibril. Also, in this plot one can see that the mobility of the inner and the outer hydration layer are considerably different. There is about an order of magnitude difference in τ_{av} at any Q and at every probed temperature.

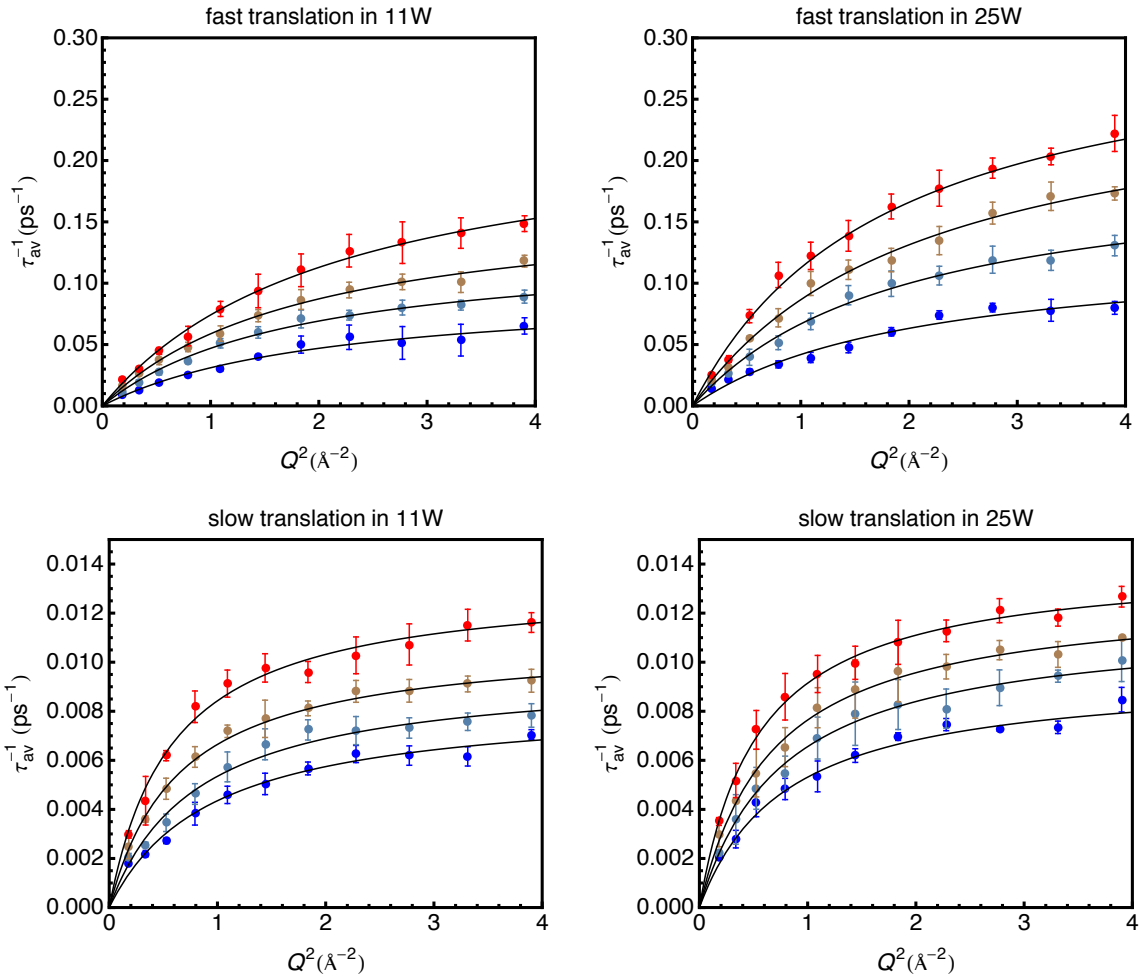

Figure 5.6: The Q dependence of the translational relaxation time in 11W and 25W samples. It is readily seen that the Q^2 dependence of translational relaxation time obeys jump diffusion model at 278–338K. T=278K(blue); T=298K(green); T=318K(orange); T=338K(red).

The translational motion of water molecules can be expressed by the three-dimensional jump diffusion model, in which a molecule executes oscillatory motions about one position for a mean residence time τ_{res}, then diffuse to another nearby position

in a repetitive way. If each diffuse step is a fixed value, a maximum at intermediate Q would display in Figure 6 [38].

The absence of such a maximum indicates that either in the inner or the outer hydration layer, water molecules undergo jump diffusion with a distributed length L. It is of interest to investigate τ_{av}^{-1} as a function of Q^2. Fitting the Q dependence of inverse τ_{av} with the equation below would yield τ_{res}, diffusion coefficient D and the jump diffusion process.

$$\frac{1}{\tau_{av}} = \frac{DQ^2}{1 + DQ^2\tau_{res}}$$

The fitting parameters are summarized in Table II. Figure 7 shows that the τ_{res} of the inner and outer hydration layers are about one and two orders of magnitude greater than that of bulk water at room temperature. In a classic picture of bulk water, a water molecule has to break at least three bonds to undergo translation. The temperature dependence of τ_{res} for bulk water is non-Arrhenius. The confined water displays a distinct temperature dependence than bulk water. Water in the inner and outer hydration layer obeys Arrhenius-type temperature dependence, $\tau_{res}=(\tau_0)\exp(E_A/RT)$, suggesting it is restricted by one principle bond (presumably the bond between cellulose and water) rather than multiple water-to-water hydrogen bonds. The activation energies E_A of the inner and outer hydration do not change with water content. For inner hydration water, it is (5.77±0.66) kJ/mol for 11W and (4.99±0.52) kJ/mol for 25W. For outer hydration water, it is (11.53±0.70) kJ/mol for 11W and (11.84±1.25) kJ/mol for 25W. All of the values are typical for physically adsorbed water species and much lower than chemically adsorbed species.

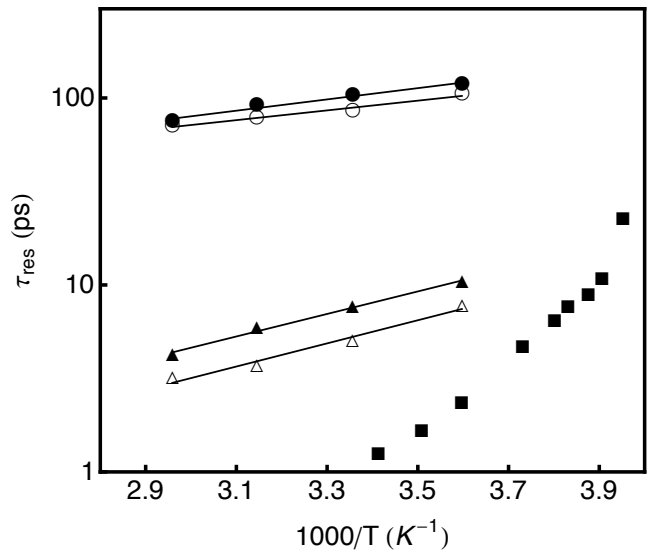

Figure 5.7: The temperature dependence of the characteristic times for the two translational motions of surface water on cellulose surface compared with bulk water. The translational residence times obey an Arrhenius-type temperature dependence. Slow translation in 11W (solid circle); Slow translation in 25W (empty circle); Fast translation in 11W (solid triangle); Fast translation in 25W (empty triangle); Bulk water after Teixeira et al (solid square).

Table 5.2: The temperature and water content dependence of translational relaxation time, jump length and diffusion coefficient. The jump length is calculated by $L=(6D\tau_{res})^{1/2}$

Sample	Temperature (K)	Fast Translation			Slow Translation		
		τ_{Res1}(ps)	L_1(Å)	D_1 (100×Å^2/ps)	τ_{Res2}(ps)	L_2(Å)	D_2 (100×Å^2/ps)
11W	278	10.44	1.71	4.6	118.53	2.52	0.9
	298	7.61	1.82	7.3	103.56	2.74	1.2
	318	5.91	1.78	9.0	91.55	3.10	1.7
	338	4.23	1.66	10.8	75.18	3.19	2.3
25W	278	7.76	1.70	6.2	104.80	2.63	1.2
	298	5.06	1.75	10.1	85.76	2.77	1.5
	318	3.68	1.67	12.7	78.17	3.00	1.9
	338	3.17	1.80	17.5	70.86	3.34	2.6
Bulk*	293	1.25	1.29	22.2			

The inner and outer hydration layers show distinct jump length. For the outer hydration layer, the jump length is independent to temperature or hydration level, being

around 1.7Å under all conditions and close to the jump length in bulk water [37]. In contrast to the small jump length in the outer hydration layer, jump length in inner hydration layer is two to three times greater than that in bulk water and increases with temperature. In any scenario, such a large jump length is hard to reconcile with the bulk-like molecular density. This result is in a good agreement with molecular dynamics simulation on the surface water of cellulose I_β, which indicates water form several high density layers above cellulose microfibrils [12]. Noted that the jump length in the inner hydration layer does not simply correlates with the distance between two neighboring cellulose monomers (5–7Å) [10]. Instead, it is between the jump length of outer hydration layer (~1.7Å) and the distance between monomers on cellulose crystal surface, suggesting water in the inner layer can either travel to outer hydration layer or stay in the same layer by jumping to the neighboring cellulose surface hydroxyl groups. As temperature increases, water in the inner hydration layer then has higher chance to overcome the energy barrier and directly jump to neighboring cellulose hydroxyl groups and thus the average jump length increases with temperature.

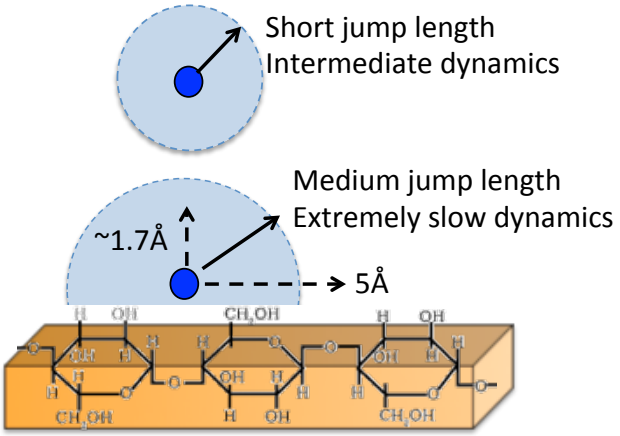

Figure 5.8: Schematic of water molecule dynamics in close contact with cellulose

microfibril

5.4 Conclusion

In conclusion, by using QENS, we have successfully characterized the surface water of cellulose. When cellulose is hydrated with 11% and 25% water, two water layers forms above cellulose microfibrils. Despite both layers share similar rotational motion that is about 3 times slower than bulk water, their translational motions differ significantly. The inner hydration layer, because of constructing strong hydrogen bond with cellulose, has extremely slow translational motion that is slower than bulk water for almost 2 orders of magnitude. The water content that can be strongly bound is ~7% of cellulose mass, presumably is related to the number of effective cellulose surface hydroxyl groups. This value can be varied for cellulose with different diameter or with different crystalline allomorph. The dynamics of outer hydration is less affected by cellulose surface, but still about 5 times slower than bulk water. It is expected that if more water is added to the present system, eventually some of water would not be affected by cellulose at all and exhibit bulk-like behavior.

5.5 Reference

1. Albersheim, P., Darvill, A., Roberts, K., Sederoff, R. & Staehelin, A. Plant cell walls: from chemistry to biology. (Garland Science, Taylor and Francis Group, LLC, 2010).
2. Cosgrove, D. J. Growth of the plant cell wall. Nat. Rev. Mol. Cell Biol. 6, 850–61 (2005).
3. Nishiyama, Y. Structure and properties of the cellulose microfibril. J. Wood Sci. 55, 241–249 (2009).

4. Kafle, K. et al. Cellulose microfibril orientation in onion (Allium cepa L.) epidermis studied by atomic force microscopy (AFM) and vibrational sum frequency generation (SFG) spectroscopy. Cellulose 21, 1075–1086 (2013).
5. Niimura, H., Yokoyama, T., Kimura, S., Matsumoto, Y. & Kuga, S. AFM observation of ultrathin microfibrils in fruit tissues. Cellulose 17, 13–18 (2009).
6. Ding, S.-Y. & Himmel, M. E. The maize primary cell wall microfibril: a new model derived from direct visualization. J. Agric. Food Chem. 54, 597–606 (2006).
7. Zhang, T., Mahgsoudy-Louyeh, S., Tittmann, B. & Cosgrove, D. J. Visualization of the nanoscale pattern of recently-deposited cellulose microfibrils and matrix materials in never-dried primary walls of the onion epidermis. Cellulose 21, 853–862 (2013).
8. McCann, M. C., Wells, B. & Roberts, K. Direct visualization of cross-links in the primary plant cell wall. J. Cell Sci. 96, 323–334 (1990).
9. McCann, M. C., Wells, B. & Roberts, K. Complexity in the spatial localization and length distribution of plant cell-wall matrix polysaccharides. J. Microsc. 166, 123–136 (1992).
10. Scheller, H. V. & Ulvskov, P. Hemicelluloses. Annu. Rev. Plant Biol. 61, 263–89 (2010).
11. Hayashi, T. Xyloglucan in the primary cell wall. Annu. Rev. Plant Physio. Plant Mol. Biol. 40, 139–168 (1989).
12. Park, Y. B. & Cosgrove, D. J. Changes in cell wall biomechanical properties in the xyloglucan-deficient xxt1/xxt2 mutant of Arabidopsis. Plant Physiol. 158, 465–75 (2012).
13. Cavalier, D. M. et al. Disrupting two Arabidopsis thaliana xylosyltransferase genes results in plants deficient in xyloglucan, a major primary cell wall component. Plant Cell 20, 1519–37 (2008).
14. Pauly, M., Albersheim, P., Darvill, A. & York, W. S. Molecular domains of the cellulose/xyloglucan network in the cell walls of higher plants. Plant J. 20, 629–639 (1999).

15. Lerouxel, O., Choo, T. S., Se, M., Lerouge, P. & Pauly, M. Rapid structural phenotyping of plant cell wall mutants by enzymatic oligosaccharide fingerprinting Plant Physiol. 130, 1754–1763 (2002).
16. Carpita, N. C. Hemicellulosic polymers of cell walls of zea coleoptiles. Plant Physiol. 72, 515–21 (1983).
17. Park, Y. B. & Cosgrove, D. J. A revised architecture of primary cell walls based on biomechanical changes induced by substrate-specific endoglucanases. Plant Physiol. 158, 1933–43 (2012).
18. Thompson, J. E. & Fry, S. C. Restructuring of wall-bound xyloglucan by transglycosylation in living plant cells. Plant J. 26, 23–34 (2001).
19. Carpita, N. C. & Gibeaut, D. M. Structural models of primary cell walls in flowering plants: consistency of molecular structure with the physical properties of the walls during growth. Plant J. 3, 1–30 (1993).
20. McCann, M. C. & Roberts, K. Changes in cell wall architecture during cell elongation. J. Exp. Bot. 45, 1683–1691 (1994).
21. Gu, J. & Catchmark, J. M. The impact of cellulose structure on binding interactions with hemicellulose and pectin. Cellulose 20, 1613–1627 (2013).
22. Dick-Pérez, M. et al. Structure and interactions of plant cell-wall polysaccharides by two- and three-dimensional magic-angle-spinning solid-state NMR. Biochemistry 50, 989–1000 (2011).
23. Bootten, T. J., Harris, P. J., Melton, L. D. & Newman, R. H. Solid-state 13C-NMR spectroscopy shows that the xyloglucans in the primary cell walls of mung bean (Vigna radiata L.) occur in different domains: a new model for xyloglucan-cellulose interactions in the cell wall. J. Exp. Bot. 55, 571–83 (2004).
24. Thompson, D. S. How do cell walls regulate plant growth? J. Exp. Bot. 56, 2275–85 (2005).
25. Talbott, L. D. & Ray, P. M. Molecular size and separability features of pea cell wall polysaccharides : implications for models of primary wall structure. Plant Physiol. 98, 357–68 (1992).
26. Zhao, Z., Crespi, V. H., Kubicki, J. D., Cosgrove, D. J. & Zhong, L. Molecular

dynamics simulation study of xyloglucan adsorption on cellulose surfaces: effects of surface hydrophobicity and side-chain variation. Cellulose 21, 1025–1039 (2014).

27. Nishiyama, Y. et al. Periodic disorder along ramie cellulose microfibrils. Biomacromolecules 4, 1013–7 (2003).
28. Matthews, J. F. et al. Computer simulation studies of microcrystalline cellulose Ibeta. Carbohydr. Res. 341, 138–52 (2006).
29. Pai, S. S. et al. The conformation of the poly(ethylene glycol) chain in mono-PEGylated lysozyme and mono-PEGylated human growth hormone. Bioconjug. Chem. 22, 2317–23 (2011).
30. Heller, W. T. Small-angle neutron scattering and contrast variation: a powerful combination for studying biological structures. Acta Crystallogr. D. Biol. Crystallogr. 66, 1213–7 (2010).
31. Endo, H. et al. Membrane decoration by amphiphilic block copolymers in bicontinuous microemulsions. Phys. Rev. Lett. 85, 102–5 (2000).
32. Glinka, C. J., Barker, J. G., Hammouda, B. & Krueger, S. The 30m small-angle neutron scattering instruments at the National Institute of Standards and Technology. J. Appl. Crystallogr. 31, 430–445 (1998).
33. Lynn, G. W. et al. Bio-SANS—A dedicated facility for neutron structural biology at Oak Ridge National Laboratory. Phys. B Condens. Matter 385-386, 880–882 (2006).
34. Kline, S. R. Reduction and analysis of SANS and USANS data using IGOR Pro. J. Appl. Crystallogr. 39, 895–900 (2006).
35. Hishikawa, Y., Togawa, E., Kataoka, Y. & Kondo, T. Characterization of amorphous domains in cellulosic materials using a FTIR deuteration monitoring analysis. Polymer. 40, 7117–7124 (1999).
36. Hammouda, B., Ho, D. L. & Kline, S. Insight into clustering in poly(ethylene oxide) solutions. Macromolecules 37, 6932–6937 (2004).
37. Hammouda, B., Ho, D. & Kline, S. SANS from Poly(ethylene oxide)/Water Systems. Macromolecules 35, 8578–8585 (2002).

38. Hammouda, B. SANS from polymers—review of the recent literature. Polym. Rev. 50, 14–39 (2010).
39. Gendreau, E. et al. Cellular basis of hypocotyl growth in Arabidopsis thaliana. Plant Physiol. 114, 295–305 (1997).
40. Thompson, J. E. & Fry, S. C. Evidence for covalent linkage between xyloglucan and acidic pectins in suspension-cultured rose cells. Planta 211, 275–86 (2000).
41. Popper, Z. A. & Fry, S. C. Xyloglucan-pectin linkages are formed intra-protoplasmically, contribute to wall-assembly, and remain stable in the cell wall. Planta 227, 781–94 (2008).
42. Kennedy, C. J. et al. Microfibril diameter in celery collenchyma cellulose: X-ray scattering and NMR evidence. Cellulose 14, 235–246 (2007).
43. Park, Y. B. et al. Effects of plant cell wall matrix polysaccharides on bacterial cellulose structure studied with vibrational sum frequency generation spectroscopy and x-ray diffraction. Biomacromolecules 15, 2718–2724 (2014).
44. Teixeira, J. Small-angle scattering by fractal systems. J. Appl. Crystallogr. 21, 781–785 (1988).
45. Dick-Perez, M., Wang, T., Salazar, A., Zabotina, O. A. & Hong, M. Multidimensional solid-state NMR studies of the structure and dynamics of pectic polysaccharides in uniformly 13C-labeled Arabidopsis primary cell walls. Magn. Reson. Chem. 50, 539–50 (2012).
46. Zykwinska, A. W., Ralet, M. J. & Garnier, C. D. Evidence for in vitro binding of pectin side chains to cellulose. Plant Physiol. 139, 397–407 (2005).
47. Zhao, Z. et al. Cellulose microfibril twist, mechanics, and implication for cellulose biosynthesis. J. Phys. Chem. A 117, 2580–2589 (2013).
48. Hyland, L. L., Taraban, M. B., Hammouda, B. & Yu, Y. B. Mutually reinforced multicomponent polysaccharide networks. Biopolymers 95, 840–51 (2011).
49. Hammouda, B. & Ho, D. L. Insight into chain dimensions in PEO/water solutions. J. Polym. Sci. 45, 2196–2200 (2007).
50. Manet, S. & Jean, B. SANS measurements of semiflexible xyloglucan polysaccharide chains in water reveal their self-avoiding statistics

Biomacromolecules 12, 3330–3336 (2011).

51. Hule, R. A., Nagarkar, R. P., Hammouda, B., Schneider, J. P. & Pochan, D. J. Dependence of self-assembled peptide hydrogel network structure on local fibril nanostructure. Macromolecules 42, 7137–7145 (2009).

52. Linder, Å., Bergman, R., Bodin, A. & Gatenholm, P. Mechanism of assembly of xylan onto cellulose surfaces. Langmuir 5072–5077 (2003).

53. Ding, S.-Y., Zhao, S. & Zeng, Y. Size, shape, and arrangement of native cellulose fibrils in maize

Chapter 6 Concluding Remarks and Suggestions for Future Directions

In Chapter 1 we have summarized the complexity of plant primary cell walls in composition, structure and dynamics. The principle objective of this research is to answer three main questions: (1) What are the structural role and function of xyloglucan in primary cell wall? (2) Do other wall polysaccharides compensate or play the role of xyloglucan when xyloglucan level is low? (3) Does water share the same properties as bulk water when interacting with polysaccharides? To investigate these questions, we characterize a wide range of plant primary cell walls and bacterial cellulose model system. We then correlate the structural properties to wall compositions, types of polysaccharides whereas the water dynamics properties to surface chemistry of polysaccharides.

6.1 Xyloglucan and pectins in *Arabidopsis* primary cell walls

We study four *Arabidopsis* primary cell walls: The first one is wild-type wall that is abundant of xyloglucan, pectins and cellulose, and second one is *xxt1*/*xxt2* wall that lacks xyloglucan but still have the rest, and the third and fourth walls are the depectinated version of the former two cell walls. We employ SANS with contrast matching to determine the structures of cellulose microfibrils and the matrix polysaccharides. The contrast between wall components arises from the differences of hydrogen/deuterium exchange in D_2O. The average diameter of single microfibril is 2.7, which not affected by

the presence of either xyloglucan or pectins. Macroscopically, many cellulose microfibrils aggregate together to form load-bearing network, with interfibril spacing filled by the matrix polysaccharides. The majority of the matrix polysaccharides functions as interfibril fillers, rather than taut chains that directly bear mechanical load. The comparison of fractal indicates that xyloglucan is a more rigid spacer than pectins. Moreover, our results have characterized that in *Arabidopsis* only xyloglucan could firmly coat on cellulose microfibrils. We do not observe coating feature before depectination process. In contract to the current notion envisioning cellulose surface is mostly coated, the analysis estimates only 25% of cellulose surface is covered. Despite a relative small fraction in the coating domain, it could mediate contacts between microfibrils, functions as biomechanical "hot-spots" in primary walls as proposed by Park et al. *xxt1*/*xxt2* lacks xyloglucan biosynthesis, resulting in lower hemicellulose content and a more important role for non-xyloglucan hemicelluloses and for pectins. The most important difference is the reduction of coating feature, which results in weaker mechanic properties of *xxt1*/*xxt2* primary wall.

6.2 Impact of different hemicellulose on primary cell wall structure

We have expanded the range of available data describing the influence of matrix polysaccharides on the assembly of plant primary cell walls. This study focuses on whether the difference between hemicelluloses changes the structure of cell wall entity. For this purpose, we investigate the difference between dicot, graminaceuos monocot (grass) and non-graminaceuos monocot and consider the impact of three hemicellulose

components, namely xyloglucan, arabinoxylan and mixed-linked glucans. The cellulose microfibril structure is not affected much by the composition and type of hemicellulose. The cellulose diameter distributes from 2 to 6 nm in these primary walls, consistent with reported size in literatures. One can calculate the number of chains inside one single microfibril from the cellulose diameter, and obtain the number of 18, 24, 36 or even more cellulose chains. At larger scale, microfibrils form network in primary walls. From the analysis of mass fractal, we find that cellulose microfibrils associate together more in plants when less xyloglucan is present. Similar to what is found in the cell wall of *Arabidopsis*, partial microfibril is coated and the coat fraction increases with xyloglucan content. A decent coating feature is observed in maize, which lacks of xyloglucan but has mix-linked glucan, suggesting that mixed-linked glucan adopt some characteristics of xyloglucan in monocots. With that, we conclude that the affinity to cellulose from strong to weak is xyloglucan, mixed-linkage glucan, and arabinoxylan. The better association between xyloglucan/mixed-linkage glucan and cellulose might be in favor of their same backbone.

6.3 Confined dynamics of water when confined by cellulose microfibril

We determine the dynamics of cellulose surface water at controlled temperature 278, 298, 318 and 338K and at water content 11% and 25% using quasi-elastic neutron scattering. Two distinct layers, inner and outer hydration layer, of cellulose surface water are identified. The inner hydration layer is the first 7% of water in direct contact with cellulose surface and the additional water afterward becomes the outer hydration layer.

From the time probe window 2–800 ps, the vibrational, rotational and translational motions are characterized. Except for the vibrational motion, both layers do not exhibit similar dynamics to bulk water. The rotational motion in inner and outer hydration layer is both about 3 times slower than bulk water. Water in the inner hydration layer experiences stronger hydrogen bond and confinement with cellulose. The translational motion is ~2 orders slower than bulk water. The dynamics of outer hydration is less affected by cellulose, but is still about 5 times slower than bulk water. It is expected that if one keep adding more water to the present system, gradually some of water would exhibit bulk-like behavior.

6.4 Suggestion for future direction of this work and preliminary results

6.4.1 Gel formation of pectin in cell wall

Despite many years of research, the roles, conformations, and distributions of the pectin are still not fully understood. Pectins are necessary in plants to cohesive cells and retain water in cell walls. Up to date there is no successful mutant plant could normally grow when that lack the ability to synthesize. Depending on the pectin, coordinate bonding with Ca^{2+} ions or hydrogen bonding and hydrophobic interaction are involved in gel formation, which enhance the mechanical strength of cell walls and are believed to regulate plant growth by controlling cell wall expansion.

It is possible that pectin functions as responsive hydrogels in cell walls react to pH value, which fluctuates from 4 to 8 for plant *in vivo*. pH-responsive gels can be detected using SANS, where the distance between crosslinks is characterized. For

instance, poly(acrylic acid) (PAA) aggregates at pH below 5 and swells at pH greater than 5. Under acidic environment, the dissociation of pectin carboxyl groups is "masked" by excessive H^+ and therefore pectin loses its charge. When pH increases carboxyl groups are "unmasked" to return negatively charged carboxylate ions, generating crosslinking sites for Ca^{2+} ions. Similar to pH, fluctuations in Ca^{2+} concentration may also be a trigger for structural changes. High Ca^{2+} concentration should produce more crosslinks and vice versa. Rheology experiments on pure pectin under different pH and Ca^{2+} have shown that pectin exhibits a solution to gel transition around pH=6 and pectin starts loosen when Ca^{2+} concentration is lower than 20mM. This supports our idea that pectin changes conformation as conditions change. The pH-responsive property of pectins, if can be verified, is very unique in cell wall. We have tested xyloglucan solution from pH 2–7 and did not see any structural changes (see Figure 6.1). Therefore, it is of great scientific interest to see if pectin network changes under different physiological conditions in cell wall. The microstructure of pectin will enhance the understanding of the mechanism behind observed plant growth behavior.

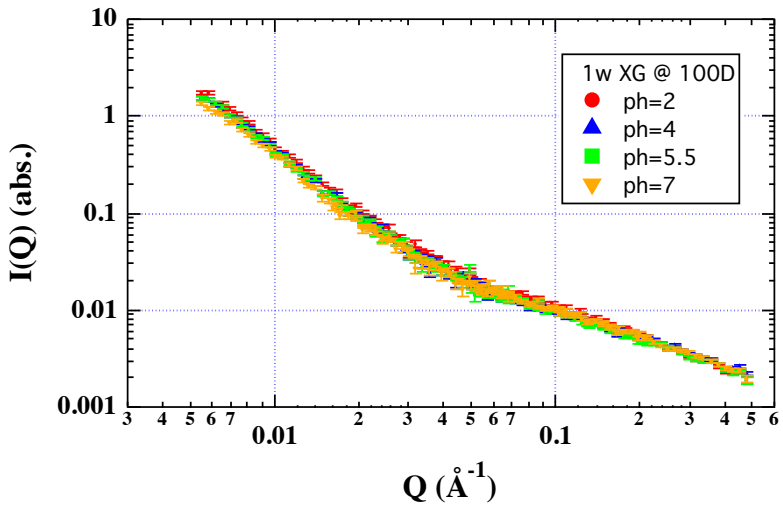

Figure 6.1: SANS measurement on 1wt% xyloglucan D_2O solution at pH 2–7. Structure does not change responsive to pH of environment.

6.4.2 Assembly of secondary cell wall

This thesis so far has put an emphasis on primary cell walls. Some plants develop thickened secondary cell walls to enhance mechanical strength. Secondary cell walls are more diverse in composition that generally contains more cellulose, more hemicellulose, less pectin or no pectin, and deposition of lignin. The structure of secondary cell wall is not less complicated than primary cell wall. We have discussed how neutron scattering technique can be useful in determining primary cell wall structure. Similarly, it is of interest to exploit the advantage on determining secondary cell wall structure. Noted that secondary cell walls are usually developed with deposit of significant amount of hydrophobic lignin. To utilize the contrast match method, it is necessary to determine whether the contrast match point of lignin is close to either cellulose (35% D_2O) or hemicellulose and pectins (48% D_2O). Based on the preliminary contrast variation test done by Dan Ye, the contrast match point of lignin is 43–45 % D_2O, within a close range

of the match point of matrix polysaccharides, i.e., the SANS method applied to primary cell wall is useful on secondary cell walls. Since cellulose tend to bundle together to form macrofibrils in secondary cell wall, low-Q data will be helpful to obtain a full picture of the assembly of cell wall.

6.4.3 Cellulose in secondary cell wall produced by inactivation of cellulose synthease proteins

The unique crystalline properties of cellulose can be traced back to the plant's mechanism of cellulose synthesis. *Arabidopsis* has been used as a model to shown that secondary cell wall cellulose microfibrils are synthesized by an 18 subunit plasma membrane super-complex, composed three different cellulose synthase isoforms (CesAs 4, 7, 8) in a 1:1:1 stoichiometry. To gain insight on the organization and catalytic activity of each CesA subunit and the effect of cellulose microfibril perturbation, Dr. Tien's group has developed individual loss-of-function mutants in the *Arabidopsis* CesAs. These mutations involve catalytic inactivation while maintaining CesA structural integrity, resulting in cellulose synthesis complexes with only 2/3 of the subunits able to synthesize cellulose. These mutant lines can gain insight into several aspects of the cellulose microfibril and the plant cell wall including (1) a more accurate measure of the number of cellulose chains in a microfibril (2) how microfibril diameter affects interactions between cellulose and other polymers in the cell wall and (3) The positioning of each CesA within the complex and their individual contributions to cellulose crystallization.

Preliminary characterization of the CesA 4 and 7 inactivations shows a 33–50% reduction in crystalline cellulose content, while stem height is reduced 25–31%. Measurements by SFG spectroscopy corroborate the measure of crystalline cellulose content and reveal that the cellulose also is less ordered. Analysis of the third CesA inactivation (CesA 8) is in progress, but initial results show shorter stem heights than the CesA 4 or 7 lines. These results support that we have created plants with novel secondary cell wall cellulose microfibrils, by (presumably) reducing the number of cellulose chains per microfibril by a third. SANS measurements will provide key contributions by determining the width, length, and interfibril spacing of cellulose fibrils in our three individual CesA inactivation lines.

6.4.4 Bacterial cellulose as a model system to study the interaction of matrix polysaccharides

Cellulose prepared by *Gluconacetobacter xylinus* has been extensively used to construct cellulose network mimicking the fibrous network in plant cell wall (see Figure 6.2). Unlike traditional extraction method on plant tissues, this approach allows samples to contain little inherent biological wall polymers such as hemicellulose and pectin. More importantly, *Gluconacetobacter xylinus* could overcome the kinetic isotope effect and survive in high concentration D_2O. Careful preparation using this method could yield high deuterium incorporation with minimal effects on the cellulose morphology. This becomes a great advantage to investigate the molecular interaction between cellulose and wall polysaccharides. To contrast match hydrogenated cellulose, it requires the use of 35%

D_2O, which inevitably contain high incoherent background and make analysis at Q>0.1 difficult. The contrast match point of deuterated cellulose has been determined at 81% D_2O, which not only decreases the incoherent background, but also greatly increase the contrast between cellulose and matrix polysaccharides. In Figure 6.3, the SANS data has shown different structure of matrix polysaccharides when interacting with cellulose. Since the contrast is larger than what we had in native cell wall, even small fraction of coating, if there is any, can be well characterized. To obtain a full picture of this work, it would require compositional analysis.

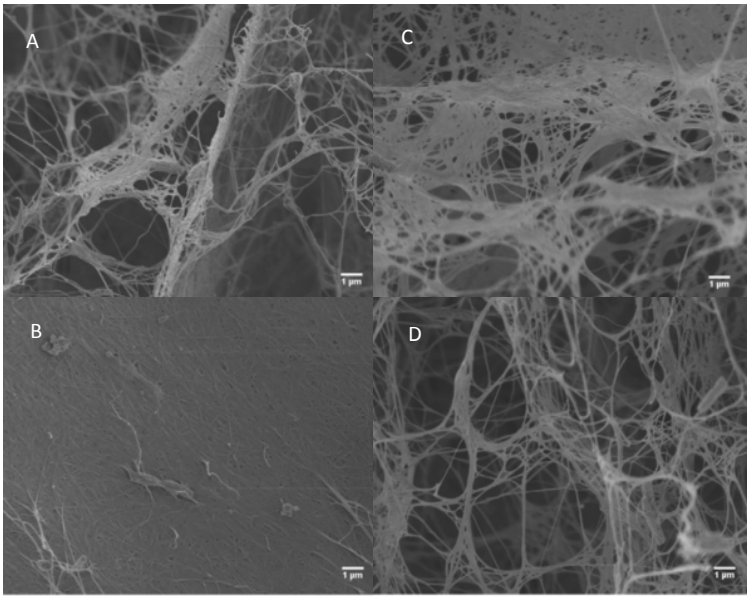

Figure 6.2 SEM images of bacterial cellulose model system. (A) control (B) cultured with xyloglucan (C) cultured with xylan (D) cultured with homogalacturan. (In courtesy of Jin Gu and Jeffery M. Catchmark, *Carbonhydrate Polymer* 2012)

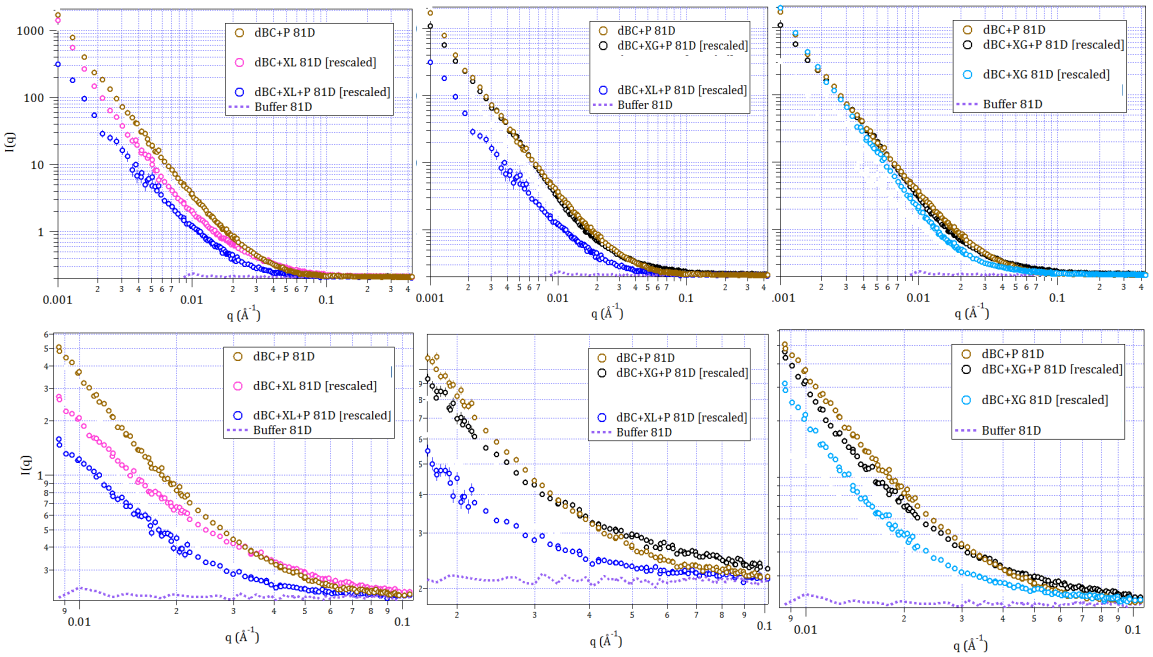

Figure 6.3 SANS spectrum of bacterial cellulose composite with xyloglucan, xylan, pectin measured under the contrast match point of deuterated cellulose (81% D_2O)

Appendix A: SANS Fitting Procedures

In this appendix we discuss the fitting procedures of SANS data. The curve fitting is done using the software Igor Pro (available on www.wavemetrics.com) and two plug-ins developed by NIST and ORNL. There are several steps involved for obtaining the fitting parameters that differ between the structure of cellulose and the matrix polysaccharides.

A.1 Using Igor Pro

Igor Pro is an integrated program for visualizing, analyzing, transforming and presenting experimental data. It is a very powerful tool for non-linear curve fitting. It uses the non-linear least squares fitting program. Igor Pro has a command line interface, which offers the ability to execute scripts or command prompts. Both the NIST and ORNL plug-ins utilize command prompts to execute raw data reduction, non-linear fitting and graphic visualization. The plug-ins provide a large, growing catalog of structural models for users to fit SANS data. Complicated systems (such as the plant cell walls) sometimes contain more than one structure. Thus the fitting of such SANS data requires a combination of two or more structural models. Fitting with multiple models should always be conducted with extra caution as SANS data sometimes can be fit by a combination of irrelevant structure models. Model calculation in the plug-ins is interactive, where changing any of the parameter immediate produce automatic calculation and update the graph. The visualization provides feedback to whether or not the chosen model is an accurate description of the data. The analysis code is written in a

modular format for extensibility, which allows users to add customized codes and models. The current code reads data files (data.abs or data.txt) that have three or four columns in the form of (Q, I, the standard deviation of I, sigma Q(optional)) as the example shown below.

0.003837	4.424	0.001086	0.00398	
0.004241	3.297	0.001087	0.00437	
0.004645	2.628	0.001089	0.004763	
0.005049	1.946	0.001093	0.005158	
…	…	…	…	~200 points
….	…	…	…	
0.4121	0.0119	0.02242	0.4121	
0.4155	0.011	0.0226	0.4155	
0.4188	0.01049	0.02277	0.4188	
0.4221	0.0111	0.02294	0.4221	

A.2 Calculation of Incoherent Background

All of the SANS I(Q) include contributions from coherent and incoherent part. The coherent scattering provides valuable structure information whereas incoherent scattering provides no structure information. Since the incoherent scattering increases the background and lowers the signal-to-noise ratio, it is undesirable in SANS experiments. Making deuterated samples is a common method to minimize the incoherent background. An incoherent scattering however is inevitable in SANS experiments. To obtain an accurate data fitting, it is important to calculate the incoherent background correctly. Here we discuss the calculation method of using Kratky plots (see Figure A.1). Noted that coherent scattering of cell wall samples decrease with Q and incoherent scattering of that is a Q-independent constant. Therefore I(Q) is dominated by incoherent scattering at high Q regime. A Kratky plot enhances the appearance of the characteristic background by making linearized $I(Q)*Q^4$ versus Q^4. The Q-independent background then appears as

the slope of a linearized Kratky curve at high Q.

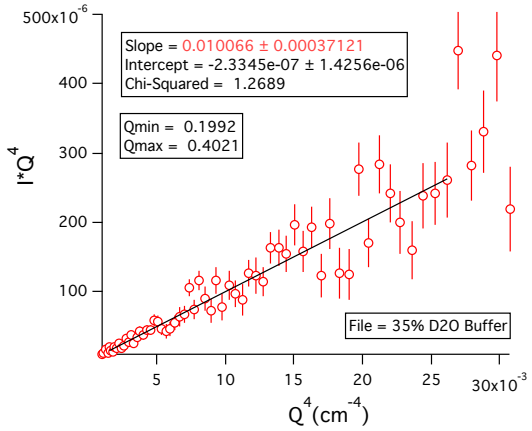

Figure A.1. Kratky plot (IQ^4 vs Q^4) of SANS curves to determine incoherent background

A.3. The Fitting Process for Cell Wall Data

The fitting parameters are obtained by using the Chi-square as criteria for selecting good fits. The outline of obtaining the fitting parameters is summarized in the form of flowcharts below.

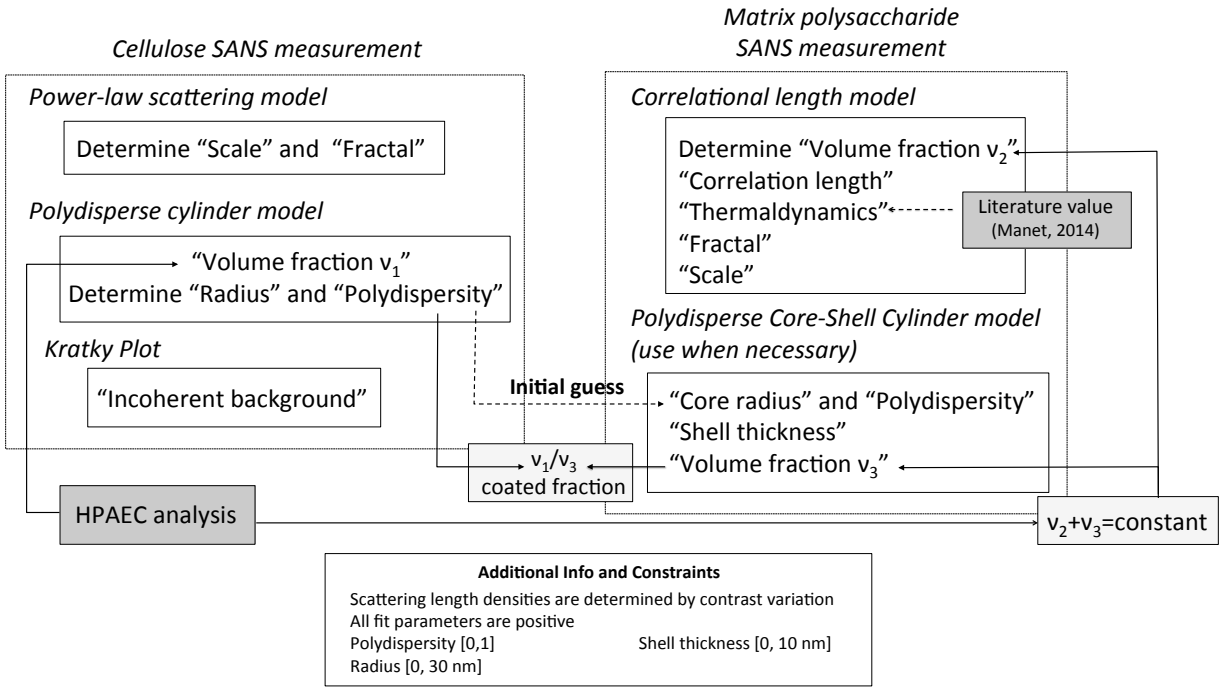

Figure A.2. Overview of fitting SANS data

The fitting algorithm employs different combination of models for the structure of cellulose and that of the matrix polysaccharides. As discussed in Chapter 3 and Chapter 4, the power-law scattering and the polydisperse cylinder model are used for cellulose structure, and the correlation length and the polydisperse core-shell cylinder model (if necessary) are used for the matrix polysaccharide structure. For cell wall samples without detectable core-shell coating feature, a satisfactory fit can be obtained by using just correlation length model. Adding more models to the current combination for cellulose and matrix polysaccharide structure has been tried. But adding the third (or the second) model either does not improve the fitting quality (Chi-square value does not decrease) or makes the fitting process fail to converge. The best scenario of adding extra model is that the software returns a negligible contribution of the extra model (volume fraction << 5%), which physical meaning suggests such structure is not there.

Appendix B: Alternative Fit Models

As described in Appendix A, the software provides an interactive visualization to determine whether or not a chosen model is an accurate description of the data. However, many SANS data look alike. Therefore, using invalid models to describe the structure of samples is a common error for SANS beginners. This kind of mistake can be overcome by experience and practice. In Appendix A.2 and A.3, the chosen models for cellulose and the matrix polysaccharides have been discussed separately. Here we discuss the models that have been tried to fit the SANS data. They can be divided into three categories, which are the models obviously deviate from the data, the models provide a good fit but lack physical meaning and the models provide both good fit and good physical meaning. In the section below we discuss a few cases for example. Only the last group of models can be considered as alternative explanations to SANS measurements on cell walls.

The first group of models does not fit the SANS data on the cell walls. The most common error is that the software has to quit fitting process because it cannot find any appropriate parameters to reduce the Chi-square value (see Figure B.1). In many of these cases, parameters have to be negative to provide a satisfactory fit, which obviously is incorrect. This group includes the structure models of lamellar, disk, dumbbell, microemulsion etc.

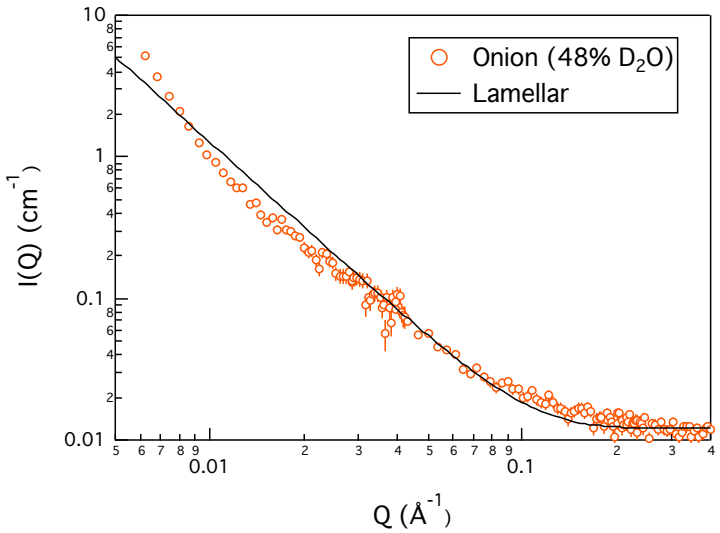

Figure B.1. An example of poor model fitting on cell wall samples. SANS fitting on onion cellulose structure using the Lamellar model. Fitting lines violate the characteristic of SANS data and at best can only fit partial regime of data.

The second group of models provides good fit at certain regime, but lacks physical meaning. For example, the spherical model can fit the cellulose data at high Q regime. However, it does not mean we observe cellulose as a sphere. Instead, the correct interpretation is at high Q regime (~3 nm), neutrons detect spherical shape structure (which in fact is the cross section of cylinder.) The characteristic difference between the sphere model and the cylinder model is the slope of curve at intermediate regime. The former has a plateau whereas the later has a slope of -1 at intermediate regime. For cellulose SANS data, it is necessary to include the slope of -1 to obtain a good fit at the intermediate regime of Q 0.02-0.04 cm^{-1}.

In Chapter 3 and Chapter 4, we report a distribution of cellulose diameter based on the polydisperse cylinder model. The monodisperse cylinder model was tried and has

mixed fitting qualities among the cell wall samples. The monodisperse cylinder model is only good for cellulose with narrow distribution. For example, the monodisperse cylinder model fit well on the *xxt1/xxt2 Arabidopsis* cellulose but not so well on the onion cellulose (see Figure B.1). To maintain a consistent fitting manner, we choose polydisperse rather than monodisperse cylinder model.

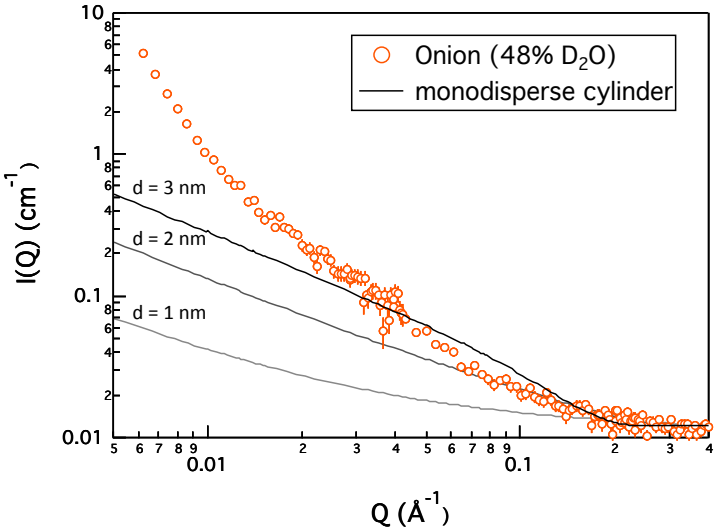

Figure B.2. SANS fitting on onion cellulose structure using the monodisperse cylinder model. Fitting lines using different diameter are plot along with the Onion cellulose SANS data.

The model of rectangular prism serves as an appropriate alternatives to the polydisperse cylinder model (see Figure B.2). In this model, the scale factor, the scattering length density, the length and the incoherent background equal to the ones used in polydisperse cylinder model. The dimension of rectangular cross section is determined from the model fitting. In the case of cellulose in the cell wall of wild-type *Arabidopsis*,

the height and width are 2.1 (±0.3) and 2.7 (±0.5) nm. Figure B.3 compares the cross section determined by rectangular prism and the polydisperse cylinder. As the difference between the two cross sections are very close to the resolution of a SANS experiment (about 1 nm), which physically suggest the genuine cellulose structure can be any of them, or a structure close to both.

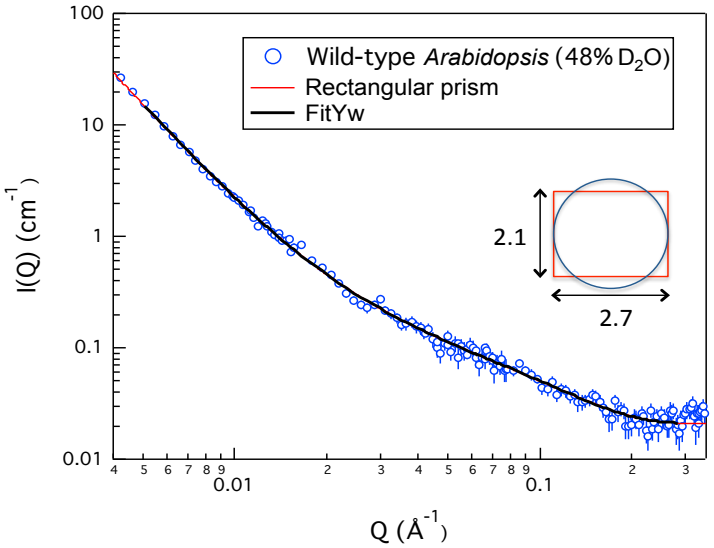

Figure B.3. SANS fitting on wild-type *Arabidopsis* cellulose structure using the rectangular prism model. The calculated structure is shown as the red rectangular box in the picture and compared with the blue sphere representing the best fit by using polydisperse cylinder model.

SHIH-CHUN HUANG

801 D6 W Aaron Dr, State College, PA-16803

Email: sqh5216@psu.edu

Cell: (814) 954-2692

EDUCATION

PhD The Pennsylvania State University (University Park, PA)
Chemical Engineering GPA:3.71

BS National Taiwan University (Taipei, Taiwan)
Chemical Engineering GPA:3.55

PUBLICATIONS

1. Shih-Chun Huang, Li-Jen Chen, "Selective Electroless Copper Plating on Poly(ethylene terephthalate) Surfaces by Microcontact Printing," *Journal of Electrochemical Society, 2010*
2. Shih-Chun Huang, Yong Bum Park, Daniel Cosgrove, Janna K. Maranas, "Determination of Cellulose and Hemicellulose Conformations in the Plant Primary Cell Wall," *in prep*
3. Shih-Chun Huang, Lin Fang, Jeff Catchmark, Christopher Lee, Seong H Kim, Janna K. Maranas, "Dynamics of Water in Cellulose Microfibril Hydrogel," *draft ready*
4. Shih-Chun Huang, Yong Bum Park, Daniel Cosgrove, Janna K. Maranas, "Dynamics of Wall Biopolymer and Water in Arabidopsis Cell Wall," *in prep*
5. Shih-Chun Huang, Lin Fang, Jeff Catchmark, Janna K. Maranas, "Structural Characterization of Cellulose-Based Polymer Material," *in prep*
6. Shih-Chun Huang, Yong Bum Park, Daniel Cosgrove, Janna K. Maranas, "Structural Model for Plant Primary Cell Wall," *in prep*

CONFERENCES

1. International Cell Wall Meeting July 2013, Nantes, France (Oral & Poster)
2. American Physical Society March 2013, Baltimore, MD (Oral)
3. American Chemical Society March 2011, San Diego, CA (Oral & Poster)
4. Gordon Conference on Plant Cell Wall July 2012, Waterville, ME (Poster)
5. Bio-Energy Symposium Feb 2012, University Park, PA (Poster)

AWARD

Travel award to attend 18th National School on the Fundamentals of Neutron Scattering, organized by National Institute of Standard and Technology, 2011